

Advanced Operator Splitting Based Semi-implicit spectral method to solve the Binary and Single component Phase-Field Crystal Model

Gurvinder Singh Bansel

A Thesis presented for the degree of
Doctor of Philosophy

Brunel Centre for Advanced Solidification Technology (BCAST)
Brunel University
England

2011

Abstract

We present extensive testing in order to find the optimum balance among errors associated with time integration, spatial discretization, and splitting for a fully spectral semi implicit scheme of the phase field crystal model. The scheme solves numerically the equations of dissipative dynamics of the binary phase field crystal model proposed by Elder *et al.* [Elder *et al.*, 2007]. The fully spectral semi implicit scheme uses the operator splitting method in order to decompose the complex equations in the phase field crystal model into sub-problems that can be solved more efficiently. Using the combination of non-trivial splitting with the spectral approach, the scheme leads to a set of algebraic equations of diagonal matrix form and thus easier to solve. Using this method developed by the BCAST research team we are able to show that it speeds up the computations by orders of magnitude relative to the conventional explicit finite difference scheme, while the costs of the pointwise implicit solution per timestep remains low. Comparing both the finite difference scheme used by Elder *et al.* [Elder *et al.*, 2007] to the spectral semi implicit scheme, we are also able to show that the finite differencing cannot compete with the spectral differencing in regards to accuracy. This is mainly due to numerical dissipation in finite differencing. In addition the results show that this method can efficiently be parallelized for distributed memory systems, where an excellent scalability with the number of CPUs. We have applied the semi-implicit spectral scheme for binary alloys to explore polycrystalline dendritic solidification. The kinetics of transformation has been analysed in terms of Johnson-Mehl-Avrami-Kolmogorov formalism. We show that Avrami plots are not linear, and the respective Avrami-Kolmogorov exponents (P_{AK}) vary with the transformed fraction (or time). Using the semi-implicit spectral scheme we have been able to provide extensive numerical testing of methods in solving the single component case. This has been demonstrated by using unconditional time stepping with comparable simulations using conditional time stepping. We show the accuracy of the solution for unconditional time stepping is not compromised and furthermore computational efficiency can be significantly increased with the introduction of this scheme. Finally we have investigated how the composition of the initial liquid phase influences the eutectic morphology evolving during solidification. This is the first study that addresses this question using the dynamical density functional theory.

Acknowledgements

It takes a long time to write a PhD thesis and can be a lonely and isolating experience, yet it is obviously not possible without the personal and practical support of numerous people. Thus my sincere gratitude goes to my adoring wife who has given me support and inspiration to complete this thesis when times have been hard over the last few years. You have given me strength and belief and shown me that anything is possible if you put your mind to it.

A special acknowledgement goes to both of my late mothers; they have been angels on my shoulders and have watched over me.

I have been very fortunate with my supervisors, Professor Fan Zhongyun and Professor László Gránásy. They have been a source of inspiration and great discussions. Without their continual support and constructive criticism as well as some noteworthy and fascinating ideas for further research subjects I would not be where I am today. I owe a special thanks to Professor László Gránásy, not only was he readily available for me, as he so generously is for all of his students, but he always read and responded to the drafts of each chapter of my work more quickly than I could have hoped.

I owe to my warmest gratitude to *György Tegze*, with whom I have spent many inspiring moments during my time. You have been there in my times of need, you are truly a great friend in every shape and form.

Finally I would like to thank BCAST and the Hungarian Academy of Science for providing me with the facilities to conduct my computer simulations and I would like to acknowledge EPSRC for financial support during my PHD.

Gurvinder Singh Bansel 2011

Contents

Abstract

Acknowledgements

iv

1 Introduction

1.1 Background and approach	1
1.2 Thesis overview	3
1.3 List of Publications	4

2 Literature Review

Introduction	5
2.1 Review of publications for the PFC	6
2.1.1 PFC	6
2.1.2 Multi-scale approach PFC	8
2.1.3 The PFC and elastic interaction	9
2.1.4 Modelling bcc-interfaces with the PFC	9
2.1.5 PFC vs. Classical density functional theory of freezing	10
2.2 Classical phase-field approach to polycrystalline solidification	11
2.3 Numerical Methods	13
2.3.1 Meshes	14
2.3.1.1 Block structured grid	14
2.3.1.2 Regular (structured) mesh	14
2.3.1.3 Overlapping	16
2.3.1.4 Unstructured mesh	16
2.3.2 Finite difference method (FD)	15
2.3.2.1 Finite Difference Scheme	17
2.3.2.2 Finite Volumes	21
2.3.2.3 Finite Element	22
2.3.2.4 Spectral Methods	24
2.3.3 Numerical Methods Applied	25
2.3.3.1 Explicit Scheme	25
2.3.3.2 Implicit Scheme	27
2.3.3.3 Crank-Nicholson	28
2.3.3.4 Pseudo-spectral method	30
2.3.3.5 Operator Splitting	32

3 Phase Field Crystal (PFC) Method

Introduction	35
3.1 Single Component PFC	35

3.1.1	Single Component (pure material) PFC	35
3.1.2	Numerical scheme for the single component (pure material) PFC	43
3.2	Binary PFC	45
3.2.1	Binary Alloy PFC	45
3.2.2	Numerical Scheme for the Binary PFC	50
3.2.3	Thermal Fluctuations	56
4	Results	
Background		57
4.1	Preliminary-results: Application to Dendritic and Eutectic growth	57
4.2	The Single Component Case	
Background		61
4.2.1	Parameters/initial conditions used in the simulations	61
4.2.2	Method of evaluation	62
4.2.3	Initial set values for simulation and results	66
4.2.4	Initial set values for simulation and results	66
4.3	Binary Case	66
Background		66
4.3.1	Parameters used in simulation	67
4.3.2	Method of Analysis	69
4.3.3	Numerical Results	72
4.3.4	Evaluation of results	69
4.4	Eutectic solidification	80
Background		80
4.4.1	Parameters used in the simulations	80
4.4.2	Method of Analysis	81
4.4.3	Results	86
4.5	Polycrystalline solidification of a binary alloy in two dimensions	86
4.5.1	Parameters used in the simulations	87
4.5.2	Method of Analysis	87
4.5.3	Numerical Results	92
5	Discussion	
Background		93
5.1	Preliminary-results: Application to Dendritic and Eutectic growth	94
5.2	Binary case	95
5.2.1	Convergence of the SIS scheme	95
5.2.2	Comparison of the SIS scheme to the EFD scheme	96
5.2.3	The L^2 test	97
5.2.4	Scalability of the numerical solutions obtained by the SIS and EFD schemes	98
5.3	The Single Component Case	99

5.4 The Johnson-Mehl-Avrami-Kolmogorov (JMAK) model	101
5.5 Polycrystalline solidification of a binary alloy in two dimensions	103
5.6 Eutectic Solidification	105
5.7 Investigation of eutectic solidification that addresses the composition dependence of eutectic pattern formation	106
6 Conclusions	109
7 Further work	111
Bibliography	
Appendix A	
Appendix B	

List of Figures

Figure 2.1: A schematic illustration of various approaches for modeling materials phenomena	6
Figure 2.2: Example of a block-structured grid	14
Figure 2.3: (a) Example of a 2D uniform rectangular grid, (b) Distorted rectangular grid	15
Figure 2.4: Example of a 2D overlapping grid	15
Figure 2.5: Example of a 2D unstructured grid	16
Figure 2.6: A grid representation function u Taylor series expanded	19
Figure 2.7: A regular grid of points to show notation	19
Figure 2.8: Shows the grid generation of finite volume method with control volumes (CV) and compass notations	21
Figure 2.9: Example of triangle used to approximate $u(x,y)$ over the element by the linear function	23
Figure 2.10: This image demonstrates mesh refinement	23
Figure 2.11: The grid demonstrates which nodes are required to calculate the explicit finite difference	26
Figure 2.12: The grid demonstrates which nodes are required to calculate the implicit finite difference	28
Figure 2.13: The grid demonstrates which nodes are required to calculate the Crank-Nicholson scheme	29
Figure 3.1: (a) A sample phase diagram, representing the coexistence region by the shaded area, (b) Two-point direct correlation function at liquid state	38
Figure 3.2: Displays the phase diagram of the single-component PFC model	43

Figure 4.1: Illustrative phase-field crystal simulations for solidification in binary alloys. (a) Is a snapshot taken at 92, 160 time steps and shows the number density difference (δN) map for the solute dendrite; panel (b) shows the solid-liquid interface of the small squared section in section (a) on the downward pointing dendrite arm; panel (c) shows a compact dendrite that was formed in order to compare with (a) to demonstrate the sensitivity of the parameters (snapshot was taken at 55, 000 time steps) and lastly panel (d) demonstrates the eutectic structure that is produced with the proposed PFC, the snapshot was taken at 498, 000 time steps.

60

Figure 4.2: Effect of the spatial and time resolution on the numerical results obtained with the unconditional and conditional time stepping. (a) Shows diameter d Vs Δx , the points correspond to the smallest Δt where the error bars relate to the relative error. (b) Diameter d Vs Δt for both the conditional and unconditional time stepping. (c) Is the graph for unconditional time stepping for all 3 different meshes that were used

63-64

Figure 4.3: Shows the difference between the structure for conditional and unconditional time stepping. The images correspond to $t = 768$. Panel (a) displays the result from conditional time stepping at $\Delta x = \Delta x_0$ with the smallest time step; panel (b) shows the respective result from unconditional time stepping for $\Delta x = \Delta x_0$ with the smallest time step. The contents of the box placed to the left hand edge of the crystal in panels (a) and (b) are shown magnified in panel (c) for the conditional time stepping and panel (d) for unconditional time stepping. The two methods lead to fairly identical results.

65

Figure 4.4: High resolution SIS solution used as reference obtained on a $1,024 \times 1,024$ grid with spatial and time steps of $\Delta x = \Delta x_0/4$ and $\Delta t = \Delta t_0$. Panel (a) presents a snapshot of the total number density at time $t = 768$, while panel (b) shows the respective total number density n distribution along the horizontal centerline.

68

Figure 4.5: Effect of the spatial resolution on the numerical results obtained with the semi-implicit spectral (SIS) and explicit finite difference (EFD) methods. (a) Displays the dependence of the normalised inter-atomic distance against the spatial resolution, (b) shows the dependence of the normalized diameter (d/d_0) on the spatial step, Δx . The reference states are $a_0 = 7.435 \times (1.0 \pm 0.004)$, and $d_0 = 192.0 \times (1.0 \pm 0.0003)$ which correspond to the lattice constant and particle diameter and was obtained from the SIS computation with the smallest Δx and Δt .

70

Figure 4.6: Displays the normalized diameter (d/d_0) versus the time step Δt , $d_0 = 192.0 \times (1.0 \pm 0.0003)$ which corresponds to the particle diameter and was obtained from the SIS computation with the smallest Δx and Δt .

71

Figure 4.7: Demonstrates the difference in the diameter of the crystal for different spatial steps for the EFD which are images (a), (c), (e), (g) and (i), SIS images (b), (d), (f), (h) and (j). All snapshots were taken at dimensionless time $t = 768$ and the spatial resolution as well as the time steps have been described in the above section. One key fact that is shown here is for the SIS the diameter of the crystal d does not vary with the spatial resolution, which cannot be said for the EFD.

73-74

Figure 4.8: Shows the cross sectional profiles ($t = 768$) for the solid liquid interface in SIS simulations. This was performed using three

different mesh spacing and $t = \Delta t_0$. Section (a) depicts the number density while section (b) depicts the total number density difference.

75

Figure 4.9: Shows the cross sectional profiles ($t = 768$) for the solid liquid interface in EFD simulations. This was performed using three different mesh spacing and to ensure numerical stability I have used the maximum time steps that were available. Section (a) depicts the number density while section (b) depicts the total number density difference.

76

Figure 4.10: Scalability of the numerical solutions obtained by the SIS and EFD schemes. (a) Computational cost for an individual time step on a single mesh point vs. the number of CPU's. (b) Computational time is required to perform a simulation vs. the number of CPU cores, this has been conducted for three different mesh spaces.

78

Figure 4.11: Demonstrates the eutectic transition from concentric ring-like lamellar structure to irregular dots. Simulations were conducted on a rectangular grid of size 1024 x 1024. Snapshots taken at the 200,000th time step are shown. (a) has a number density difference $(\delta N) = 10^{-6}$ and this is our reference point. (b) has a number density difference $(\delta N) = 0.02$, (c) has a number density difference $(\delta N) = 0.04$ and (d) has a number density difference $(\delta N) = 0.06$.

82

Figure 4.12: (a) Shows the grain size for $(\delta N) = 10^{-6}$, $(\delta N) = 0.02$ and $(\delta N) = 0.06$ as a function of time, (b) Shows the average velocity as a function of time with the same concentrations as in (a), both results

were conducted on a simulation window of 1024 x 1024.

83

Figure 4.13: (a) Shows the average velocity for $(\delta N) = 10^{-6}$, $(\delta N) = 0.02$ and $(\delta N) = 0.06$ as a function of time, (b) shows the average velocity vs. Composition both results were conducted on a simulation window 2048 x 2048.

84

Figure 4.14: Shows the average velocity for $(\delta N) = 0.06$ obtained in the simulation windows of size 1024 x 1024 and 2048 x 2048 as a function of time.

85

Figure 4.15 Shows the average velocity for $(\delta N) = 0.06$ obtained in the simulation windows of size 1024 x 1024 and 2048 x 2048 vs. $t^{1/2}$

85

Figure 4.16: These images relate to dendritic growth of 5 crystalline particles, snapshots were taken at 1000, 5000, 7500, 10 000, 15 000 and 20 000. The simulations have been performed on a $16,384 \times 16,384$ grid, using a semi-implicit spectral method.

88

Figure 4.17: These images relate to dendritic growth of 50 crystalline particles, snapshots were taken at 1000, 3000, 4500, 5000, 7 500 and 10 000. The simulations have been performed on a $16,384 \times 16,384$ grid, using a semi-implicit spectral method.

89

Figure 4.18: These images relate to dendritic growth of 500 crystalline particles, snapshots were taken at 250, 500, 625, 750, 1125 and 1500. The

simulations have been performed on a $16,384 \times 16,384$ grid, using a semi-implicit spectral method.

90

Figure 4.19: Demonstrates the crystallization kinetics for binary phase-field crystal, the top graph shows the number of atoms in the crystalline phase against time; the middle is the Avrami plots where the slope of each curve is used for the analysis of kinetics. The bottom shows Avrami-Kolmogorov exponent as a function of the reduced transformed fraction.

91

List of Tables

Table 4.1: Parameters used in computing Figure.4.1, description for them can be seen in subsection 3.2.1	59
Table 4.2: Parameters used in computing the single component case for both conditional and unconditional time stepping simulations (description of parameters are presented in subsection 3.2.1)	61
Table 4.3: Scaled L^2 difference of the Fourier spectra	77
Table 4.4: Parameters used in computing the eutectic structures	81

Chapter 1

INTRODUCTION

1.1 Background and Approach

Field theoretical models relying on coarse-grained order parameters and gradient free energy are used widely for describing phase transitions in complex systems, including magnetic phase transitions, condensation, phase separation and crystallization ([Gunton *et al*, 1983], [Langer, 1992], [Bray, 1994], [Cahn, Hilliard, 1958], [Allen, Cahn, 1979], [Shih *et al*, 1987], [Rogers *et al*, 1988], [Oono, S.Puri, 1998] and [Wu *et al*, 2006]). Molecular approaches based on the dynamic extension of the density functional theory (DDFT) of classical particles have also in use for similar purposes for some time [Oxtoby, 1991], however, the accessible system size limits the range of problems they can address. A promising recent theoretical approach to crystalline freezing in undercooled liquids is the Phase Field Crystal (PFC) method [Elder *et al*, 2002], [Elder *et al*, 2004]. It is an atomistic theory which is considerably simpler from the viewpoint of numerical implementation than the full Dynamical Density Functional Theory (DDFT), and thus can be used to address crystallization in systems containing a few millions of atoms [Elder *et al*, 2002]. The PFC can be regarded as a simplified classical Density Functional Theory (DFT). Its free energy functional can be derived from the perturbative DFT of Ramakrishnan and Yussouff [Ramakrishnan, Yussouff, 1979] after simplifications, such as Taylor expanding both the ideal gas term in the free energy, and the two-particle direct correlation function in the interaction term [Elder *et al*, 2004]. The resulting free energy functional can be transformed into a Swift-Hohenberg/Brazowskii form [Swift, Hohenberg, 1977], [Brazowskii, 1975]. Since the order parameter, the time-averaged number density of molecules, used here is a conserved quantity, and only slow transitions are considered for the sake of simplicity, conserved dynamics taken in the

overdamped limit applies [Elder *et al*, 2004]. The advantage of this atomistic approach relative to conventional phase-field techniques is that it automatically incorporates the crystal structure with the associated anisotropy of the interfacial free energy (and other properties), the elasticity, and various lattice defects including dislocations. The PFC also has advantage over the traditional atomistic simulations (Molecular Dynamics), as PFC simulations can be conducted on the diffusive time scale. Finally, it is able to address crystallization on a considerably larger size-scale than the full DDFT.

The main objective of this thesis is to provide a numerically efficient method to solve the equations of dissipative dynamics for both the single component and binary PFC method. In addition, we will use this PFC model to analyse various aspects of solidification such as polycrystalline freezing and the formation of eutectic structures. Solution of the PFC model is numerically demanding. This is especially true for the binary PFC due to the variable coefficients that appear in the equations of motion. There are different strategies to address these problems. An appealing possibility is the combination of a coarse-grained formulation, which can be obtained using the renormalization group technique [Goldenfel *et al*, 2005] with adaptive gridding (local refining and coarsening of the computational mesh as required [Provatas *et al*, 2005], [Athreya *et al*, 2007]). While this approach has been implemented successfully for the single component case, its extension for the binary case is not without difficulties due to the different size scales appearing (due to the difference of the interatomic distances A-A, A-B, and B-B). Another possibility is to use a numerical algorithm that is sufficiently efficient. One of the promising candidates is the operator splitting method, a numerical technique that has been successfully used to solve the Navier-Stokes equations [Christov, Marinova, 2001], [Mimura *et al*, 1984], the Hamilton-Jacobi equations [Jakobsen *et al*, 2001], [Karlsen, Risebro, 2002], advection-diffusion problems [Karlsen *et al*, 2001], [Marinova *et al*, 2003] and is considered to be one of the most efficient methods for solving complex PDEs in applied physics [Strang, 1968], [Marchuk, 1988].

In the present thesis, we apply the latter approach for solving the coupled equations of motions of the binary PFC model. Following the philosophy of operator splitting the main problem is split into sub-problems (represented by appropriate sub-operators),

which can be solved numerically efficiently. The errors associated with the operator splitting method have been investigated in detail [Farago, Havasi, 2005a]. Other sources of error are the numerical methods used for solving the sub-problems. The respective numerical error can be split into two contributions, firstly the error produced by the time integration and secondly the error originating from spatial discretization. To avoid accumulation of these errors that would lead to order reduction and unnecessary loss of accuracy, one needs to choose carefully the method of discretization. P. Csomos and I. Farago have discussed this problem in detail [Csomos, Farago, 2008]. Nevertheless, even with these types of errors, the operator splitting method appears to be one of the most efficient techniques in dealing with high order PDEs.

1.2 Thesis overview

The thesis has been organized as follows: This introductory chapter summarizes the context, motivation and main contributions of this thesis, in addition, it lists the publications I co-authored during my work. A literature review on previous work done on the PFC model is presented in Chapter 2; it also formulates the motivations for the present work. Chapter 3 outlines the numerical techniques applied for solving the governing equations of the single component and binary PFC models. The results of the work are presented in Chapter 4; The first part of the chapter demonstrates the preliminary results for the PFC; In the second part of the chapter I present the numerical test of methods I applied for solving the single component PFC. I have moved on to address the binary case where I demonstrate the numerical stability of the proposed numerical scheme, investigate its computational efficiency in parallel environment, and apply it for the exploration of polycrystalline dendritic solidification in binary alloy. Chapter 4 also includes an investigation of eutectic solidification that addresses the composition dependence of eutectic pattern formation. In Chapter 5 I present my discussion for all the respective results. Chapter 6 is a summary of the main conclusions of the thesis and in Chapter 7 I have suggested further work that can be carried out.

1.3 List of Publications

1. T. Pusztai, G. Tegze, G. I. Tóth, L. Környei, G. Bansel, Z. Fan, L. Gránásy:
Phase-field approach to polycrystalline solidification including heterogeneous and homogeneous nucleation. J. Phys.: Cond. Matter **20**, 404205 (2008).
2. G. Tegze, G. Bansel, G. I. Tóth, T. Pusztai, Z. Fan, L. Gránásy:
Advanced operator-splitting-based semi-implicit spectral method to solve the binary phase-field crystal equation with variable coefficients. J. Comp. Phys. **228**, 1612–1623 (2009).

Chapter 2

LITERATURE REVIEW

Introduction

The Molecular Dynamics (MD) technique and field-theoretic models relying on coarse-grained order parameters (often termed as phase-field models) are widely used for simulations of crystal growth. In the case of Molecular Dynamics, the simulations are restricted to atomic sizes and photonic time scales (picoseconds ps). The coarse-grained field theories overcome these limitations to some extent at the expense that many of the microscopic details (such as anisotropy, elasticity, etc.) are lost and have to be incorporated “by hand”. A recently developed theoretical approach named the Phase Field Crystal (PFC, which can be considered as a simple dynamical density functional theory) model offers a microscopic description which describes crystallization of liquids on a diffusive time scale that can be many orders of magnitude longer than the range accessible for molecular dynamics which can be seen in Figure 2.1. Being a density functional theory, the model naturally incorporates elastic and plastic deformations, multiple orientations, anisotropies, etc., and offers an efficient atomistic description of crystal growth from the melt. The PFC equation tries to find a path along the free energy where the energy is minimized through the equation of motion, this results a path where the free energy of the system is monotonic and decreasing (a function which increases but decreases).

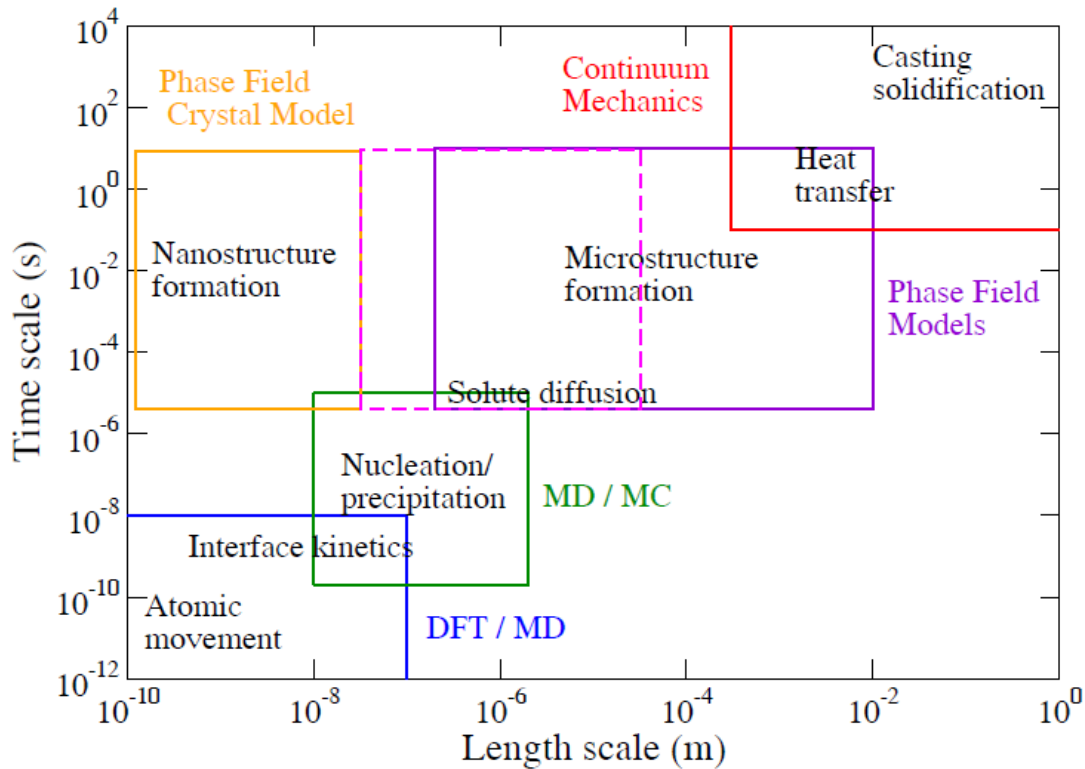


Figure 2.1: A schematic illustration of various approaches for modeling materials Phenomena [Athreya, 2006]

2.1 Review of publication for the PFC

2.1.1 PFC

The PFC model was first introduced by Elder et al. [Elder *et al*, 2002]. It relies on a Swift-Hohenberg (SH) type free energy functional and an overdamped conservative equation of motion in describing the time evolution of the field ψ that represents the reduced local particle density. The SH form of the free energy produces periodic states. The work was focused on the two-dimensional form of the PFC for both the single component and binary case. Several methods were used to validate the model. Firstly the PFC was compared to Read and Shockley's prediction of grain boundaries [Read,

Shockley 1950]. It was found that PFC fitted closely to Read and Shockley's predictions for small angles. The other method used for validating the model was an investigation of morphological instability in epitaxial growth. Here the PFC was used to calculate the critical height H_c at which dislocations eventually nucleate. H_c was then compared to results from the equation by Matthews and Blakesless [Matthews, Blakesless 1975]. It was found that the PFC results were consistent with the theoretical relationship. In addition, Elder et al deduced the time scales accessible to the PFC simulations. It was concluded that the PFC could simulate a diffusion controlled process in 1000 time steps as opposed to Molecular Dynamics which needs approximately 10¹² time steps for the same process.

Elder *et al* reported further work that displayed several applications, which included epitaxial growth, material hardness, grain growth, reconstructive phase transition and crack propagation [Elder *et al* 2004]. In addition to this, basic properties of the PFC model, such as the phase diagram, linear elastic constants and the vacancy diffusion constants were also calculated analytically. Elder *et al* evaluated the grain boundary energy for the PFC and compared it with the experimental data of systems like tin, lead and copper [Aust, Chalmers, 1952], [Gjostein, Rhines, 1959]. The PFC was found to have good agreement and in part provided evidence that the interaction between dislocations is correctly captured. Simulations were conducted for epitaxial growth using an Euler discretization scheme for the time derivative and the "spherical Laplacian" approximation to calculate all the Laplacian operators. From the simulations it could be seen that the film initially grew in a uniform manner before becoming unstable due to buckling or mound instability; then the film nucleated dislocations in the valleys where the stress was largest. After the dislocations nucleated, the interface grew in a regular fashion. Material hardness was investigated and a significant distortion at the grain boundary was discovered, however, small strains and grain boundary locations were relatively unaffected. The influence of grain sizes on the stress-strain relationship was also investigated for four-grain sizes. Elder *et al* reported that the PFC approach was able to reproduce the inverse Hall-Petch effect [Schiotz *et al* 1998], [Schiotz *et al* 1999]. This

work has provided evidence that the PFC can simulate the solidification process accurately for a wide variety of processes.

2.1.2 Multi-scale approach PFC

The multi-scale approach for simulating polycrystalline materials relying on the PFC theory was first developed by Goldenfeld. They used the renormalization group (RG) [Provatas *et al*, 2005] and transformed systematically to coarse-grain the PFC model that Elder *et al* presented. The basic idea was to obtain a set of renormalization group equations of motion for the complex amplitudes of the periodic density field. From the complex amplitude the atomic-scale density field can be reconstructed within the one-mode approximation. Comparing the grain boundary energies for both the original PFC and the coarse-grained version demonstrated the accuracy of the method. It was concluded that the RG equations closely follow the trends the PFC predicted for low angle grain boundaries, in fact the maximum difference in the free energy's between the two methods was approximately 1.6%. Following this the computational efficiency was also demonstrated. It was found that the RG form of the PFC showed a speed up close to a factor of 10 compared to the original PFC, while the error in the free energy was still less than 0.1%.

Further work by Athreya *et al* in 2006 [Goldenfeld *et al*, 2006], [Athreya *et al*, 2007] presented a hybrid numerical implementation that combined cartesian and polar representation of the complex amplitude with adaptive mesh refinement, allowing a multi-scaled modelling of complex polycrystalline materials microstructure to be possible. Athreya *et al* solved the renormalization group equations using a C++ adaptive mesh refinement algorithm that uses a finite difference scheme [Fan *et al*, 2006]. It was shown that depending on the application, the scheme could be anywhere between one to three orders of magnitude faster than the equivalent uniform grid implementation of the PFC equation on a single processor machine. While this approach has been implemented

successfully for the single component case, its extension for the binary case is not without difficulties due to the different size scales appearing.

2.1.3 The PFC and elastic interaction

Stefanovic *et al* in 2006 suggested that the simplified PFC did not contain a mechanism for simulating elastic interactions sufficiently and provided an alternative method called the Modified Phase Field Crystal (MPFC) [Stefanovic *et al*, 2006]. This method included both diffusive dynamics and elastic interaction that used wave modes, which propagated on time scale slower than atomic vibrations; however it was still faster than diffusive time scale. Stefanovic *et al* performed simulations for grain growth and elastoplastic deformation, which was consistent with properties of nanocrystals. First Stefanovic *et al* simulated isothermal solidification using the MPFC. It was found that during the simulation the effect of the first term in the MPFC equation was small but significant. Comparing the MPFC results to the PFC results, it was found that the grain growth and morphology was indistinguishable. The elastic relaxation present in the MPFC was demonstrated by simulating a one-dimensional single crystal, which was under uniaxial tension. The displacement along the one-dimensional sample at three different times was found to be consistent with elasticity theory. It was shown that the MPFC becomes visco-elastic as the damping is increased. This provides evidence that the PFC alone cannot adequately describe elastic responses in strained crystals at finite strain rates. The MPFC naturally incorporates this.

2.1.4 Modeling bcc-interfaces with the PFC

Kuo-An Wu and Alain in 2006 [Wu *et al*, 2006] investigated body-centered-cubic (bcc) structures to find the physical origin and quantitative predictions of anisotropy. They formed a system using Ginzburg-Landau (GL) theory where amplitudes of density waves corresponded to reciprocal lattice vectors. Earlier work for the formulation of the Ginzburg-Landau (GL) theory was introduced by Shih *et al* in 1987 [Shih *et al*, 1987].

Using both these theories, Wu and Karma fitted the model parameters to experimental data of iron and comparisons were made with molecular dynamic simulations, which used an embedded-atom-method (EMA) with the potential of MH(SA)² [Mendelev *et al*, 2003]. It was concluded that the theory Wu and Karma proposed in 2006 was able to predict the anisotropy of the interfacial energy and the density wave structure of the interface with good agreement to the results obtained by the molecular dynamic simulation.

In 2007 Wu and Karma extended their work from 2006 to investigate the equilibrium properties of bcc-liquid interface with the PFC [Wu, karma, 2007]. The PFC model used was based on the reformalisation of the Swift-Hohenberg equation [Swift, Hohenberg, 1977], which conserved the dynamics introduced by Elder *et al* in 2002 and 2004. Using this form Wu and Karma constructed the phase-diagram, which corresponded to bcc-liquid coexistence and derived the amplitude equations for the PFC from a multiscale expansion. The amplitude equations described the equilibrium of the crystal density waves in the interface region. This allowed the PFC amplitude equations to be made comparable to the previous Ginzburg-Landau (GL) theory in 2006 [Wu *et al*, 2006]. Using both these theories Wu and Karma fitted parameters to experimental data in iron and comparisons were made with molecular dynamic simulations, which used an embedded-atom-method (EMA) with the potential of MH(SA)² [Mendelev *et al*, 2003]. It was concluded that for both the PFC amplitude and the Ginzburg-Landau (GL) theory the amplitude profile and interatomic widths that were predicted were almost indistinguishable. The numerical results also showed that both methods gave similar predictions for γ .

2.1.5 PFC vs. classical density functional theory of freezing

The density functional theory (DFT) for freezing was first formulated by Ramakrishnan and Yussouff [Ramakrishnan, Yussouff, 1979]. The classical DFT techniques have been reviewed by Singh [Singh, 1991] and Evans [Evans, 1979]. In 2007 Elder *et al* [Elder *et*

al, 2007] used this previous work to make the connection between the correlation function that enters the DFT and the free energy functional, which is used in the PFC. This connection was then exploited to develop a binary PFC model. Here the free energy expansion was truncated by the two-point correlation function which then could be characterized by three parameters: lattice constant, bulk modulus of the crystal and the isothermal compressibility of the liquid. In addition a binary PFC has been developed. The binary PFC was used to perform simulations for eutectic and dendritic microstructures. It was also concluded by Elder *et al* that the binary PFC was able to model phase segregation, grain growth, elastic and plastic deformation in anisotropic systems with multiple crystal orientation on the diffusive time scale.

Following this work Berry *et al* in 2008 investigated freezing and glass formation in monatomic liquids using the PFC method [Berry *et al*, 2008]. The model was able to capture the relevant behavior. A semi-implicit pseudospectral algorithm was used to solve the equation of motion in three dimensions with periodic boundary conditions. The algorithm was reported to improve the computational efficiency in the order of one to two orders of magnitude compared to the real space finite difference Euler scheme.

2.2 Classical phase-field approach to polycrystalline solidification

Over the last several decades there has been an intensive amount of work within the area of polycrystalline solidification however there is a large amount that still needs to be understood. Various methods have been developed to model polycrystalline solidification which are level set [Tryggvason *et al*, 2002] [Tan, Zabaras, 2006, 2007], cellular automata [Zhu, Hong, 2002], [Beltram-Sanchez, Stefanescu, 2004] and [Zhu *et al*, 2008]. Other front tracking techniques have been investigated Schmidt, Steinbach *et al* and Jacot and Rappaz [Schmidt, 1996], [Steinbach *et al*, 1999], [Jacot, Rappaz, 2002]. Another method is the phase-field approaches; this scheme connects the thermodynamic and kinetic properties with microstructure through a transparent mathematical formalism. Therefore this method has been preferred over the others stated above. There have been

several reviews on this model which I would like to draw the reader's attention to [Boettinger *et al*, 2002], [Chen, 2002], [Hoyt *et al*, 2003], and [Gránásy *et al*, 2004a]. In order to model the polycrystalline solidification within the phase field model the inclusion of homogeneous and/or heterogeneous nucleation is required. This is done for field theoretical models by adding Langevin noise to the equation of motion which can be seen in [Gunton *et al*, 1983]. However crystallographic orientation is required to be incorporated in the model to describe the impingent process of a large number of crystallites that grow anisotropically. The reason for this, crystallographic orientation allows the specification of the preferred growth directions of growth. First simulations to incorporate this were conducted by Morin *et al* [Morin *et al*, 1995]. They relied on a free energy density that had n wells which corresponded to n crystallographic orientations, thus breaking the rotational symmetry of the free energy.

Another approach was realized by the multi-phase-field theory [Steinbach *et al*, 1996], [Fan, Chen, 1996], [Tiaden *et al*, 1998], [Diepers *et al*, 2002], [Krill, Chen, 2002] which was used to address the formation of particles with random crystallographic orientations. This approach introduced separate phase field for every crystal grain. The advantage of this was that the model offered more flexibility however this was at the expense of enhanced mathematical and numerical complexity. Using the MPFT approach, studies in to polycrystalline dendritic and eutectic/peritectic solidification have been conducted. Furthermore MPFT has been successfully applied for describing the time evolution of multigrain structures. However, the large number of phase fields applied in these approaches leads to difficulties, when nucleation is to be modelled by Langevin noise. Noise-induced nucleation can be substituted by inserting nuclei by 'hand' into the simulations. However when structures that require the nucleation of different crystallographic orientations at the growth front are to be addressed this procedure becomes non-trivial. Furthermore this treatment rules out possible interactions between the orientation of new grains and diffusion. Therefore growth front nucleation in the MPFT model is not straight forward. In order to model complex polycrystalline structures (especially the polycrystalline growth forms) it seems that another method is required

which relies on an orientation field to monitor the crystallographic orientation. Such a model has been provided by Kobayashi *et al*, (1998) [Kobayashi *et al*, (1998)] to model polycrystalline solidification in 2D. Here they have used a non-conserved scalar field to monitor crystallographic orientation. The energy density of $f_{ori} = HT|\nabla\theta|$ (f_{ori} is the orientation free energy), where the H coefficient has a minimum at the position of the interface, the minimization of free energy leads to a stepwise variation of $\theta(\mathbf{r})$, a behaviour approximating reasonably the experimental reality of stable, flat grain boundaries. (Such minimum can be realized making the coefficient H dependent on the phase field, by introducing the factor $1 - p(\varphi)$ ($p(\varphi)$ is the phase interpolation function) into f_{ori} [Gránásy *et al*, 2002]). For the problems which include solid-solid and solid-liquid interfaces, successful modifications to the approach above have been made by Kobayashi *et al* and Warren *et al* [Kobayashi *et al*, 1998, 2000] and [Warren *et al*, 2003]. Furthermore Gránásy *et al* [Gránásy *et al*, 2002] have provided an extension of the orientation field to the liquid state, where it has been made to fluctuate in time and space. This allows handling of such polycrystalline growth forms as disordered dendrites, spherulites, axialites, and fractal like growth forms [Gránásy *et al*, 2003; 2004b].

In order to provide information on polycrystalline solidification I am going to apply the PFC for multi-grain crystallization in a binary liquid alloy. My aim is to investigate the behaviour of the Avrami-Kolmogorov exponent as a function of the number density of the initial crystal seeds. This kinetic exponent is often used for characterizing the time evolution of crystallization.

2.3 Numeric Methods

2.3.1 Meshes

Meshes are discrete locations where variables are calculated. The location is defined by a numerical grid which is essentially a discrete representation of geometric domain. There a

four major grids and in the following sub-section I am briefly going to explain them and identify the advantages and disadvantages of each.

2.3.1.1 Block structured grid

They consist of several rectangular grids which are combined together. The joining points of two grids share the same common neighbour. The key point to remember is that the structure may be irregular but they may not overlap one another. The advantage of this grid is its flexibility; also it allows regions to have finer grids where greater resolution is required. However due to the complexity of the grids one can find it difficult to generate the mesh. I have demonstrated such a grid in Figure 2.2; this was taken from [inf.bauwesen].

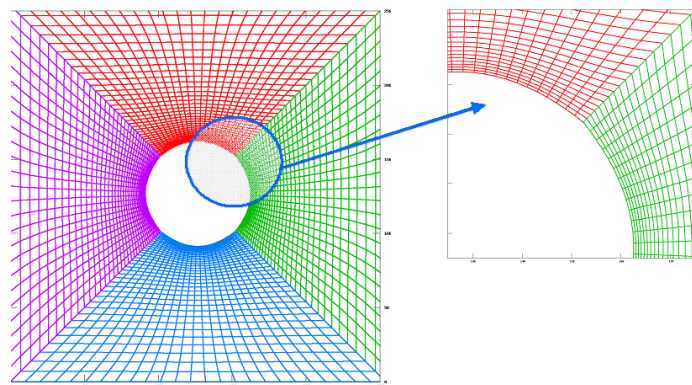


Figure 2.2: Example of a block-structured grid taken from [inf.bauwesen].

2.3.1.2 Regular (structured) mesh

This is the simplest grid structure out of the four since it's logically equivalent to a Cartesian grid. The mesh is a uniform rectangular grid, which can be distorted to fit any shape and was used for our simulations. One of the key advantages for the mesh is that it is easy to implement and a large number of solvers can be used in developing a solution

technique. However they can only be used for geometrically simple solution domains and furthermore it is difficult to control the distribution of grid points. I have provided an example of such a mesh in Figure 2.3 which was taken from [rspa]. This type of mesh was used for our simulations because the FFT that was used was available for the regular mesh.

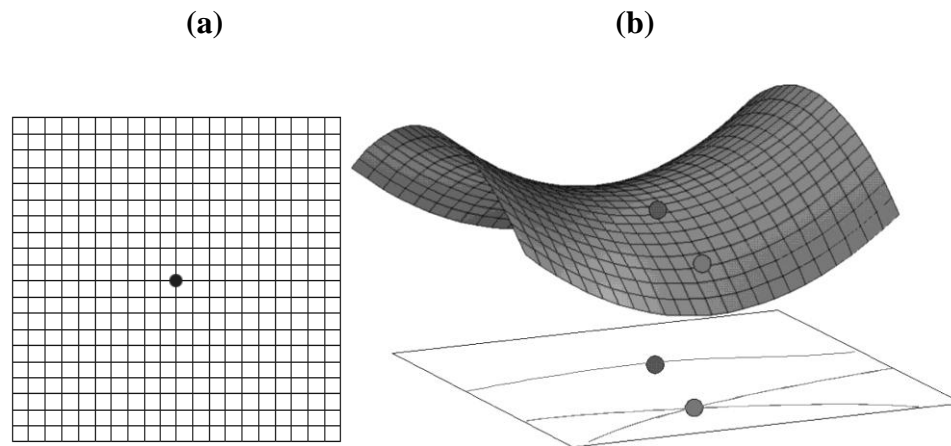


Figure 2.3: (a) Example of a 2D uniform rectangular grid [Ferziger, Peric, 2002], (b) Distorted rectangular grid taken from [rspa].

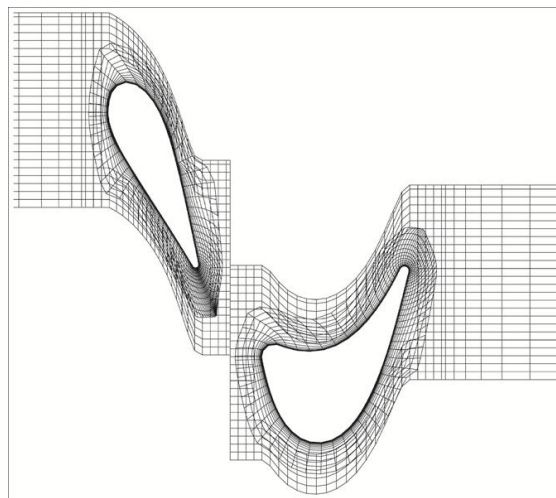


Figure 2.4: Example of a 2D overlapping grid taken from [psc.edu].

2.3.1.3 Overlapping

This type of mesh is sometimes called composite or chimera grid. Essentially the mesh contains several grids with the grids overlapping one another. In these overlapping regions the boundary conditions for one of the blocks can be obtained by interpolating the solution from the other (overlapped) block, Figure 2.4 shows a typical example and was taken from [psc.edu]. The disadvantage of these grids is that conservation is not easily enforced at the block boundaries. However one advantage is that it can be used for complex domains.

2.3.1.4 Unstructured mesh

It is best suited for Finite Element (FE) and Finite Volume (FV) approaches, in practice the grids are made up of triangles and quadrilaterals in 2D and tetrahedral or hexahedral in 3D. A simple example of this type of mesh in 2D is illustrated in Figure 2.5, this was taken from [vidi.cs].

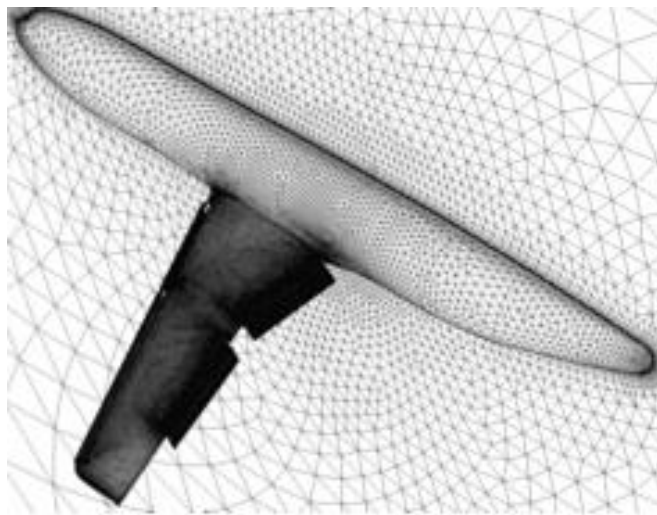


Figure 2.5: Example of a 2D unstructured grid taken from [vidi.cs]

This type of mesh can be used for very complex geometries, due to the mesh being the most flexible type it can fit any solution domain boundary. With this in mind it can be said that the mesh can be used with any discretization scheme. Furthermore I would like to raise the point that due to the irregularity of the data structure, each nodes location and neighboring connections would need to be explicitly specified. This in turn causes the matrix of the algebraic equations not to diagonally dominate. This result makes the solvers for the algebraic equations slower in comparison to the regular mesh.

2.3.2 Discretization Method

Discretization methods are used to approximate PDEs by a system of algebraic equations. The main methods that are employed are finite differences (FD), finite volume (FV), finite element (FE) and spectral schemes. With each method the desired characteristics of the mesh may differ. However in general, for all types of mesh there are certain characteristics to be controlled.

- **Local density of grid points:** Density of points gives you more accuracy however the computation takes a longer time.
- **Smoothness of point distribution:** Large variations in the grid or shape can cause numerical diffusion. This can lead to inaccurate results and instabilities.
- **The shape of grid volumes:** For instance, in Finite element (FE) triangular elements are used, in order to prove convergence under strict conditions.

2.3.2.1 Finite Difference scheme

This scheme is commonly used for solving differential equations. They are based on approximations that replace the PDE by the finite difference equation. These approximations are in algebraic form and the solution relates to grid point. The key steps

for the finite difference scheme are firstly to divide the solution into grid nodes. Secondly approximate the PDE by the equivalent finite difference that relates to the solution on the grid. Thirdly solve the PDE subject to prescribed boundary/initial conditions. The approximations come directly from the Taylor expansion. To elaborate I am going to demonstrate this with a 2-D Taylor series expansion. From Figure 2.6 if we consider the function u and Taylor series expanded about the point (x, y) we obtain equations 2.3.1 and 2.3.2. Now considering a regular grid of points shown in Figure 2.7 we can use the notation $u(x, y) = u_{i, j}$, $u(x + \Delta x, y) = u_{i+1, j}$ and $u(x, y + \Delta y) = u_{i, j+1}$, substituting this notation back into equations 2.3.1 and 2.3.2 we can obtain the equations 2.3.3 and 2.3.4. From equations 2.3.3 and 2.3.4 we can then make the finite difference approximations. The approximations can be classed into three forms forwards; backwards and central and have been defined below:

- **Forward Difference (first order derivative):** By taking the positive of the Taylor's expansion and truncating it to the terms including second order and higher we can then rearrange it so we get the following expression in equation 2.3.5.
- **Backwards Difference (first order derivative):** By taking the negative of the Taylor's expansion and truncating it to the terms including second order and higher we can then rearrange it so we get the following expression in equation 2.3.6.
- **Central Difference (first order derivative):** This is obtained truncating both equations 2.3.3 and 2.3.4 terms higher than the second derivative. Then by subtracting them from one another and rearranging them in terms of the first order derivative so we get the expression in equation 2.3.7

In order to obtain the second order central difference we truncate both equations 2.3.3 and 2.3.4 terms higher than the second derivative. Then by adding them together and rearranging them in terms of the second order derivative we can obtain the second order

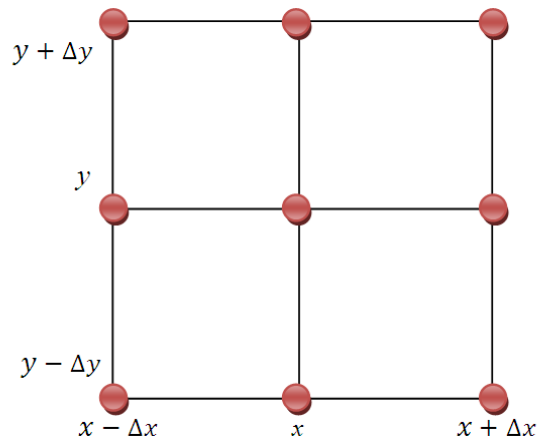


Figure 2.6: A grid representation function u Taylor series expanded about the point (x, y) to obtain equations 2.3.1 and 2.3.2

$$u(x \pm \Delta x, y) = u(x, y) \pm \Delta x \frac{\partial u}{\partial x} + \frac{1}{2!} \Delta x^2 \frac{\partial^2 u}{\partial x^2} + O(\Delta x^3) \quad (2.3.1)$$

$$u(x, y \pm \Delta y) = u(x, y) \pm \Delta y \frac{\partial u}{\partial y} + \frac{1}{2!} \Delta y^2 \frac{\partial^2 u}{\partial y^2} + O(\Delta y^3) \quad (2.3.2)$$

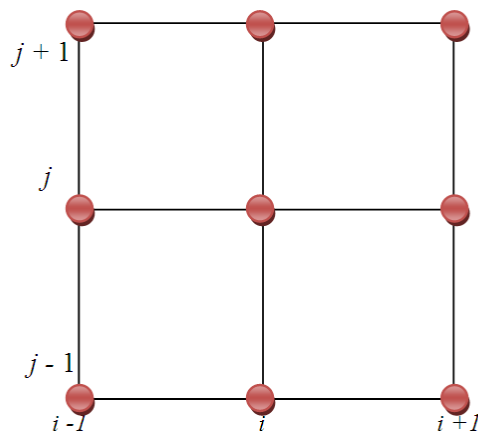


Figure 2.7: A regular grid of points to show that we can use the notation $u(x, y) = u_{i,j}$,

$$u(x + \Delta x, y) = u_{i+1,j} \text{ and } u(x, y + \Delta y) = u_{i,j+1},$$

$$u_{i \pm 1, j} = u_{i, j} \pm \Delta x \left. \frac{\partial u}{\partial x} \right|_{i, j} + \frac{1}{2} \Delta x^2 \left. \frac{\partial^2 u}{\partial x^2} \right|_{i, j} + O(\Delta x^3) \quad (2.3.3)$$

$$u_{i, j \pm 1} = u_{i, j} \pm \Delta y \left. \frac{\partial u}{\partial y} \right|_{i, j} + \frac{1}{2} \Delta y^2 \left. \frac{\partial^2 u}{\partial y^2} \right|_{i, j} + O(\Delta y^3) \quad (2.3.4)$$

$$\left. \frac{\partial u}{\partial x} \right|_{i, j} = \frac{u_{i+1, j} - u_{i, j}}{\Delta x} + O(\Delta x) \quad (2.3.5)$$

$$\left. \frac{\partial u}{\partial x} \right|_{i, j} = \frac{u_{i, j} - u_{i-1, j}}{\Delta x} + O(\Delta x) \quad (2.3.6)$$

$$\left. \frac{\partial u}{\partial x} \right|_{i, j} = \frac{u_{i+1, j} - u_{i-1, j}}{2\Delta x} + O(\Delta x^2) \quad (2.3.7)$$

$$\left. \frac{\partial^2 u}{\partial x^2} \right|_{i, j} = \frac{u_{i+1, j} - 2u_{i, j} + u_{i-1, j}}{\Delta x^2} + O(\Delta x^2) \quad (2.3.8)$$

central difference equation 2.3.8. It is worth noting that higher order finite difference approximations can be obtained by taking more terms in the Taylor series expansion. By substituting these approximations into the PDE for the differentials we arrive at the discretized equation of the PDE. There are several methods that are used to solve the discretized equations such as explicit method, implicit and semi implicit method however this will be discussed later in the chapter. It is worth pointing out that the boundary nodes can take two forms: firstly Dirichlet conditions where variable values are given and no equation is needed, and secondly Neumann conditions which involve derivatives. For both conditions it must be discretized to contribute to the equations that must be solved. Furthermore the advantage of using the FD scheme is that it's easy to implement and it's easier to obtain higher order derivatives. However the method is confined to only using a

structured grid which may not be conserved.

2.3.2.2 Finite Volume

The finite volume scheme is similar to the finite difference and finite element where the values are calculated on discrete places on a mesh. It is based on small control volumes where each volume encloses a grid node; this can be seen in Figure 2.8 (which was drawn by myself).

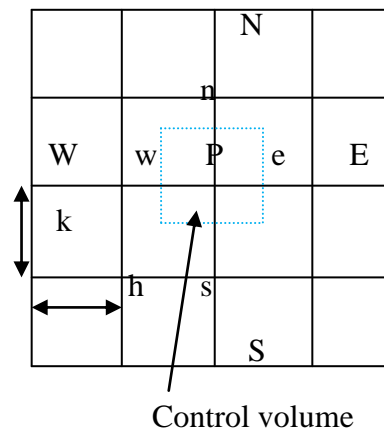
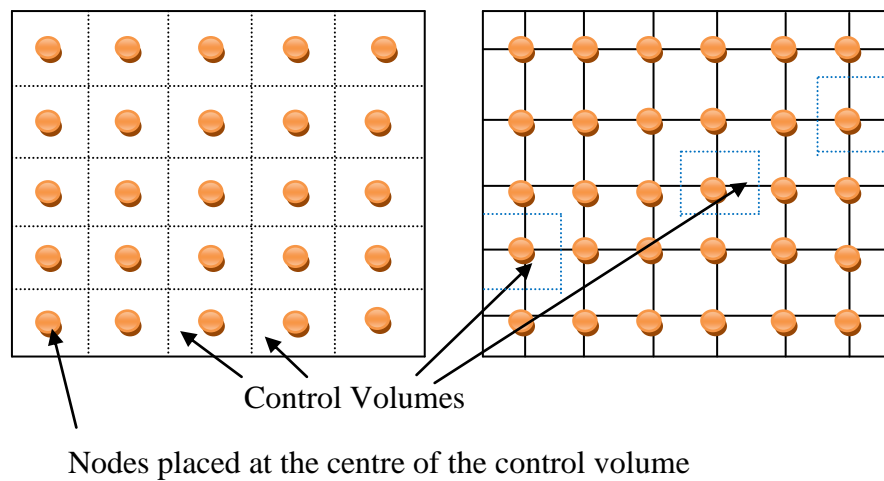


Figure 2.8: Shows the grid generation of finite volume method with control volumes (CV) and compass notations.

The scheme utilizes the fact that volume integrals in a PDE contains a divergent, using the divergence theorem shown in equation 2.3.9 we are able to relate the flow on the surface of the control volume to the interior.

$$\iiint_V (\nabla \cdot F) dV = \oiint_S F \cdot n dS \quad (2.3.9)$$

By approximating the flow on the surface of each control volume we are then able to calculate a solution for the dependent variable at each grid node. Furthermore I would like to note, due to the flux entering a given volume is identical to the flux leaving the adjacent volume the scheme is conserved. To generate the grid we place nodes across a domain and control volumes around them. Control volumes faces (boundaries) are placed midway between adjacent nodes. For the case of boundary nodes it is common practice to ensure that the boundary lies on a control volume face. Compass notations are usually used to denote each control volume face, e.g. central control volume is (P) and its East and West neighbors are (E) and (W). The East and the West faces of the control volume (P) are (e) and (w) respectively (Figure 2.8). One of the advantages of the finite volume scheme compared to the finite difference method is that it can be used on unstructured meshes and still be conserved, which is not true for the finite difference scheme where a structured mesh is required. However there are difficulties in approximating higher order derivatives for the finite volume scheme unlike the finite difference method.

2.3.2.3 Finite Element

The basic idea behind the finite element method is that the unknown $u(x,y)$ forms the surface over a domain. The finite element method approximates this surface using a piecewise linear function which is comprised of polynomials of fixed degree. The finite element method typically requires the minimisation of functional involving integrals. In practice it also requires the solution of a large linear system for the U_i at the mesh nodes

- $U_i(x_1, y_1) = a + bx_1 + cy_1$
- $U_i(x_2, y_2) = a + bx_2 + cy_2$
- $U_i(x_3, y_3) = a + bx_3 + cy_3$

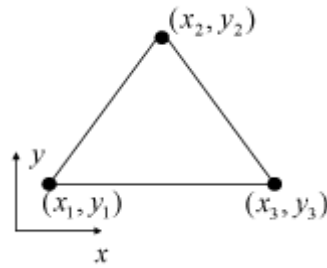


Figure 2.9: Example of triangle used to approximate $u(x, y)$ over the element by the linear function

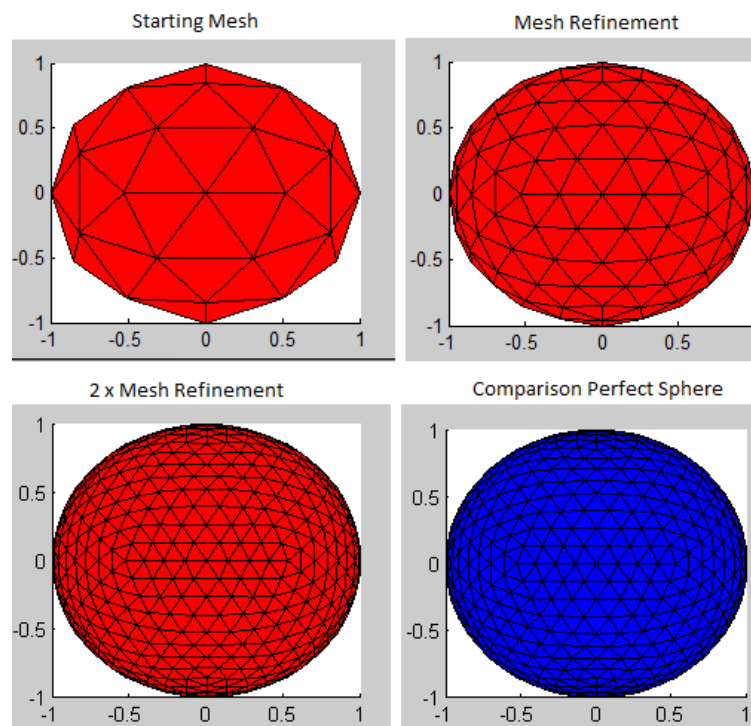


Figure 2.10: This image demonstrates mesh refinement. The image was taken from [mathworks]

(the corners of each triangle). The domain is made up of triangles T_i (the elements) and uses a linear function, U_i on each triangle. Thus $u(x,y)$ is approximated over the element by the linear function $U_i(x,y)$ to give $U_i(x,y) = a + bx + cy$, where a , b and c are constants and calculated by the method (also see Figure 2.9). The collection of triangular elements is known as an unstructured mesh, the elements can also be rectangles or other shapes providing they fit together well and cover the domain. Mesh refinement is commonly used for the finite element method to improve the accuracy; the easiest way is to divide each triangle into four smaller triangles by bisecting each edge (Figure 2.10).

2.3.2.4 Spectral methods

For the case of spectral methods the spatial derivatives are evaluated using Fourier series, the simplest method deals with periodic functions where values are uniformly spaced points. Therefore its function can be represented by a discrete Fourier series:

$$f(x_i) = \sum_{q=-N/2}^{\frac{N}{2}-1} \hat{f}(k_q) e^{ik_q x_i} \quad (2.3.10)$$

- $x_i = i\Delta x$
- $i = 1, 2, \dots, N$
- $k_q = 2\pi q / \Delta x N$

Re arrangement of equation 2.3.10 can lead to the form:

$$\hat{f}(k_q) = \frac{1}{N} \sum_{i=1}^N f(x_i) e^{-ik_q x_i} \quad (2.3.11)$$

Equation 2.3.11 can be used to interpolate $f(x)$ and this is what makes these series useful, hence the continuous variable x can replace the discrete variable x_i , therefore $f(x)$ is then defined for all x , not just the grid points. Next the choice of the range of q is very important as different sets of q produces different interpolation, it is important to choose a set which gives rise to the smoothest interpolation. After defining the interpolation one can differentiate it to give a Fourier's series for derivatives. For our case it gives rise to:

$$\frac{df}{dx} = \sum_{q=-N/2}^{\frac{N}{2}-1} ik_q \hat{f}(k_q) e^{ik_q x} \quad (2.3.12)$$

Therefore this method allows one to evaluate the derivative. A key advantage of this method is that higher derivatives can be easily generalized and the error in computing the derivatives decay exponentially with N when the number of grid points N is larger than $f(x)$. This property makes spectral methods more accurate than finite difference method. Also the accuracy of the spectral scheme translates into fewer unknowns, therefore greater speed and less memory is obtained for the same accuracy in comparison to the FD scheme. Furthermore FFT can be performed easily which means implicit time stepping can be implemented. Lastly in comparison to the FD method the spectral methods typically produce smaller artificial dissipation and dissipation. Generally Pseudo-spectral method is used for evaluating PDE's using a spectral scheme.

2.3.3 Numerical methods applied

2.3.3.1 Explicit Scheme

This is one of the simplest methods where all fluxes and sources are evaluated using known values at t_n only. For the equations of control volume or grid points at the new

time line the value at that node only is the unknown, hence all the neighbouring values are evaluated at previous time levels. Therefore one can calculate the new value of the unknown node explicitly. I will demonstrate the method for the finite difference scheme by considering equation 2.3.13, which is a one dimensional PDE. By replacing the first order derivative on the LHS by the forward difference and the second order derivative on the RHS by the second order central difference we get equation 2.3.14.

$$\frac{\partial u}{\partial t} = \alpha \frac{\partial^2 u}{\partial x^2} \quad (2.3.13)$$

$$\frac{u_{i,j+1} - u_{i,j}}{\Delta t} = \alpha \frac{u_{i+1,j} - 2u_{i,j} + u_{i-1,j}}{\Delta x^2} \quad (2.3.14)$$

$$u_{i,j+1} = u_{i,j} + r(u_{i+1,j} - 2u_{i,j} + u_{i-1,j}) \quad r = \frac{\alpha \Delta t}{\Delta x^2} \quad (2.3.15)$$

Time (j+1) ↗
Time (j) ↗

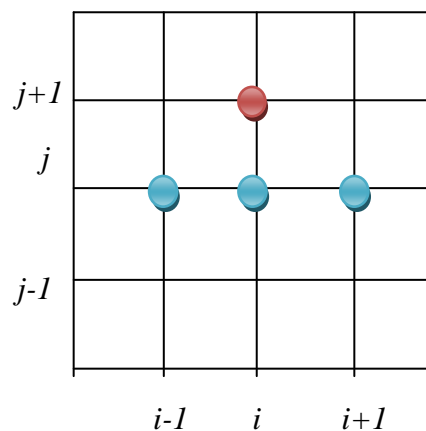


Figure 2.11: The grid demonstrates which nodes are required to calculate the explicit finite difference (the blue nodes are used to calculate the unknown node red node).

As the explicit method calculates values of the current time step only from the known values at the previous time step we can rearrange equation 2.3.14 so that on the LHS we have all the $u_{i,j+1}$ and on the RHS we have all the other terms, we get equation 2.3.15. The grid representation Figure 2.11 shows which nodes (blue nodes) are used to calculate the unknown node (red node) explicitly for equation 2.3.15. The advantage of this scheme is it's easy to implement and solve, however the disadvantage is that there are restrictions on the time step for stability.

2.3.3.2 Implicit Scheme

The key difference from the explicit method is that the implicit scheme uses more than one node at time step $j + 1$. Hence the unknown values at the current time step depend on known values at the previous time step and on each other. The scheme is always numerically stable and convergent however it is more numerically intensive than the explicit method. This is due to the method solving a system of numerical equations on each time step. The errors are linear over the time step and quadratic over the space step. I will demonstrate the method for the finite difference scheme by considering equation 2.3.13. By replacing the first order derivative on the LHS by the backwards difference and the second order derivative on the RHS by the second order central difference at $j + 1$ we get equation 2.3.16.

$$\frac{u_{i,j+1} - u_{i,j}}{\Delta t} = \alpha \frac{u_{i+1,j+1} - 2u_{i,j+1} + u_{i-1,j+1}}{\Delta x^2} \quad (2.3.16)$$

$$u_{i,j+1} - r(u_{i+1,j+1} - 2u_{i,j+1} + u_{i-1,j+1}) = u_{i,j} \quad r = \frac{\alpha \Delta t}{\Delta x^2}$$

$$(2.3.17)$$

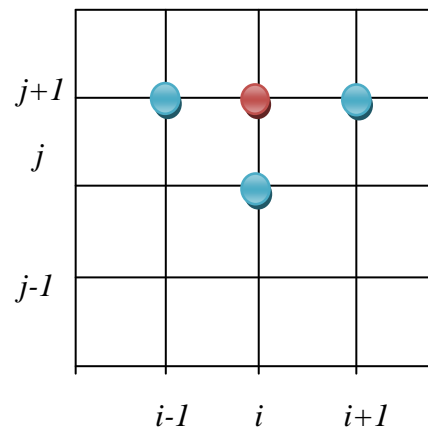


Figure 2.12: The grid demonstrates which nodes are required to calculate the implicit finite difference (the blue nodes are used to calculate the unknown node red node).

As the implicit method calculates values of the current time step on known values at the previous time step and each other we can rearrange equation 2.3.16 so that on the RHS we have all the $u_{i,j}$ and on the LHS we have all the other terms, we get equation 2.3.17. The grid representation Figure 2.12 shows which nodes (blue nodes) are used to calculate the unknown node (red node) from the implicit equation 2.3.17. The advantage of using the implicit method is that larger time steps can be used; however the method requires the solution of system of equation.

2.3.3.3 Crank-Nicholson

This method can also be considered as a semi-implicit scheme, the method not only uses known values at t_n , but it also uses more than one node at time step $j + 1$. The scheme approximates the derivative at midpoints in $(i, j+0.5)$ and is based on central difference in space and trapezoidal rule in time, giving second-order convergence in time. This scheme requires a small increase in computational effort compared to the first order implicit scheme. Furthermore using the Von Neumann stability analysis it can be shown that the Crank-Nicholson scheme is unconditionally stable and for oscillatory solutions larger

time steps are possible. The errors that are associated with this method are quadratic over the time step and formally are of the fourth degree regarding the space step.

$$\frac{u_{i,j+1} - u_{i,j}}{2(0.5\Delta t)} = \alpha \frac{1}{2} \left[\frac{u_{i+1,j} - 2u_{i,j} + u_{i-1,j}}{\Delta x^2} + \frac{u_{i+1,j+1} - 2u_{i,j+1} + u_{i-1,j+1}}{\Delta x^2} \right]$$

Central difference
Central difference
Central difference

at $(i, j + 0.5)$
at (i, j)
at $(i, j + 1)$

(2.3.18)

$$-ru_{i-1,j+1} + (2 + 2r)u_{i,j+1} - ru_{i+1,j+1} = ru_{i-1,j} + (2 - 2r)u_{i,j} + ru_{i+1,j} \quad r = \frac{\alpha\Delta t}{\Delta x^2}$$

(2.3.19)

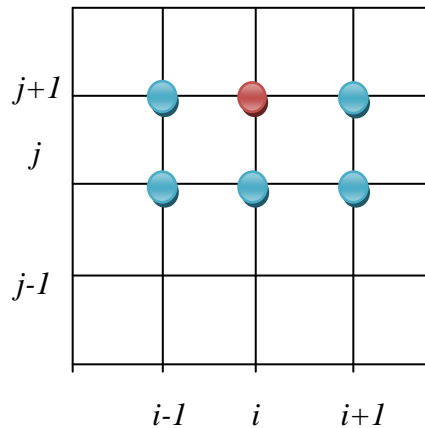


Figure 2.13: The grid demonstrates which nodes are required to calculate the Crank-Nicolson scheme (the blue nodes are used to calculate the unknown node red node).

I will demonstrate the method for the finite difference scheme by considering equation 2.3.13 for the last time. I begin by approximating the derivatives at the mid-point in time $(i, j + 0.5)$ so we get the equation 2.3.18. We can rearrange equation 2.3.18 so that on the RHS we have all the time j and on the LHS we have all the other terms, we get equation 2.3.19. The grid representation Figure 2.13 shows which nodes (blue nodes) are used to calculate the unknown node (red node) from the Crank-Nicholson equation 2.3.19.

2.3.3.4 Pseudo-spectral method

The reason why this method is preferred is due to the fact that it obtains maximum flexibility while retaining good convergence properties of the spectral approximation. Furthermore the method can be applied to PDE's with variable coefficients, nonlinearities and inhomogeneities. The spatial derivatives are evaluated by using Fourier series. The simplest methods deal with periodic functions where values are uniformly spaced points. Thus the function can be represented by a discrete Fourier series. Below I have shown an example of differentiating in spectral space and the forward and backward Euler time stepping in equations 2. 3.24 and 2.3.25.

Consider the operator:

$$\mathcal{L} = \frac{\partial^2}{\partial x^2} \tag{2. 3.20}$$

Using the spectral expansion:

$$U(x) = \sum_m a_m e^{i\beta_m x}, \quad \beta_m = 2\pi m/l \tag{2. 3.21}$$

$$|LU|_j \equiv [\mathcal{L}U(x)]_{x=x}$$

$$= \sum_m -\beta_m^2 a_m e^{i\beta_m x_j}$$

The second derivative in spectral space is a multiplication by $-\beta_m^2$. Therefore the second order derivative matrix in spectral space is defined as:

$$\hat{L} \equiv \begin{bmatrix} -\beta_0^2 & & & & \\ & -\beta_1^2 & & & \\ & & -\beta_1^2 & & \\ & & & \ddots & \\ & & & & -\beta_{j/2}^2 \end{bmatrix} = \text{diag}(-\beta_m^2)$$

Implementing this in spectral space using Fast Fourier's Transformations FFT in an individual steps can be seen below:

$$LU = \mathbf{FFT}^{-1} \hat{L} \mathbf{FFT} U \quad (2.3.22)$$

Forward Euler time stepping:

$$\frac{\partial u}{\partial t} \simeq \frac{U^{n+1} - U^n}{\Delta t} = LU^n$$

Then it becomes equation 2.3.23 where I is the identity matrix:

$$U^{n+1} = (I + \Delta t L) U^n = LU^n \quad (2.3.23)$$

$$U^{n+1} = \mathbf{FFT}^{-1} (I + \Delta t \hat{L}) \mathbf{FFT} U^n \quad (2.3.24)$$

Backward Euler time stepping:

$$U^{n+1} = \mathbf{FFT}^{-1}(I + \Delta t L)^{-1} \mathbf{FFT} U^n \quad (2.3.25)$$

2.3.3.5 Operator Splitting

Operator splitting techniques are considered as being amongst the most efficient methods for solving complex PDEs applied in physics. The basic concept is that the spatial differential operator is split into a sum of sub-operators that have simpler forms and can be handled easier. Accordingly, the original problem is replaced by a sequence of sub-problems solved numerically. The method can be generalized in the following steps taken from [Farago, 2007]:

- Select a small positive time step (τ) and then divide the whole time interval into sub-intervals of length τ ;
- On each sub-interval you consecutively solve the time dependent problems, each of which involves only one physical process;
- Then pass to the next time sub-interval.

There are three traditional operator techniques that can be implemented which are Sequential splitting, Strang-Marchuk splitting and symmetrically weighted sequential splitting. In addition to this, two new techniques for splitting have been suggested by I. Farago [Farago, 2007], that are called Iterated splitting and Adaptive splitting. An example of sequential splitting that demonstrates the basic properties of the technique is presented below [Farago, Geiser, 2006] and in [Farago, Havasi, 2005b].

Let us consider the case of two linear operators:

$$\frac{\partial c(t)}{\partial t} = Ac(t) + Bc(t), \quad \text{with } t \in [0, T], \quad c(0) = c_0 \quad (2.3.26)$$

The sequential operator split of A-B can be represented as:

$$\frac{\partial c^*(t)}{\partial t} = Ac^*(t), \quad \text{with } t \in [t^n, t^{n+1}] \text{ and } c^*(t^n) = c_{sp}^n \quad (2.3.27)$$

$$\frac{\partial c^{**}(t)}{\partial t} = Bc^{**}(t), \quad \text{with } t \in [t^n, t^{n+1}] \text{ and } c^*(t^{n+1}) = c^{**}(t^n) \quad (2.3.28)$$

For $n = 0, 1, \dots, N-1$ where $c_{sp}^n = c_0$ is given by (2.3.26), the approximated split solution at the point $t = t^{n+1}$ is then defined as $c_{sp}^{n+1} = c^{**}(t^{n+1})$.

We applied this approach for solving the coupled equations of motion of the binary PFC model, which has not previously been done. The team have specifically used spectral scheme and splitting the discretization as this leads to diagonal matrices.

Chapter 3

PHASE FIELD CRYSTAL (PFC) METHOD

Introduction

The Phase Field Crystal (PFC) method is a simple dynamical density functional theory which offers microscopic description and describes crystallisation of the liquid on the diffusive timescale. Being a density functional theory, the model naturally incorporates elastic and plastic deformation, multiple orientations and anisotropies and offers an atomistic description of the crystal growth for the melt. The PFC equation of motion is formulated so that it finds the minimum free energy path during time evolution.

3.1 Single component PFC

3.1.1 Single component (pure material) PFC

The following subsection shows the derivation of the free energy functional for the single component case as proposed by Elder *et al* in 2006. For a detailed derivation the reader is advised to read through Appendix A which shows the full derivation given in [Elder *et al*, 2006]. Within this subsection I am also going to provide the numerical scheme that was used to solve the equation of motion to provide the simulations in the first part of chapter 4. The reader should note the numerical scheme was developed by my research team;

however I have used this as a tool for the subsequent simulations shown in the early part of the results chapter.

The starting point in defining the equations for the PFC is the Classical Density Functional Theory (DFT). In this theory the characterization of the local physical state is given by time-averaged densities which are uniform in the liquid and periodic in the solid, rigorous mathematical proof of this has been provided by Ramakrishnan and Yussouff [Ramakrishnan, Yussouff, 1979]. As being part of the perturbative DFT, which uses the homogeneous liquid as a reference, the free energy of the solid is then Taylor expanded relative to the liquid to give equation 3.1.1.

$$\begin{aligned} \frac{\mathcal{F}}{KT} = & \int dr \left[\rho \ln \left(\frac{\rho}{\rho_L^{ref}} \right) - \Delta\rho \right] \\ & - 1/2 \iint dr_1 dr_2 [\Delta\rho(r_1) C(r_1, r_2) \Delta\rho(r_2)] \end{aligned} \quad (3.1.1)$$

- K is the Boltzmann's coefficient.
- $\Delta\rho = \rho - \rho_L^{ref}$ this is assumed to be a small quantity.
- $c(r_1, r_2)$ is the two particle direct correlation function of the referenced liquid.

Equation 3.1.1 is a non-local functional; therefore, the equation of motion is an integro-differential equation. The next step is to simplify the mathematical task, so we introduce the rescaled density via equation 3.1.2 and substitute it into equation 3.1.1. Finally we Taylor expand the logarithmic term in \mathcal{F} up to n^4 which gives equation 3.1.3.

$$n \equiv (\rho - \rho_L^{ref}) / \rho_L^{ref} \quad (3.1.2)$$

$$\frac{\mathcal{F}}{\rho_L^{ref} KT} \approx \int dr \left[n \frac{1 - \rho_L^{ref} C}{2} n - \frac{n^3}{6} + \frac{n^4}{12} - \dots \right] \quad (3.1.3)$$

Next we Taylor expanded the direct correlation function in Fourier space giving equation 3.1.4.

$$\hat{c}(k) = \hat{c}_0 + \hat{c}_2 k^2 + \hat{c}_4 k^4 + \dots \quad (3.1.4)$$

- $\hat{c}(k)$ has the first peak at $k = 2\pi/\sigma$.
- σ is the inter particle distance.

Then equation 3.1.4 is transformed back to real space, yielding

$$\hat{c} = (\hat{c}_0 - \hat{c}_2 \nabla^2 + \hat{c}_4 \nabla^4 - \dots) \delta(r_1 - r_2) \quad (3.1.5)$$

All physical information concerning the solidifying system is buried into the expansion coefficients of the two-point correlation function, which can be related to measurable properties such as the compressibility of the liquid, the bulk modulus of the crystal and its lattice constant. Figure 3.1(a) shows the liquid state lying on the liquidus line of the solid-liquid which is for a pure material. The coexistence region is represented by the shaded area. Also Figure 3.1 (b) shows the typical liquid state two-point correlation function compared to the power series approximation. One can see that the approximation is

reasonably close to the experimental two-point correlation function allowing the evaluation of the parameters of the PFC model:

1. The isothermal compressibility of the liquid ($\sim (1 - \rho_L^{ref} \hat{c}_0)$), which is \hat{c}_0 when $K = 0$ in Figure 3.1b.
2. The bulk modulus of the crystal ($\sim (\rho_L^{ref} \hat{c}_2^2 / |\hat{c}_4|)$), which is associated with the height of the first peak \hat{c}_2 in Figure 3.1b.
3. The lattice constant ($\sim (\hat{c}_2 / |\hat{c}_4|)^{1/2}$), which is the position of the first peak \hat{c}_4 in Figure 3.1b.

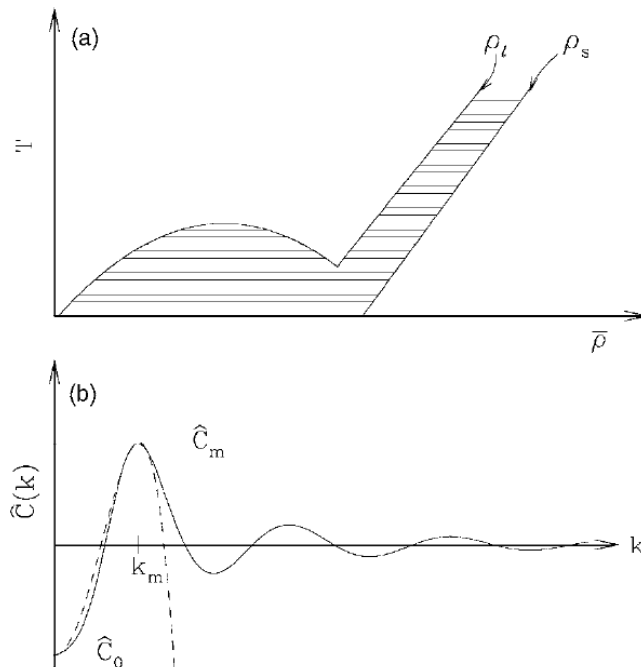


Figure 3.1 (a) A sample phase diagram, representing the coexistence region by the shaded area ($\bar{\rho}$ is the average number density). (b) Two-point direct correlation function at liquid state is also shown together with the approximation made in the PFC (dashed line).[Elder *et al*, 2007].

Substituting 3.1.5 into 3.1.3 the PFC free energy takes the form:

$$\frac{\mathcal{F}}{\rho_L^{ref} KT} = \int dr \left\{ \frac{n}{2} [B_L + B_S(2R^2 \nabla^2 + R^4 \nabla^4)] n - v \frac{n^3}{6} + \frac{n^4}{12} \right\} \quad (3.1.6)$$

- $B_L = 1 - c_0$, Which is the equivalent to $(1/\mathcal{K})/(\rho_L^{ref} KT)$, where \mathcal{K} is the compressibility.
- $B_S = |b_2|^2/(4|b_4|)$, Which is the equivalent to $K/(\rho_L^{ref} KT)$, where K is the bulk modulus of the crystal.
- $R = \sigma (2|b_4|/|b_2|)^{1/2}$.
- One should note that the v term in equation 3.1.6 accounts for the 0th order contribution from the 3 particle correlation function.
- $b_j = \hat{c}_j / 2\pi^j$, where \hat{c}_j are the coefficients of the polynomial expression for the Fourier's transformation $\hat{c}(k)$.

By introducing dimensionless variables, one may obtain a dimensionless form of the PFC free energy, which is equivalent to the Brazowskii/Swift-Hohenberg free energy functional equation 3.1.7, as shown by Elder in the following papers [Elder *et al*, 2002, 2004].

Introduced dimensionless variable:

$$x = R \cdot \bar{x}$$

$$n = (3B_s)^{1/2} \varphi$$

$$\mathcal{F} = (3\rho_L^{ref} KTR^d B_s^2) \cdot \tilde{\mathcal{F}}$$

We obtain:

$$\tilde{\mathcal{F}} = \int d\tilde{r} \left\{ \frac{\psi}{2} [r^* + (1 + \tilde{\nabla}^2)^2] \psi + t^* \frac{\psi^3}{3} + \frac{\psi^4}{4} \right\} \quad (3.1.7)$$

In the above equation, ψ is the reduced number density, $\psi \propto \frac{(\rho - \rho_L^{ref})}{\rho_L^{ref}}$, and r^* is an effective temperature, expressible as a combination of the Taylor coefficients of the two-particle correlation function and related to the measurable quantities previously described:

1. Compressibility of the liquid.
2. Bulk modulus of the crystal.
3. Lattice constant.

$\tilde{\mathcal{F}}$ is a local functional, therefore, the equation of motion is a partial differential equation (PDE). It is also worth noting that the Swift-Hohenberg model differs from the PFC model by assuming non-conserved dynamics (equation 3.1.8); whereas in the PFC model Elder *et al* has assumed conserved dynamics described by equation 3.1.9.

$$\frac{\partial \psi}{\partial \tilde{t}} = -M \frac{\delta \tilde{\mathcal{F}}}{\delta \psi} \quad (3.1.8)$$

$$\frac{\partial \psi}{\partial \tilde{t}} = \tilde{\nabla}^2 \frac{\delta \tilde{\mathcal{F}}}{\delta \psi} + \zeta \quad (3.1.9)$$

- M is the mobility.
- ζ is a Gaussian stochastic noise term.

The motivation of this is that ψ is a reduced number density, therefore, its integral (total number of particles) is conserved throughout the time evolution of the system (mass conservation). The respective equation of motion for the single-component case reads as:

$$\frac{\partial \psi}{\partial \tilde{t}} = \tilde{\nabla}^2 \{ [r^* + (1 + \tilde{\nabla}^2)^2] \psi + t^* \psi^2 + \psi^3 \} \quad (3.1.10)$$

The initial parameters of the model are as follows:

- $r^* = \Delta B / B_s = (1 + |b_0|) / [|b_2|^2 / (4|b_4|)]^{-1}$ which is the reduced temperature.
- ψ is the reduced number density, $\psi \propto \frac{(\rho - \rho_L^{ref})}{\rho_L^{ref}}$

Because $t^* = 0$ the final form of the equation of motion stands as:

$$\frac{\partial \psi}{\partial \tilde{t}} = \tilde{\nabla}^2 \{ [r^* + (1 + \tilde{\nabla}^2)^2] \psi + \psi^3 \} \quad (3.1.11)$$

The reader should be aware of the phase diagram for the single-component system, which is shown in Figure 3.2. Here there are three phases that are of interest:

- **Region 1** – Is the striped phase. The respective region in the phase diagram is of interest only for polymer studies.

- **Region 2** – Is the 2d hexagonal crystal phase. The respective region in the phase diagram is where the stable phase is the crystal and where my simulations (to be presented in the next chapter) have been conducted.
- **Region 3** – Is the homogenous liquid phase.

There are two more areas in the phase diagram labelled as Region 4 and Region 5 which stand for the coexistence regions between the striped and hexagonal phases (Region 4 on the left) and the homogenous liquid and crystal (Region 5 on the right).

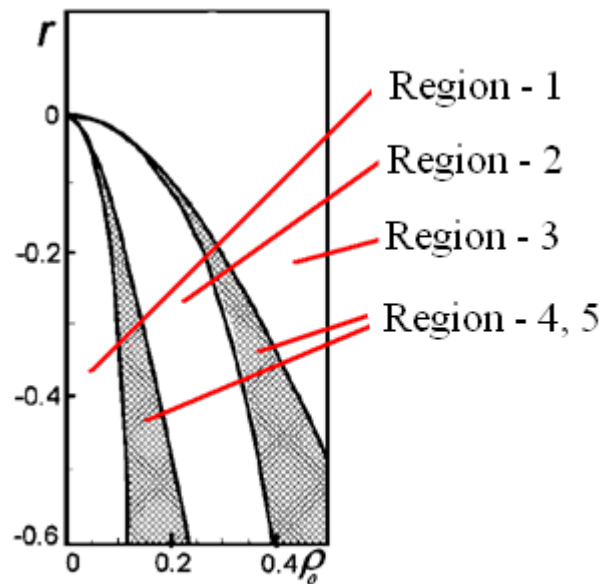


Figure 3.2 Displays the phase diagram of the single-component PFC model described above (The figure was taken from [Provatas *et al*, 2007]), r is the reduced temperature and ρ_0 is the average number density.

3.1.2 Numerical scheme for the single component (pure material) PFC

First I would like to mention that there exist several splitting procedures [Strang, 1968], [Marchuk, 1988], [Farago, Havasi, 2005a], [Csomos, Farago, 2008], [Hundsdoerfer, Verwer, 2003], [Havasi, 2005b] and [Csomos *et al*, 2005]. For simplicity, the numerical procedure used in solving the equation of motion was sequential splitting. This was deployed in order to make the calculations more manageable. While its advantages are perhaps less apparent in the case of the single-component model, they are evident in the case of the binary version, which will be discussed in subsection 3.2.2. The concept behind the method is to split the spatial differential operator into sub-operators, which have simpler structure. The split can be seen below in 3.1.13 and 3.1.14, where 3.1.13 is the collection of the non-linear terms and 3.1.14 is the collection of linear terms. For our simulations A_1 is solved by explicit spectral scheme and A_2 is solved by implicit spectral scheme.

$$\frac{\partial \psi}{\partial \bar{t}} = (A_1 + A_2)\psi \quad (3.1.12)$$

$$A_1\psi = \tilde{\nabla}^2\{\psi + \psi^3\} \quad (3.1.13)$$

$$A_2\psi = \tilde{\nabla}^2\{[r^* + (1 + \tilde{\nabla}^2)^2]\psi\} \quad (3.1.14)$$

We will use explicit Euler time stepping for the sub-operator A_1 and implicit time integration for A_2 , yielding the following equations:

$$\psi^* = \psi^t + \Delta A_1 \psi \quad (3.1.15)$$

$$\psi^{t+\Delta t} = \psi^* + \Delta A_2 \psi^{t+\Delta t} \quad (3.1.16)$$

In order to obtain an accurate solution, which is free of dissipation in handling the non-linear contributions, we have repeatedly applied Fast Fourier Transformation (FFT) by differentiation in spectral space and then inverse Fast Fourier Transformation (IFFT). The explicit time integration applied for 3.1.15 produces algebraic equations, which are written in a diagonal matrix form; therefore, they could be solved point-wise using back-substitution. For the sub-operator containing constant coefficients terms A_2 , the 2D spatial discretisation has been made spectrally. Note that the 2D Laplacian discretised in Fourier space corresponds to a $-4\pi^2(k_x^2 + k_y^2)$, where k_x and k_y are the discrete wave numbers. The final form of the splitting equations is shown by equations 3.1.17 and 3.1.18.

$$\psi^{t+\Delta t} = \psi^*(1 - \Delta t A_2)^{-1} \quad (3.1.17)$$

$$\psi^{t+\Delta t} = \psi^*(1 - \Delta t \tilde{\nabla}^2 \{ [r^* + (1 + \tilde{\nabla}^2)^2] \})^{-1} \quad (3.1.18)$$

The above equations realize a conditional time stepping however in the results chapter we make comparison to unconditionally stable time stepping. The difference from unconditionally stable time stepping is that we have treated the fourth order term explicitly in order to make the solution stable. The respective equation of motion in dimensionless terms is equation 3.1.11 and the split is displayed in equations 3.1.19 and 3.1.20.

$$A_1\psi = \tilde{\nabla}^2\{\psi^3 + \tilde{\nabla}^2\psi\} \quad (3.1.19)$$

$$A_2\psi = \tilde{\nabla}^2\{[r^* + 2\tilde{\nabla}^2 + 1]\psi\} \quad (3.1.20)$$

The discretised Laplacian in 2D Fourier space corresponds to a $-4\pi^2(k_x^2 + k_y^2)$, where k_x and k_y are the discrete wave numbers. Thus the final forms can be seen below in equations 3.1.21 and 3.1.22.

$$\psi^{t+\Delta t} = \psi^*(1 - \Delta t A_2)^{-1} \quad (3.1.21)$$

$$\psi^{t+\Delta t} = \psi^* (1 - \Delta t [\tilde{\nabla}^2 \{[r^* + 2\tilde{\nabla}^2 + 1]\}])^{-1} \quad (3.1.22)$$

3.2 Binary PFC

3.2.1 Binary alloy PFC

The binary case differs from the single component case in that it considers A and B atoms, still the starting point is the same as for the single component case, the Classical Density Functional Theory. Here the homogeneous binary liquid is used as a reference. The free energy of the solid is Taylor expanded relative to the liquid yielding equation 3.2.1

$$\begin{aligned}
\frac{\mathcal{F}}{K_B T} = & \int \overline{d\mathbf{r}} \left[\rho_A \ln \left(\frac{\rho_A}{\rho_L^A} \right) - \Delta \rho_A + \rho_B \ln \left(\frac{\rho_B}{\rho_L^B} \right) - \Delta \rho_B \right] \\
& - \frac{1}{2} \int \overline{d\mathbf{r}_1 d\mathbf{r}_2} \left[\Delta \rho_A(\overline{\mathbf{r}_1}) C_{AA}(\overline{\mathbf{r}_1}, \overline{\mathbf{r}_2}) \Delta \rho_A(\overline{\mathbf{r}_2}) \right. \\
& \quad + \Delta \rho_B(\overline{\mathbf{r}_1}) C_{BB}(\overline{\mathbf{r}_1}, \overline{\mathbf{r}_2}) \Delta \rho_B(\overline{\mathbf{r}_2}) \\
& \quad \left. + 2 \Delta \rho_A(\overline{\mathbf{r}_1}) C_{AB}(\overline{\mathbf{r}_1}, \overline{\mathbf{r}_2}) \Delta \rho_B(\overline{\mathbf{r}_2}) \right]
\end{aligned} \tag{3.2.1}$$

- (L) Corresponds to the referenced homogeneous binary liquid.
- ρ_i is the number density of the i^{th} species
- C^{ij} is the two-particle partial direct correlation function
- $\delta \rho_i = \rho_i - \rho_{i,L}$

Analogously to the single component case, the direct correlation function is Taylor expanded up to the 4th order in Fourier Space:

$$\hat{C}_{ij} = \hat{C}_{ij}^0 + \hat{C}_{ij}^2 k^2 + \hat{C}_{ij}^4 k^4 + \dots \tag{3.2.2}$$

Then this is transformed back into real space as

$$\hat{C}_{ij} = (\hat{C}_{ij}^0 - \hat{C}_{ij}^2 \nabla^2 + \hat{C}_{ij}^4 \nabla^4 - \dots) \delta(\overline{\mathbf{r}_1} - \overline{\mathbf{r}_2}) \tag{3.2.3}$$

The partial direct correlation functions C_{ij} can be related to experimental or computed partial structure factors [Woodhead-Galloway, Gaskell, 1968] and related in turn to:

1. Compressibility of the liquid.
2. Bulk modulus of the crystal.
3. Lattice constant.

By introducing new variables that represent the partial number density differences shown in 3.2.4 and 3.2.5 to 3.2.1, one can expand the resultant equation around $\delta N = 0$ and $n = 0$ thus obtaining the free energy in the form shown in equation 3.2.6 (note that coefficients t and v follows from the power series expansion):

$$n = n_A + n_B \tag{3.2.4}$$

$$\delta N = (n_B - n_A) + \frac{\rho_L^B - \rho_L^A}{\rho_L} \tag{3.2.5}$$

- $n_A = \frac{\rho_A - \rho_L^A}{\rho_L}$
- $n_B = \frac{\rho_B - \rho_L^B}{\rho_L}$

The Free Energy form (note that with exception to n and δN the rest of the coefficients comes from the expansion of the direct correlation function):

$$\begin{aligned} \frac{\mathcal{F}}{\rho_L K_B T} = & \int \overline{dr} \left(\frac{n}{2} [B_L + B_S(2R^2 \nabla^2 + R^4 \nabla^4)] n \right. \\ & + \frac{t}{3} n^3 + \frac{v}{4} n^4 + \gamma(\delta N) + \frac{w}{2} (\delta N)^2 + \frac{u}{4} (\delta N)^4 \\ & \left. + \frac{L^2}{2} |\vec{\nabla}(\delta N)|^2 + \dots \right) \end{aligned}$$

(3.2.6)

The initial parameters of the model are as follows:

- n corresponds to the number density.
- δN corresponds to the total number density.
- B_L is related to the compressibility of the liquid.
- B_S is the Bulk modulus of the crystal.
- R is the inter-atomic distance.
- v is a constant from the Taylor expansion of \ln .
- t is a constant from the expansion of \ln , however it can be changed to incorporate 3- particle correlation to 0th order.
- γ is the coefficient of the linear terms and comes from the expansion.
- L^2 is the coefficient of the square-gradient term that is related to the chemical contribution to the phase boundaries.
- u, w magnitude and sign will decide whether there is phase separation in the liquid; with appropriate signs they can produce a double well free energy as a function of δN .

As in the single component case, Elder has assumed conserved dynamics for the particle densities, yielding equation 3.2.7 as the equation of motion for total particle density, and equation 3.2.8 as the equation of motion for the particle density difference (related to concentration).

$$\frac{\partial n}{\partial t} = M_e \nabla^2 \frac{\delta \mathcal{F}}{\delta n} \quad (3.2.7)$$

$$\frac{\partial(\delta N)}{\partial t} = M_e \nabla^2 \frac{\delta \mathcal{F}}{\delta(\delta N)} \quad (3.2.8)$$

- $M_e \equiv \frac{2M}{\rho_L^2}$

In order to produce the equation of motion and concentration from equation 3.2.6, we need equation 3.2.9 that defines the functional derivative in case of higher differential operators [see e.g. Musicki, 1978]:

$$\frac{\delta \mathcal{F}}{\delta \chi} = \frac{\partial I}{\partial \chi} + \sum_i (-1)^i \nabla^i \frac{\partial I}{\partial \nabla^i \chi} \quad (3.2.9)$$

The form for n :

$$\frac{\delta \mathcal{F}}{\delta n} = \frac{\partial I}{\partial n} + \sum_i (-1)^i \nabla^i \frac{\partial I}{\partial \nabla^i n}$$

The form for δN :

$$\frac{\delta \mathcal{F}}{\delta N} = \frac{\partial I}{\partial (\delta N)} + \sum_i (-1)^i \nabla^i \frac{\partial I}{\partial \nabla^i (\delta N)}$$

Equation 3.2.9 is the first functional derivative of the free energy with respect to χ , where I is the integrand of equation 3.2.6. Next we expand the coefficients B_L , B_S and R in terms of powers δN :

$$B_L = B_0^L + B_1^L \delta N + B_2^L \delta N^2$$

$$B_S = B_0^S + B_1^S \delta N + B_2^S \delta N^2$$

$$R = R_0 + R_1 \delta N + R_2 \delta N^2$$

$$(3.2.10)$$

Assume that only B_0^L , B_2^L , B_0^S , R_0 and R_1 differ from zero, then insert the respective form into equations 3.2.7 and 3.2.8, after straightforward manipulation of the equations, the motions for the binary PFC model take the following form:

$$\begin{aligned} \frac{\partial n}{\partial t} = & M_e \nabla^2 [n[B_0^L + B_2^L \delta N^2] + tn^2 + vn^3 \\ & + \frac{B_0^S}{2} \{2[R_0 + R_1 \delta N]^2 \nabla^2 + [R_0 + R_1 \delta N]^4 \nabla^4\} n \\ & + \frac{B_0^S}{2} \{2\nabla^2 (n[R_0 + R_1 \delta N]^2) + \nabla^4 (n[R_0 + R_1 \delta N]^4)\} \end{aligned} \quad (3.2.11)$$

$$\begin{aligned} \frac{\partial(\delta N)}{\partial t} = & M_e \nabla^2 [B_2^L (\delta N) n^2 \\ & + 2B_0^S n \{[R_0 + R_1 (\delta N)] R_1 \nabla^2 + [R_0 + R_1 (\delta N)]^3 R_1 \nabla^4\} n \\ & + \gamma + w(\delta N) + u(\delta N)^3 - L^2 \nabla^2 (\delta N)] \end{aligned} \quad (3.2.12)$$

3.2.2 Numerical scheme for the Binary PFC

In solving the equation of motion and the equation of concentration we have used sequential splitting, which has previously been deployed for the single component case. The advantage of using this scheme can be clearly seen in the case of the binary PFC: by decomposing the sixth order PDE, which contains both linear and non linear terms, into sub-problems which are easier in form, we are able to solve both equations of motions numerically efficiently. I would like to note the specific split that was proposed by György Tegze in conjunction with appropriate spatial discretization reduces the computation time significantly. The sub-operators A_1 and B_1 can be solved using explicit

finite differencing or a spectral scheme, while A_2 and B_2 can be dealt with by using an implicit spectral scheme. For our case we have opted to solve A_1 and B_1 using a fully spectral approach in order to retain a high level of accuracy.

$$\frac{\partial n}{\partial t} = (A_1 + A_2)n \quad (3.2.13)$$

$$\frac{\partial(\delta N)}{\partial t} = (B_1 + B_2)(\delta N) \quad (3.2.14)$$

Where the sub-operators take the following form:

$$\begin{aligned} A_1 n = & \nabla^2 \{ [M_e \{ B_0^L + B_2^L (\delta N)^2 \} - C_1] n \} \\ & + \nabla^2 [M_e B_0^S \{ R_0 + R_1 (\delta N) \}^2 - \frac{C_2}{2}] \nabla^2 n \\ & + \nabla^2 [M_e \frac{B_0^S}{2} \{ R_0 + R_1 (\delta N) \}^4 - \frac{C_3}{2}] \nabla^4 n \\ & + \nabla^4 [M_e B_0^S \{ R_0 + R_1 (\delta N) \}^2 - \frac{C_2}{2}] n \\ & + \nabla^6 [M_e \frac{B_0^S}{2} \{ R_0 + R_1 (\delta N) \}^4 - \frac{C_3}{2}] n \\ & + \nabla^2 \{ M_e [tn^2 + vn^3] \} \end{aligned} \quad (3.2.15)$$

$$A_2 n = C_1 \nabla^2 n + C_2 \nabla^4 n + C_3 \nabla^6 n \quad (3.2.16)$$

$$B_1(\delta N) = M_e \nabla^2 [B_2^L(\delta N)n^2]$$

$$\begin{aligned}
& + 2B_0^S\{[R_0 + R_1(\delta N)]R_1\nabla^2 + [R_0 + R_1(\delta N)]^3R_1\nabla^4\}n \\
& + \gamma + w(\delta N) + u(\delta N)^3]
\end{aligned} \tag{3.2.17}$$

$$B_2(\delta N) = M_e(w\nabla^2(\delta N) - L^2\nabla^4(\delta N)) \tag{3.2.18}$$

The coefficients C_1 , C_2 and C_3 are simply constants which are used to ensure stability of the scheme, and will be discussed in detail in the later part of this subsection. The next step is to implement the sequential splitting procedure and discretization. This is done by using Euler time stepping for sub-operators A1 and B1 while first order implicit time integration has been used for the sub-operators A2 and B2, which leads to the following equations:

$$n^* = n^t + \Delta t A_1 n^t \tag{3.2.19}$$

$$n^{t+\Delta t} = n^* + \Delta t A_2 n^{t+\Delta t} \tag{3.2.20}$$

$$(\delta N)^* = (\delta N)^t + \Delta t B_1 (\delta N)^t \tag{3.2.21}$$

$$(\delta N)^{t+\Delta t} = (\delta N)^* + \Delta t B_2 (\delta N)^{t+\Delta t} \tag{3.2.22}$$

The equations for n^* and $(\delta N)^*$ contain the non-linear variables coefficients and, as in the single component case, the 2D spatial discretization has been made using spectral differencing for the constant coefficients A_2 and B_2 . Furthermore, the explicit time

integration applied for 3.2.19 and 3.2.21 produces algebraic equations, which are written in a diagonal matrix form, therefore it has been solved pointwise using back substitution. Here $\tilde{n}_{(k_x+k_y)}$ and $(\widetilde{\delta N})_{(k_x+k_y)}$ represent the discrete Fourier transformation of $n(\mathbf{r})$ and $\delta N(\mathbf{r})$. Thus one arrives to the final forms shown in equations 3.2.23 and 3.2.24.

$$\begin{aligned} \tilde{n}_{(k_x+k_y)}^{t+\Delta t} &= \tilde{n}_{(k_x+k_y)}^* \{1 - \Delta t(C_1 2^2 \pi^2 (-k_x^2 - k_y^2) \\ &\quad + C_2 2^4 \pi^4 (-k_x^4 + 2k_x^2 k_y^2 + k_y^4)) \\ &\quad + C_3 2^6 \pi^6 (-k_x^6 - 3k_x^4 k_y^2 - 3k_x^2 k_y^4 - k_y^6)\}^{-1} \end{aligned} \quad (3.2.23)$$

$$\begin{aligned} (\widetilde{\delta N})_{(k_x+k_y)}^{t+\Delta t} &= (\widetilde{\delta N})_{(k_x+k_y)}^* \{1 + \Delta t M_e w 2^2 \pi^2 (k_x^2 + k_y^2) \\ &\quad \Delta t M_e L^2 2^4 \pi^4 (-k_x^4 + 2k_x^2 k_y^2 + k_y^4)\}^{-1} \end{aligned} \quad (3.2.24)$$

Due to the mix of explicit and implicit formulations in the present scheme we were able to fine tune the stability criteria via the choice of constants C_1 , C_2 and C_3 . In this respect, Csomos and Farago [Csomos, Farago, 2008] have pointed out that due to possible interactions of the errors, fine tuning is necessary for the stability of time stepping with the individual sub-operators, which however does not automatically guarantee the stability of the full scheme. The appropriate choice of C_1 , C_2 and C_3 is discussed below.

From the result of sequential operator splitting and spectral implicit treatment of the 4th order term in the equation of motion for concentration (equation 3.2.12) one obtains $\Delta t \propto (\Delta x)^2$ as opposed to $\Delta t \propto (\Delta x)^4$ applying to the fully explicit scheme, making the proposed splitting scheme more favourable. Next, we have analysed the stability of time stepping and the consistency of the explicit and implicit time stepping for the equation of

motion (equation 3.2.11). After straightforward manipulation one obtains the form shown below (equation 3.2.25), which displays the terms added to the fully explicit discretization equation. From this one observes that as Δt tends to zero the extra terms tend to zero as well, which demonstrates that the consistency of the scheme was ensured.

$$\Delta t M_e [C_1 (\nabla^2 n^{t+1} - \nabla^2 n^t) + C_2 (\nabla^4 n^{t+1} - \nabla^4 n^t) + C_3 (\nabla^6 n^{t+1} - \nabla^6 n^t)] \quad (3.2.25)$$

Next we discuss the stability of time stepping. We define the coefficients C_1 , C_2 and C_3 , as specified by equations 3.2.26, 3.2.27 and 3.2.28. As previously stated, the proper choice of these coefficients allow us to modify the stability criteria, thus for every time step and mesh spacing we are able to choose these coefficients so that the stability of the explicit terms is retained. This choice of the coefficients forces the maximum of the variable coefficients 2nd and 6th order terms into a range, where the differencing terms are stable for given time step and mesh space. The 4th order term was not required to ensure stability, as all the variable coefficients are positive in practice. The choices of C_1 and C_3 shown below ensure the stability of explicit time stepping:

$$C_1 = |M_e \{B_0^L + B_2^L (\delta N)^2\}|_{max} \quad (3.2.26)$$

$$C_2 = |2M_e B_0^S \{R_0 + R_1 (\delta N)\}^2|_{max} \quad (3.2.27)$$

$$C_3 = |M_e B_0^S \{R_0 + R_1 (\delta N)\}^4|_{max} \quad (3.2.28)$$

Nevertheless one should consider implicit time stepping and ensure its stability. With regards to this the BCAST research team suggested that the stability is dependent on the wave factor k which has been formulated so that the condition restricts the coefficient C_2 value. This can be seen in the equation below.

$$\Delta t M_e \left[C_1 2^2 \pi^2 (k_x^2 + k_y^2) - C_2 2^4 \pi^4 (k_x^2 + k_y^2)^2 + C_3 2^6 \pi^6 (k_x^2 + k_y^2)^3 \right] > -1 \quad (3.2.29)$$

One should note that, where possible, the mixing of explicit and implicit terms within numerical schemes should be avoided due to splitting errors that may occur. In this work we have utilized the fact that the coefficient varies only slightly due to the composition dependence of inter atomic distance represented by $R = R_0 + R_1(\delta N)$, which is typically small itself. Therefore, as C_2 is represented by equation 3.2.27, the dominant terms are the variable coefficients, which are then treated in an implicit manner and the explicit part is used as small correction. Thus the representation of C_2 (equation 3.2.27) satisfies the implicit stepping stability condition.

The reader should also be aware that we have used spherical spectral filtering [Levin *et al*, 1997] on the non-linear terms in equation 3.2.12. The main reason for this is to avoid accumulation of errors at high frequencies, which can come from the non-linear instabilities of the numerical solution due to various choices of model parameters, as the equation of motion is highly non-linear in nature. The filter has been applied by cancelling frequencies that satisfy the condition $k_x^2 + k_y^2 > k^2$ where k is a constant which is defined empirically.

I am going to compare the proposed semi-implicit spectral scheme to the explicit finite difference method in respect to the accuracy, stability and overall computational

efficiency in a parallel environment. For the explicit finite difference method I am going to use the compact finite difference discretization of the Laplacian shown below (equation 3.2.30 taken from [Levin *et al*, 1997]).

$$\begin{aligned} \nabla^2 f_{i,j} = & [(f_{i+1,j} + f_{i-1,j} + f_{i,j+1} + f_{i,j-1})/2 \\ & + \frac{f_{i+1,j+1} + f_{i-1,j+1} + f_{i+1,j-1} + f_{i-1,j-1} - 3f_{i,j}}{4}] / (\Delta x)^2 \end{aligned} \quad (3.2.30)$$

3.2.3 Thermal Fluctuations

Within statistical mechanics we represent random deviations from the equilibrium of the system by thermal fluctuations. As temperature increases the thermal fluctuations become more frequent and larger. Furthermore as the temperature approaches absolute zero the thermal fluctuations disappear. Therefore thermal functions are a consequence of the temperature and if the system is not at absolute zero then the systems do not stay in equilibrium microscopic state. However the thermal fluctuations sample all possible states by the probabilities by the Boltzmann distribution. Thermodynamic variables, for example pressure, temperature, or entropy, all undergo thermal fluctuations and are a source of noise in many systems. In order to represent thermal fluctuations within our simulation, we have added coloured conserved Gaussian noise to the governing equation in Fourier space which was similarly done in [Garcia-Ojalvo *et al*, 1992]. In addition to this the amplitude scales with the time step and the cut-off wavelength which is shown in [Sancho *et al*, 1998]. Furthermore, to avoid the appearance of unphysical small wavelengths shorter than the inter-atomic distance, we have applied an appropriate cut-off in the Fourier space. In the case for the binary PFC simulations the cut-off for wavelengths was for wavelengths smaller than $\lambda = 7\Delta x$.

Chapter 4

RESULTS

Background

Our research team has produced and implemented a parallel C code for the Phase Field Crystal model, which relies on a MPI protocol. The MPI protocol is a message passing interface which allows computers to communicate to one another. This protocol is generally used for super computers or a cluster of computers. This code is then used to solve the governing equation specified in chapter 3 on a $N \times N$ rectangular grid. To optimise the numerical performance of the code, György Tegze has developed a Fast Fourier Transformation code, which is based on the FFTW3 library [Frigo, Johnson, 2005].

The numerical investigation presented in this thesis has been performed using two PC clusters.

1. One hosted at the Research Institute for Solid State Physics and Optics (RISSPO), Budapest, Hungary. This cluster consists of 24 PCs; equipped with two 2.33 GHz Intel processors of four CPU cores (192 CPU cores). The 24 nodes are connected by 10 Gbit/s communications (Infiniband).
2. The other is located at the Brunel Centre for Advanced Solidification Technology (BCAST), Brunel University, West London, UK. This cluster consists of 20 similar nodes (160 CPU cores), however, with 1 Gbit/s (standard GigaBit Ethernet) communication in between.

4.1 Preliminary-results: Application to Dendritic and Eutectic growth

In order to illustrate the types of problems, for the solution of which the code developed by our research team can be applied, we investigate how dendrites and eutectic structures form in computer simulations performed with this new semi-implicit PFC scheme. Firstly, we prescribe the initial conditions. The simulation window has been filled uniformly with an appropriate total number density $n = \bar{n}$ and number density difference $(\delta N) = \delta \bar{N}$. The initial conditions and model parameters used are displayed in Table 4.1. Owing to difficulties to set other kind of boundary conditions, we have prescribed periodic boundary conditions at the perimeters of the simulation window. Next, I have placed a crystal seed into the simulation box. In the case of the dendritic structure, a small crystalline cluster has been used, which consisted of 13 peaks placed on a hexagonal lattice of suitable atomic spacing. In the case of eutectic solidification I have placed 2 seeds of different compositions i.e. $(\delta N) = -0.3$ and 0.3 , respectively. Each of these seeds consisted of 7 density peaks (central atom plus the first neighbour shell) and they have been placed in contact with one another in the centre of the simulation window.

I note that these preliminary-results are here to demonstrate the potential of the scheme that I will be using in the following subsections. To explore the sensitivity of the growth morphology to the conditions/parameter settings, I have grown two dendrites under different thermodynamic driving forces tuned by varying the initial number density of the liquid phase. Next I have grown a eutectic structure, for which I changed the initial number density difference of the liquid. The respective simulation parameters can be seen in Table 4.1. The code has the built-in facility (developed by G. Tegze) of adding conserved Gaussian noise to the equations of motion to mimic the thermal fluctuations. This function of the code includes a cut-off for wavelengths that are smaller than the inter-atomic distance (i.e., $\lambda = 7\Delta x$) to avoid the high frequencies integrated into the free energy functional. The time and spatial steps I have used in these simulations are $\Delta x = \Delta x_0 = 1.1$ and $\Delta t = 32\Delta t_0 = 0.16$. The results of these illustrative simulations for crystalline solidification in binary alloys are displayed in Figure 4.1. Here the four panels represent the following:

- **(a)** Shows the number density difference (δN) map for the solute dendrite.
- **(b)** Shows a magnified view of the small square section of the dendrite in (a), which was taken from the downward pointing arm of the dendrite.
- **(c)** Shows a compact dendrite that develops when a higher driving force is used, this was done by increasing the initial liquid density.
- **(d)** Shows a eutectic structure. I have reduced the initial number density \bar{n} and number density difference $\delta\bar{N}$ relative to panel (a).

Table 4.1: Parameters used in computing Figure.4.1, description for them can be seen in subsection 3.2.1

	(a), (b)	(c)	(d)
\bar{n}	0.0092	0.0096	0.0
$\delta\bar{N}$	0.0904	0.0904	10^{-6}
B_0^L	1.04	1.04	1.0248
B_2^L	-1.8	-1.8	-1.8
B_0^S	1.0	1.0	1.0
R_0	1.0	1.0	1.0
R_1	0.25	0.25	0.25
t	-0.6	-0.6	-0.6
v	1.0	1.0	1.0
γ	0.0	0.0	0.0
w	0.088	0.088	0.0
u	4.0	4.0	4.0
L	1.2	1.2	1.2
$\Delta x/\Delta x_0$	1.0	1.0	1.0
$\Delta t/\Delta t_0$	32.0	32.0	32.0
ζ_0	10^{-6}	10^{-6}	10^{-5}
N	8,192	8,192	2,048

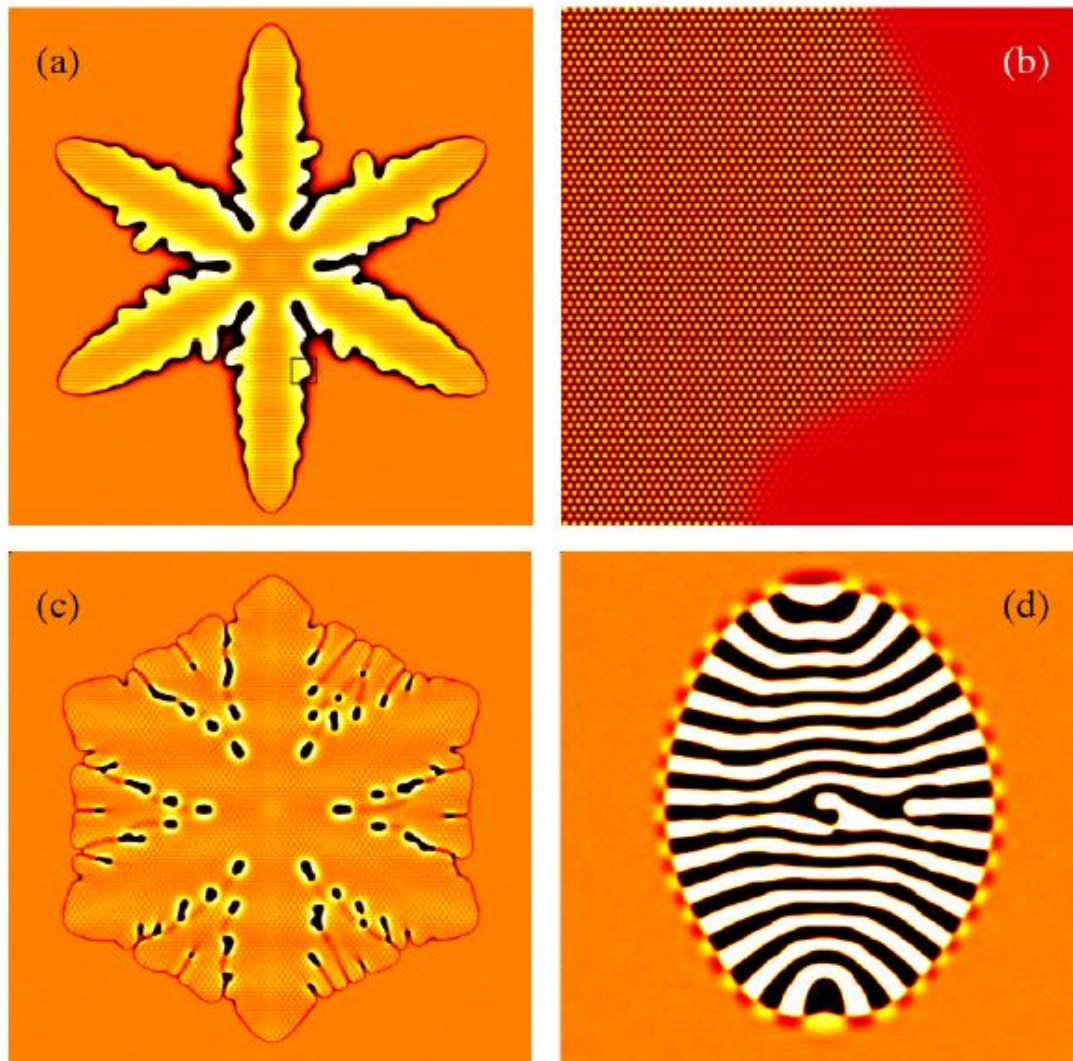


Figure 4.1: Illustrative phase-field crystal simulations for solidification in binary alloys. (a) Is a snapshot taken at 92, 160 time steps and shows the number density difference (δN) map for the solute dendrite; panel (b) shows the solid-liquid interface of the small squared section in section (a) on the downward pointing dendrite arm; panel (c) shows a compact dendrite that was formed in order to compare with (a) to demonstrate the sensitivity of the parameters (snapshot was taken at 55, 000 time steps) and lastly panel (d) demonstrates the eutectic structure that is produced with the proposed PFC, the snapshot was taken at 498, 000 time steps.

4.2 The Single Component Case

Background

The motivation for this investigation is to identify whether unconditional time stepping can be applied to the revised semi-implicit spectral scheme for the single component case which has been described in chapter 3. In short, I have treated the fourth order term explicitly in order to make the solution stable. To make comparison to the unconditional time stepping I have conducted conditional time stepping simulations and made comparisons between both schemes in terms of their relative errors. The simulations have been performed on the computer cluster of the Brunel Centre for Advanced Solidification Technology.

4.2.1 Parameters/initial conditions used in the simulations

The choice of parameters/initial conditions I have used in the simulations is given in Table 4.2. These values refer to a region of the phase diagram, in which dendritic solidification has been observed, and have been chosen inside the crystal-fluid coexistence region of the phase diagram by [Elder *et al*, 2006].

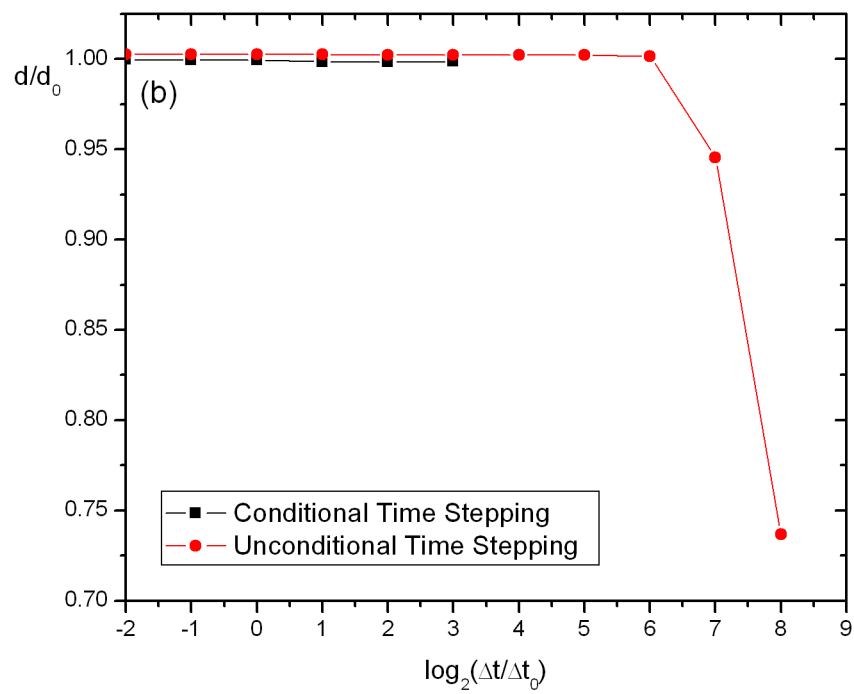
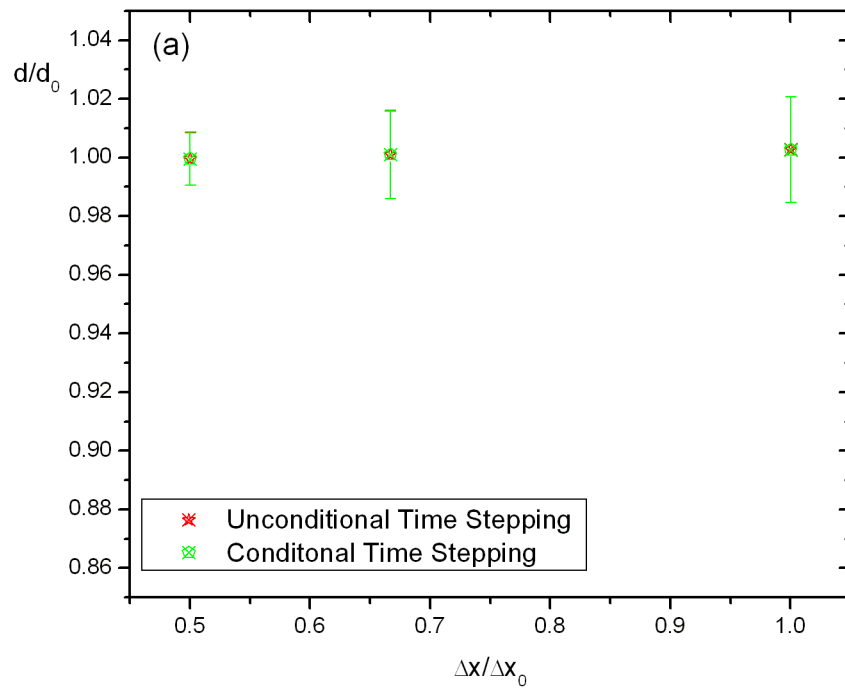
Table 4.2: Parameters used in computing the single component case for both conditional and unconditional time stepping simulations (description of parameters are presented subsection 3.2.1)

parameter	values
ψ	-0.53
r^*	-0.75
ζ_0	0.0
L	402.112

I began the simulations by first filling the simulation window with the appropriate uniform number density. Then I placed a small crystalline cluster of 19 density peaks on a hexagonal lattice (atom + first and second neighboring shells) with suitable atomic spacing in the center of the simulation window, which acted as a crystal seed. To avoid stochastic inaccuracies that may originate from the noise, and to make a quantitative comparison between computations at different time and spatial steps easier, the noise representing the thermal fluctuations has been switched off in these simulations.

4.2.2 Method of evaluation

In this investigation, I have used the diameter d of the crystal to characterize the solution as it provides information on the average growth rate and also monitors the kinetics of the phase transition. In evaluating the diameter, I have followed the same process as I have done with the binary case; the reader is advised to read the subsection 4.3.2. However, I summarize briefly the applied procedure: I have connected the maxima of the neighboring total number of density peaks along the horizontal centerline of the particles (lying on a crystal plane) by a straight line at dimensionless time $t = 768$. From this, I have taken the intersection of the resulting peak envelope with an arbitrarily chosen fixed threshold of $n = 0.075$, where the position has been then used as the limit between the solid and liquid phases. (Choice of other threshold values would lead to different data for the diameter; however, the results would remain qualitatively the same.) The uncertainty of the peak position is $2\Delta x$ on both ends of the diameter, which for our case is $\sim 113\Delta x_0$. The relative error for the diameter then becomes $\pm 2\Delta x / (113\Delta x_0)$, which varies in the range from $\pm 0.9\%$ to $\pm 1.8\%$ for the single component case. Unlike the binary case, we have not found any perceptible variation in the position of the density peaks thus I didn't evaluate the inter-atomic distance.



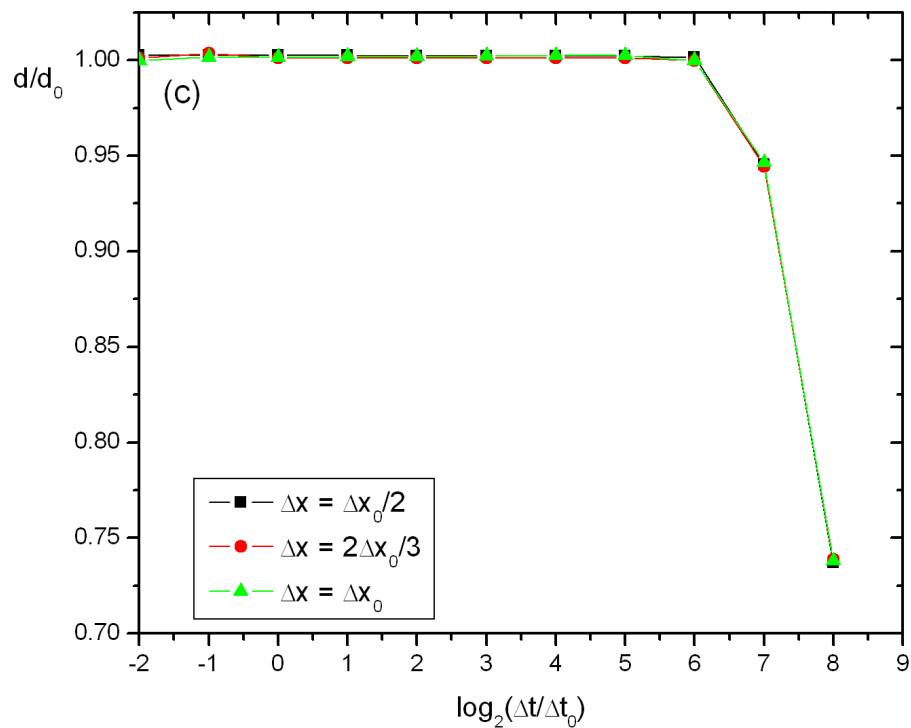


Figure 4.2: Effect of the spatial and time resolution on the numerical results obtained with the unconditional and conditional time stepping. (a) Shows diameter d Vs Δx , the points correspond to the smallest Δt where the error bars relate to the relative error. (b) Diameter d Vs Δt for both the conditional and unconditional time stepping. (c) Is the graph for unconditional time stepping for all 3 different meshes that were used.

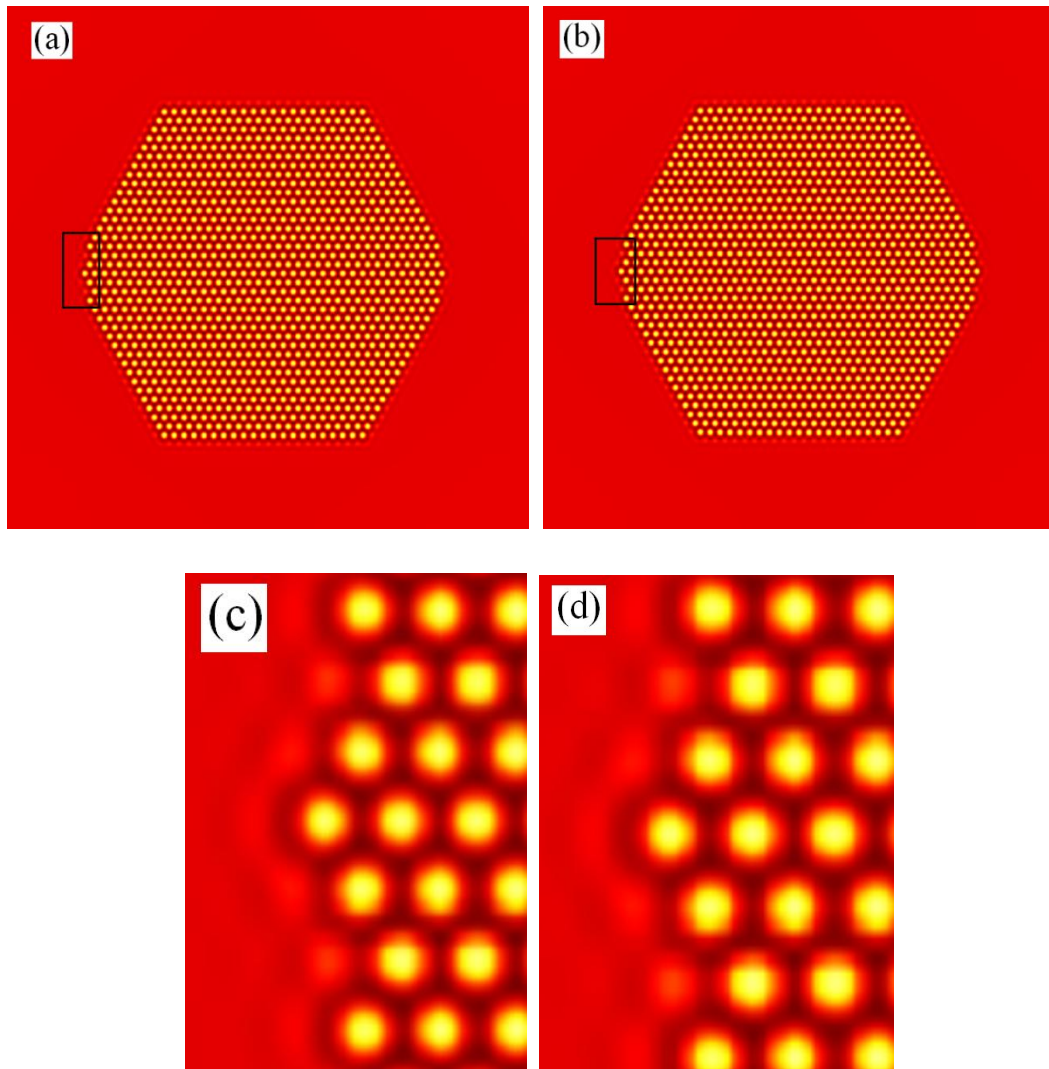


Figure 4.3: Shows the difference between the structure for conditional and unconditional time stepping. The images correspond to $t = 768$. Panel (a) displays the result from conditional time stepping at $\Delta x = \Delta x_0$ with the smallest time step; panel (b) shows the respective result from unconditional time stepping for $\Delta x = \Delta x_0$ with the smallest time step. The contents of the box placed to the left hand edge of the crystal in panels (a) and (b) are shown magnified in panel (c) for the conditional time stepping and panel (d) for unconditional time stepping. The two methods lead to fairly identical results.

4.2.3 Initial set values for simulation and results

For our study, we have set $\Delta x_0 = 0.785375$ and $\Delta t = 0.05$, while the spatial steps used were $\Delta x = (1, 2/3 \text{ and } 1/2) \times \Delta x_0$. In the case of conditional time stepping, the following simulations have been performed with the time steps $\Delta t = \frac{1}{4} \times 2^j \times \Delta t_0$, where $j = 0, 1, 2, \dots, 5$. In turn, for unconditional stepping, we have performed simulations with time steps of $\Delta t = \frac{1}{4} \times 2^j \times \Delta t_0$, $j = 0, 1, 2, \dots, 10$. The diameter $d_0 = 88.45 \times (1.0 \pm 0.0009)$ from the computation with the finest spatial and time resolution has been chosen as the reference.

4.2.3 Initial set values for simulation and results

Firstly, I would like to compare the conditional time stepping and the unconditional time stepping schemes regarding the spatial and time resolution on the numerical results. This is displayed in the Figures 4.2 (a), (b) and also in Figure 4.2 (c). Figure 4.2 (a) displays how the diameter of the crystal depends on the spatial resolution. Figure 4.2 (c) displays how the diameter of the crystal depends on the time steps Δt . I have normalised the diameter in order to identify the true variance between the conditional and unconditional schemes. In addition, I have provided further evidence of the difference between the solid liquid interfaces for both schemes in Figure 4.3.

4.3 Binary case

Background

The motivation behind this investigation is to firstly identify whether there exists a limiting solution which the SIS solution converges to for decreasing Δx and Δt . In order to conduct this investigation, I have used an empirical convergence test (see e.g. [Budd *et al*, 2006]). The rationale behind this choice is that I am unaware of any non-trivial analytical solution which could be used as a point of reference when computing the numerical error. Secondly it is commonly known that the stability criterion is severely restricted with regards to the

explicit discretization as $\Delta t \propto (\Delta x)^6$. With these limitations a sufficiently accurate explicit finite difference computation, which can potentially be used as a reference point, could not be obtained thus the only option available to me was to conduct empirical convergence tests. After identifying the limiting solution, I have then used this as the point of reference in defining and calculating the numerical error, furthermore, I will investigate if the SIS scheme converges to the EFD scheme for simulations within our range for spatial resolution and time steps. The simulations have been performed by me on the computer cluster of the Brunel Centre for Advanced Solidification Technology.

4.3.1 Parameters used in the simulations

I start with investigating the effect of the spatial and time resolution on the numerical solution obtained by the proposed SIS scheme. For the setup of the simulations in this section, similar to the previous one, we switch off the noise. The reason is similar: I wish to avoid differences of stochastic origin. Secondly the simulation window for the following sub-sections has been set to a small physical domain of dimensionless area 281.6×281.6 unless specified otherwise. The size of the simulation window contains approximately 6,600 atoms which provides a good compromise so that it's enough space to produce a crystal large enough at dimensionless time $t = 768$ to display bulk crystalline properties inside, however it is still small enough to allow refinement steps in the spatial resolution for both the SIS and EFD schemes. The parameters that were set for these simulations can be found in Table 4.1 (a). The simulations for the SIS scheme have been performed using the spatial steps $= \Delta x (1/4, 1/3, 1/2, 2/3, 3/4, \text{ and } 1) \times \Delta x_0$, also for each individual spatial step I have performed simulations with time steps $\Delta t = 2^j \times \Delta t_0$, where $j = 0, 1, 2, \dots, 8$. As I am interested in making comparisons to the SIS scheme, I have made EFD computations with the same spatial steps; however, I have used the largest time steps allowed by the numerical stability of the explicit scheme. The crystal seed that initiated growth of the dendrite was placed in the centre of the simulation window. Crystallization has been started by a crystalline seed of 13 atoms, described above.

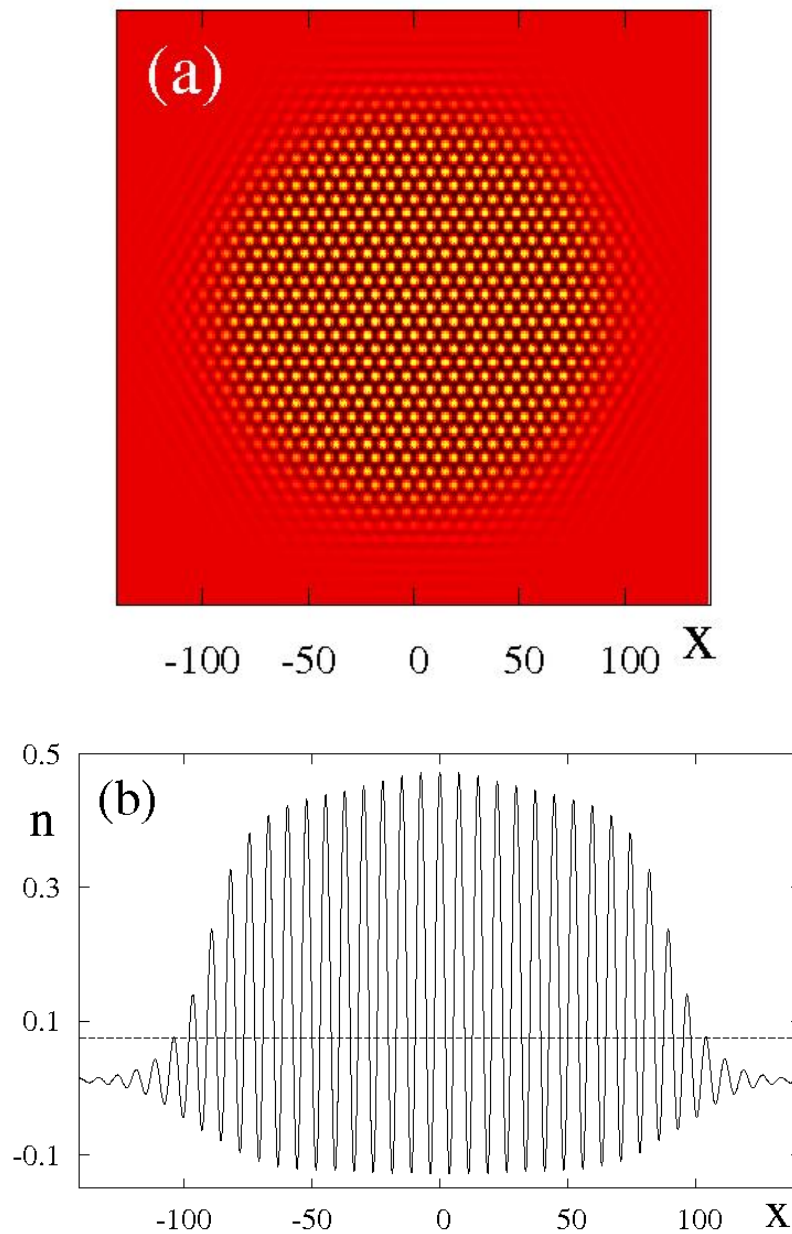


Figure 4.4: High resolution SIS solution used as reference obtained on a $1,024 \times 1,024$ grid with spatial and time steps of $\Delta x = \Delta x_0/4$ and $\Delta t = \Delta t_0$. Panel (a) presents a snapshot of the total number density at time $t = 768$, while panel (b) shows the respective total number density n distribution along the horizontal centerline.

4.3.2 Method of analysis

For characterizing the simulated crystal clusters I have used two quantities: a local one, the inter-atomic distance a , associated with the crystal structure and a global one, the diameter of the crystal d , which reflects the growth rate. The reason why I have chosen these measurable quantities is because the inter-atomic distance reflects the atomic interaction, while the diameter of the crystal can be used to calculate the average growth rate that monitors the kinetics of the phase transition. Some care is required when defining the diameter of the crystalline particle due to the atomic nature of the crystal structure and the gradual transition observed between the homogeneous liquid and the crystal. In the following, the linear size of the crystalline particle is determined by connecting the neighboring total number density peaks along the horizontal centerline of the particle (lying on a crystal plane) by straight lines and taking the intersection of the resulting peak envelope with an arbitrary threshold. I have set this arbitrary threshold between the solid and liquid phases as $n = 0.075$, and this is marked by the dashed horizontal line in Figure 4.4 (b). Furthermore Figure 4.4 (a) is a snapshot of the total number density at time $t = 768$ which was used for Figure 4.4 (b). I would like to note the number density profiles produced in molecular dynamic simulations [Davidchack, Laird, 1998], [Sun *et al*, 2004], [Morris, 2002] and [Ramalingam *et al*, 2002] display a close similarity to the diffuse solid-liquid interface shown in Figure 4.4 (b). I have used the diameter d of the crystal at dimensionless time $t = 768$ as a measure for the growth rate which reflects the time evolution of the solutions. The uncertainty of the peak positions on both ends of the diameter is approximately $2 \Delta x$ which can be represented as $\sim 175 \Delta x_0$, thus the diameters relative error is defined as $\pm 2 \Delta x / (175 \Delta x_0)$, which ranges from $\pm 0.3\%$ to $\pm 1.1\%$. As I am going to use the inter-atomic distance a to characterize the atomic level periodic nature of the solution in the crystal I need to define its relative error also. To do this I have measured 10 density waves in the crystal plane which is represented by $10a \approx 68 \Delta x_0$, however for the whole length of $10a$ the reading error is $\sim 2 \Delta x$. Therefore the relative error can be defined as $\sim \pm \Delta x / (68 \Delta x_0)$, ranging between $\pm 0.4\%$ and $\pm 1.5\%$. I would like to remind the reader once again the significance of

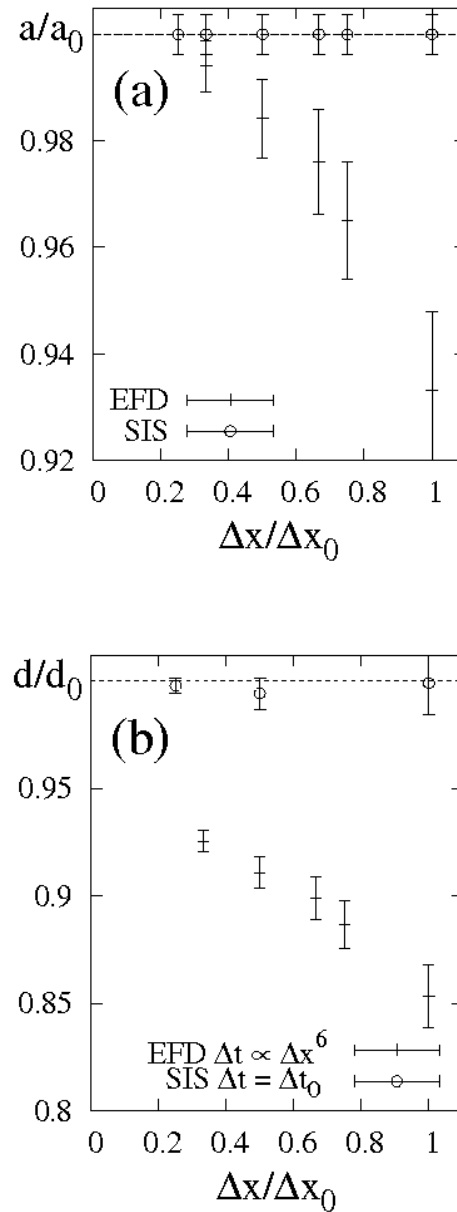


Figure 4.5: Effect of the spatial resolution on the numerical results obtained with the semi-implicit spectral (SIS) and explicit finite difference (EFD) methods. (a) Displays the dependence of the normalized inter-atomic distance against the spatial resolution, (b) shows the dependence of the normalized diameter (d/d_0) on the spatial step, Δx . The reference states are $a_0 = 7.435 \times (1.0 \pm 0.004)$, and $d_0 = 192.0 \times (1.0 \pm 0.0003)$ which correspond to the lattice constant and particle diameter and was obtained from the SIS computation with the smallest Δx and Δt .

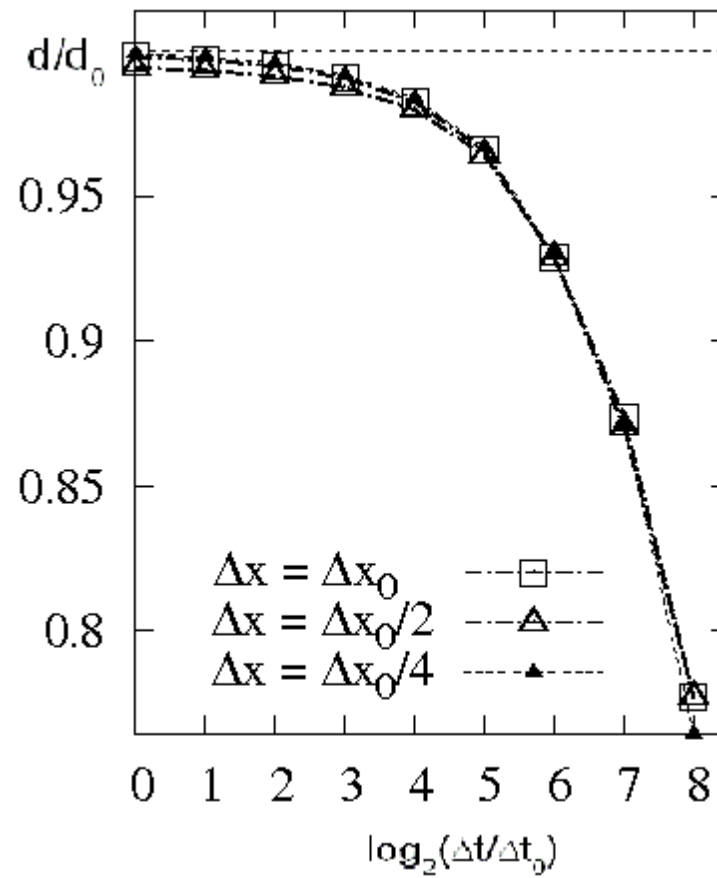


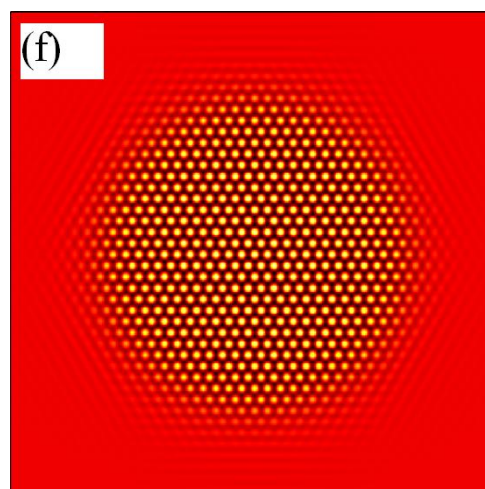
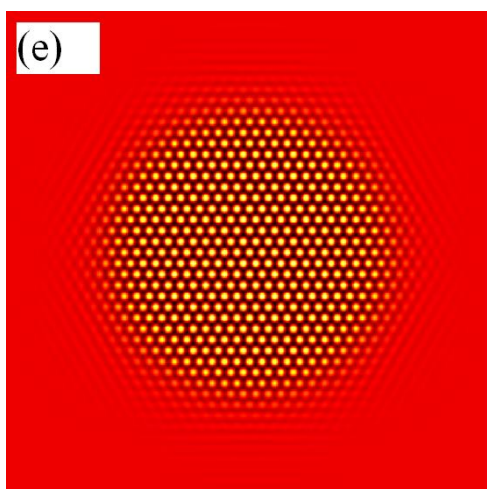
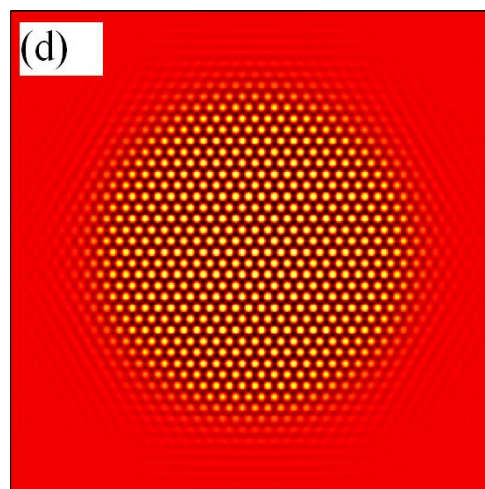
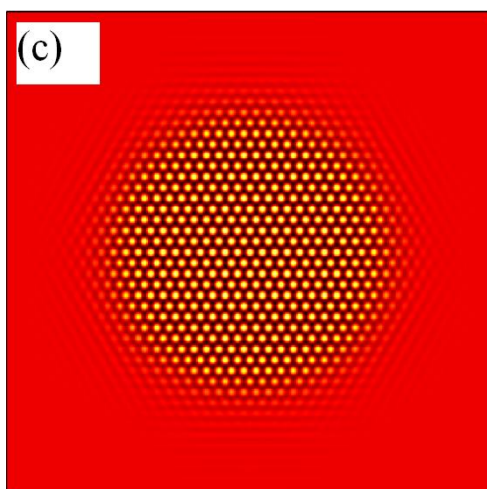
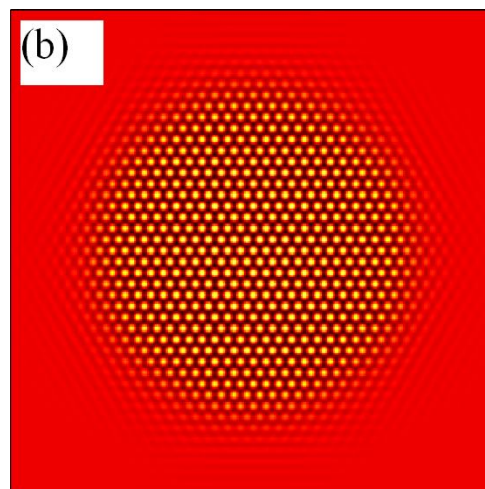
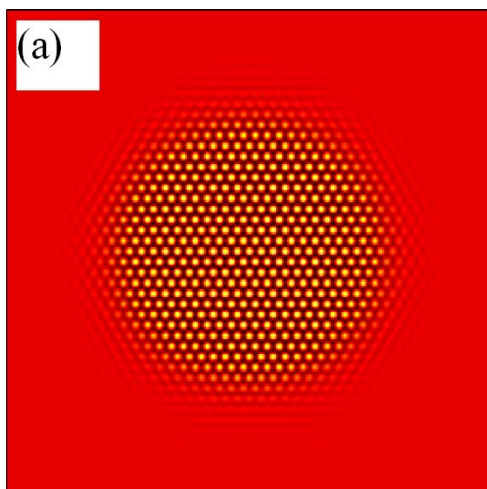
Figure 4.6: Displays the normalized diameter (d/d_0) versus the time step Δt , $d_0 = 192.0 \times (1.0 \pm 0.0003)$ which corresponds to the particle diameter and was obtained from the SIS computation with the smallest Δx and Δt .

the two quantities: the diameter of the crystal characterizes the growth kinetics of the phase transition, whereas the inter-atomic distance reflects the local crystal periodicity.

4.3.3 Numerical results

Firstly, I would like to compare the explicit finite difference scheme and the semi implicit scheme regarding the spatial and time resolution on the numerical results. This is displayed in the figures 4.5 (a), (b) and also in figure 4.6. I have shown in figure 4.5(a) the normalised inter atomic distance against the spatial resolution i.e. (a/a_0) Vs $(\Delta x/\Delta x_0)$ in order to identify if there is a dependence of the inter-atomic distance on the spatial resolution. Figure 4.5(b) displays how the diameter of the crystal depends on the spatial resolution. Figure 4.6 displays how the diameter of the crystal depends on the time steps Δt . I have normalised both the inter-atomic distance and the diameter in order to identify the true variance between the EFD and SIS schemes. In addition, I have provided further evidence of how the diameter of the crystal depends on spatial resolution in figure 4.7. The snapshots shown were taken at dimensionless time $t = 768$ and are as follows:

- (a) Shows the EFD result at $\Delta t = \Delta t_0$ and (b) shows the SIS result at $\Delta t = \Delta t_0$. Both had the spatial steps $\Delta x = \Delta x_0$.
- (c) Shows the EFD result at $\Delta t = \Delta t_0 / 8$ and (d) shows the SIS result at $\Delta t = \Delta t_0$. Both had the spatial steps $\Delta x = 3\Delta x_0 / 4$.
- (e) Shows the EFD result at $\Delta t = \Delta t_0 / 16$ and (f) shows the SIS result at $\Delta t = \Delta t_0$. Both had the spatial steps $\Delta x = 2\Delta x_0 / 3$.
- (g) Shows the EFD result at $\Delta t = \Delta t_0 / 16$ and (h) shows the SIS result at $\Delta t = \Delta t_0$. Both had the spatial steps $\Delta x = \Delta x_0 / 2$.
- (i) Shows the EFD result at $\Delta t = \Delta t_0 / 729$ and (j) shows the SIS result at $\Delta t = \Delta t_0$. Both had the spatial steps $\Delta x = \Delta x_0 / 3$.



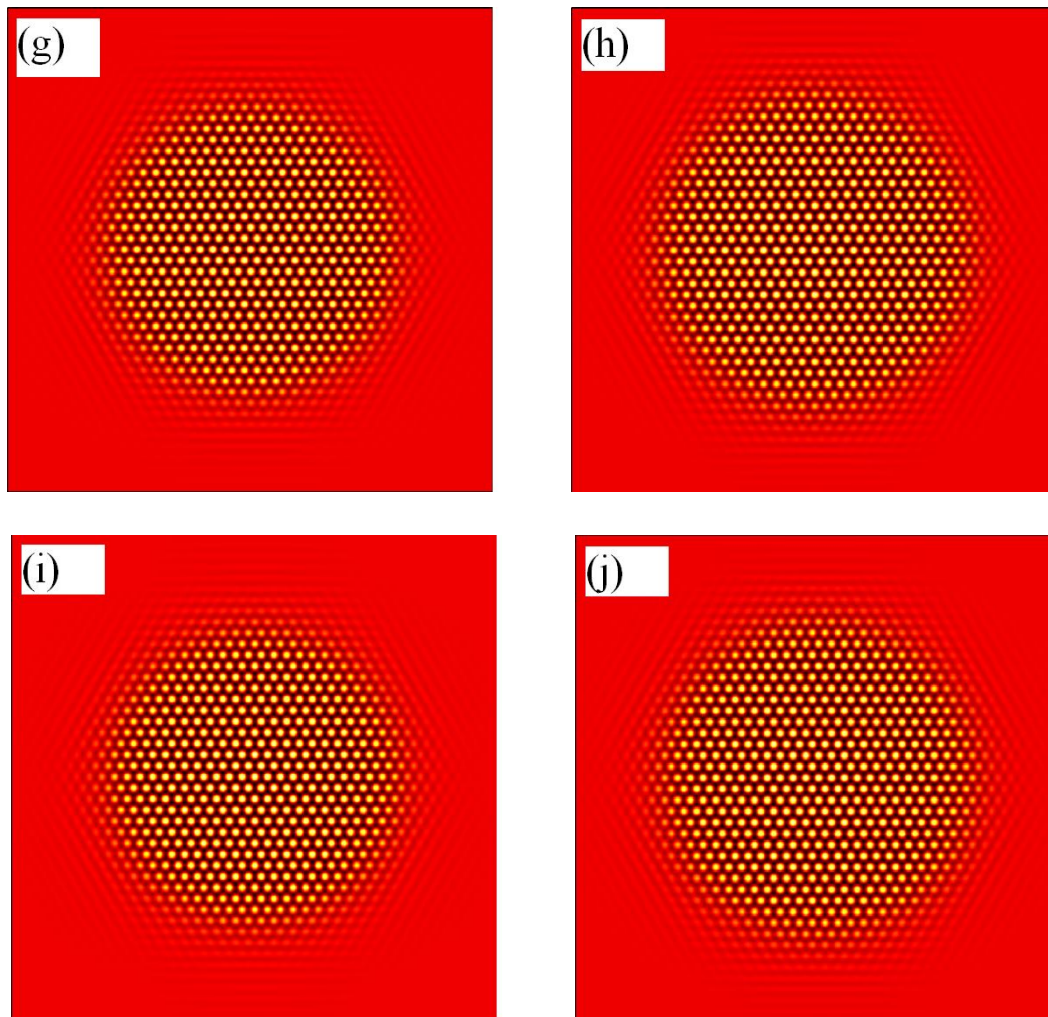


Figure 4.7: Demonstrates the difference in the diameter of the crystal for different spatial steps for the EFD which are images (a), (c), (e), (g) and (i), SIS images (b), (d), (f), (h) and (j). All snapshots were taken at dimensionless time $t = 768$ and the spatial resolution as well as the time steps have been described in the above section. One key fact that is shown here is for the SIS the diameter of the crystal d does not vary with the spatial resolution, which cannot be said for the EFD.

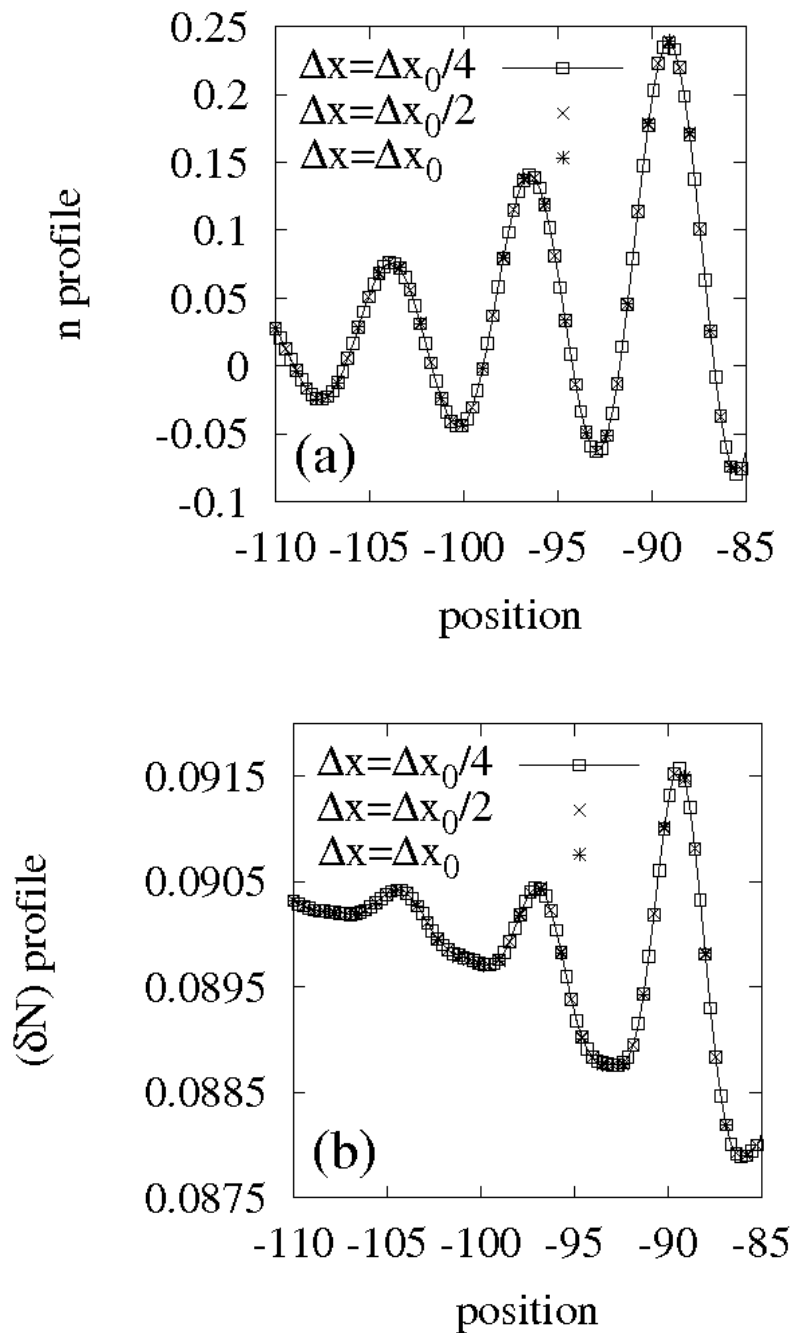


Figure 4.8: Shows the cross sectional profiles ($t = 768$) for the solid liquid interface in SIS simulations. This was performed using three different mesh spacing and $t = \Delta t_0$. Section (a) depicts the number density while section (b) depicts the total number density difference.

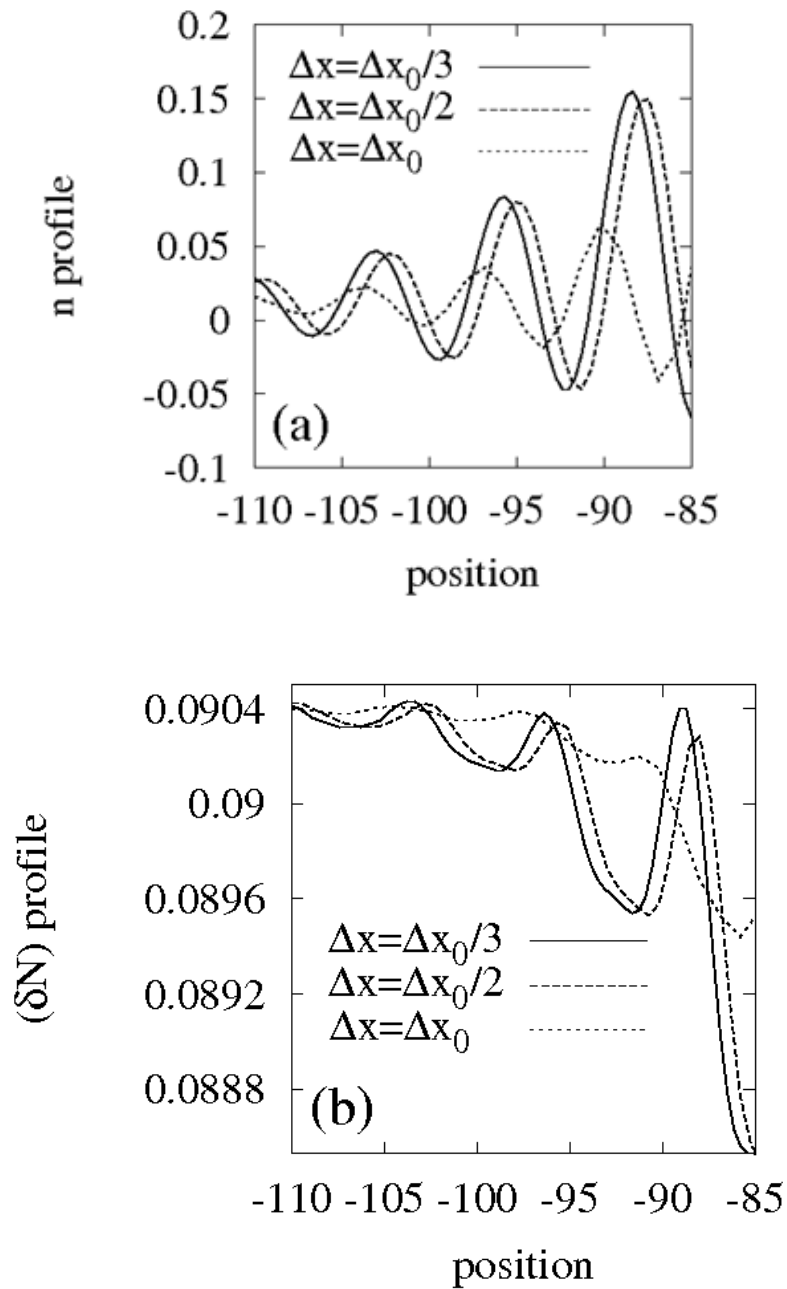


Figure 4.9: Shows the cross sectional profiles ($t = 768$) for the solid liquid interface in EFD simulations. This was performed using three different mesh spacing and to ensure numerical stability I have used the maximum time steps that were available. Section (a) depicts the number density while section (b) depicts the total number density difference.

Figure 4.8 shows the cross section of the solid-liquid interface for the semi-implicit scheme, the profile was taken at $t = 768$. Here panel (a) shows the total number density and (b) the number density difference as a function of position across the solid-liquid interface; both plots have been done with three different mesh spacings at $\Delta t = \Delta t_0$. I have also plotted the same profiles for explicit finite difference scheme in figure 4.9. To characterize the accuracy of the semi-implicit scheme against the explicit finite difference scheme, I have introduced the scaled L^2 difference for the Fourier transform of the semi-implicit scheme solution relative to the Fourier transform of the explicit finite difference scheme (equation 4.3.1). The results are displayed in Table 4.3. The L^2 difference is no other than the Euclidean distance between solutions obtained with the semi-implicit scheme and the explicit finite difference scheme:

$$\sigma_\chi = \frac{\sqrt{\langle (\chi_{SIS} - \chi_{EFD})^2 \rangle}}{\max(\chi_{EFD}) - \min(\chi_{EFD})} \quad (4.3.1)$$

Table 4.3: Scaled L^2 difference of the Fourier spectra

Δx	$\sigma_{\hat{n}}$	$\sigma_{\widehat{(\delta N)}}$
Δx_0	9.8451×10^{-2}	10.9165×10^{-2}
$3/4\Delta x_0$	9.2025×10^{-2}	9.8817×10^{-2}
$2/3\Delta x_0$	7.6462×10^{-2}	7.6462×10^{-2}
$1/2\Delta x_0$	5.5147×10^{-2}	6.1442×10^{-2}
$1/3\Delta x_0$	2.3969×10^{-2}	2.8141×10^{-2}

Here $\chi = \hat{n}$ and $\widehat{\delta N}$ are the quantities, number density and the number density difference. The hat on the quantities denotes the Fourier transform of the respective fields. The numerator of the RHS of equation 4.3.1 is the standard deviation of the explicit and semi implicit scheme for every point, $\min(\chi_{EFD})$ and $\max(\chi_{EFD})$ stand for the minimum and

maximum values of χ_{EFD} for the whole domain. I would like the reader to note that the solutions for the Fourier transforms have been obtained by the 2D FFT.

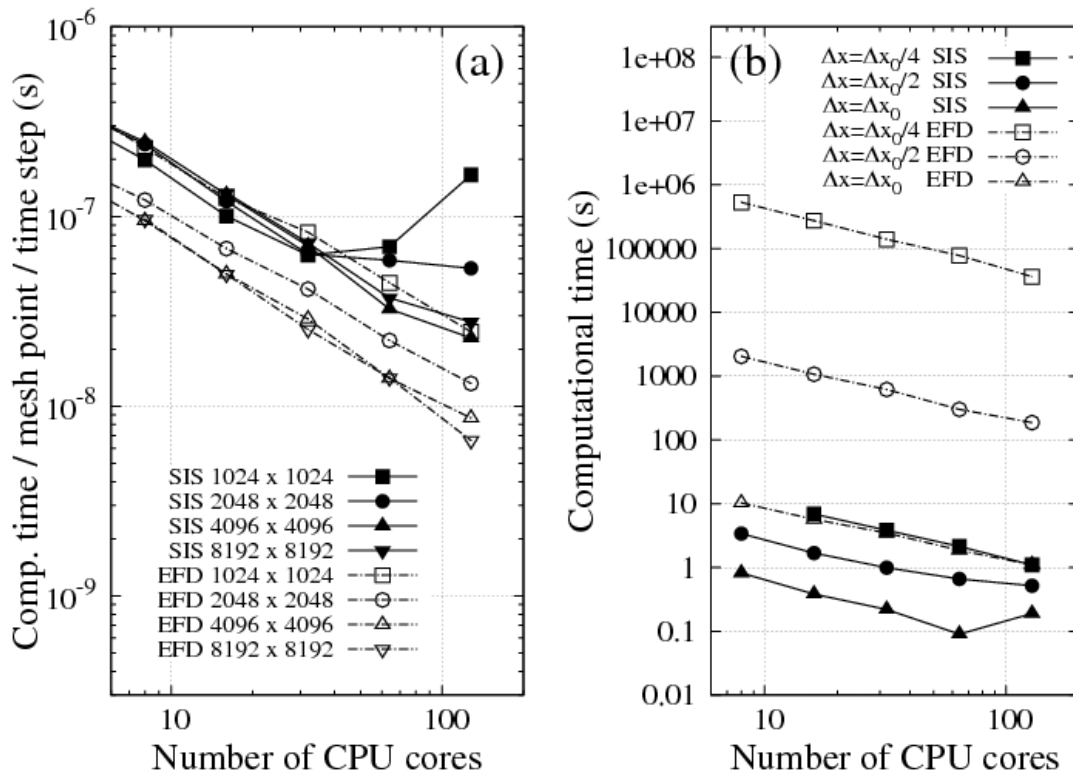


Figure 4.10: Scalability of the numerical solutions obtained by the SIS and EFD schemes. (a) Computational cost for an individual time step on a single mesh point vs. the number of CPU's. (b) Computational time is required to perform a simulation vs. the number of CPU cores, this has been conducted for three different mesh spaces.

Now, I would like to turn the reader's attention to identifying the computer efficiency and scalability of the semi-implicit and explicit finite difference scheme in parallel environment. The work described in this section was conducted by the BCAST research team and partly by me. I calculated the results for the SIS scheme. The results provide additional evidence on the relative efficiency of the two methods. The work for this section was hosted at the Research Institute for Solid State Physics and Optics (RISSPO). First, the team determined the effective computations time τ , i.e., the computational time for one time step for a single grid point expressible as:

$$\tau = \frac{t_{comp}}{(N^2 N_t)} \quad (4.3.2)$$

- t_{comp} : The full computational time.
- N_t : The number of the time steps.
- $N \times N$: Grid size.

Using this method we have plotted computational speed ($1/\tau$) against the number of CPU cores in figure 4.10 (a). This has been done for both the SIS and the EFD scheme. In addition, we have compared the computational time vs number of CPU cores curves obtained for three different spatial resolutions [$\Delta x = (\frac{1}{4}, \frac{1}{2}, 1) \cdot \Delta x_0$]. This was done to clarify for both schemes, how fast one can obtain a solution for the same time step and spatial resolution. The results refer to the same physical size and we used the largest stable time steps. As a final note, I would like to draw the readers attention to Appendix B, where I have provided all the raw data for the interatomic distance, L^2 test and the diameter of the crystal, which has been performed by me.

4.4 Eutectic solidification

Background

In solidification of a binary eutectic composition, two solid phases form cooperatively from the liquid. In the present work, I am going to investigate how the composition of the initial liquid phase influences the eutectic morphology evolving during solidification. To my understanding this appears to be the first study that addresses this question on microscopic ground using dynamical density functional theory. I have conducted the investigation using the same semi-implicit spectral scheme, which has been applied previously in this thesis for simulating solutal dendrites. I have conducted the eutectic simulations on two rectangular grid sizes: 1024×1024 and 2048×2048 . The simulations were performed on the PC cluster of the Brunel Centre for Advanced Solidification Technology (described in the previous sub-section) consisting of 160 CPU cores.

4.4.1 Parameters used in the simulations

The initial conditions have been prescribed in the following way; firstly I have filled the simulation window with appropriate uniform number density $n = \bar{n}$ and number density difference $(\delta N) = \delta \bar{N}$. Other parameters used here have been specified in Table 4.4. Following this I have placed two small crystalline clusters of 7 atoms on a hexagonal lattice (central atoms + first neighbour shells) with suitable atomic spacing and composition (δN) . The two clusters have been placed to the centre of the simulation window in contact with one another. To model the thermal fluctuations, I have used a conservative Gaussian coloured noise characterized by the correlator ζ_0 (as described in sub-section 3.2.4), while a cut-off for wavelengths smaller than $\lambda = 7\Delta x$ has been applied in the Fourier space to avoid the non-physical high frequencies (wavelengths smaller than the inter-atomic spacing). The noise strength used in this part of the work was 10^{-3} . I would also like to state that I have used periodic boundary conditions for all the simulation.

Table 4.4: Parameters used in computing the eutectic structures.

(a)	
\bar{n}	0.0
B_0^L	1.0248
B_2^L	-1.8
B_0^S	1.0
R_0	1.0
R_1	0.25
t	-0.6
v	1.0
γ	0.0
w	0.0
u	4.0
L	1.2
$\Delta x/\Delta x_0$	1.0
$\Delta t/\Delta t_0$	32.0
ζ_0	10^{-3}
N	1126

4.4.2 Method of analysis

I have determined the average grain diameter of the eutectic particle as a function of time in exactly the same way as done previously for the single component and the binary case. To summarize, I have connected the maxima of the neighboring total number of density peaks along the horizontal centerline of the particles (lying on a crystal plane) by a straight line at dimensionless time $t = 768$. From this we have taken the intersection of the resulting peak envelope with an arbitrary threshold of $n = 0.075$, which has been chosen as the limit between the solid and liquid phases. The average radial growth velocity has then been evaluated from this time dependence. Equation 4.4.1 shows how I conducted this.

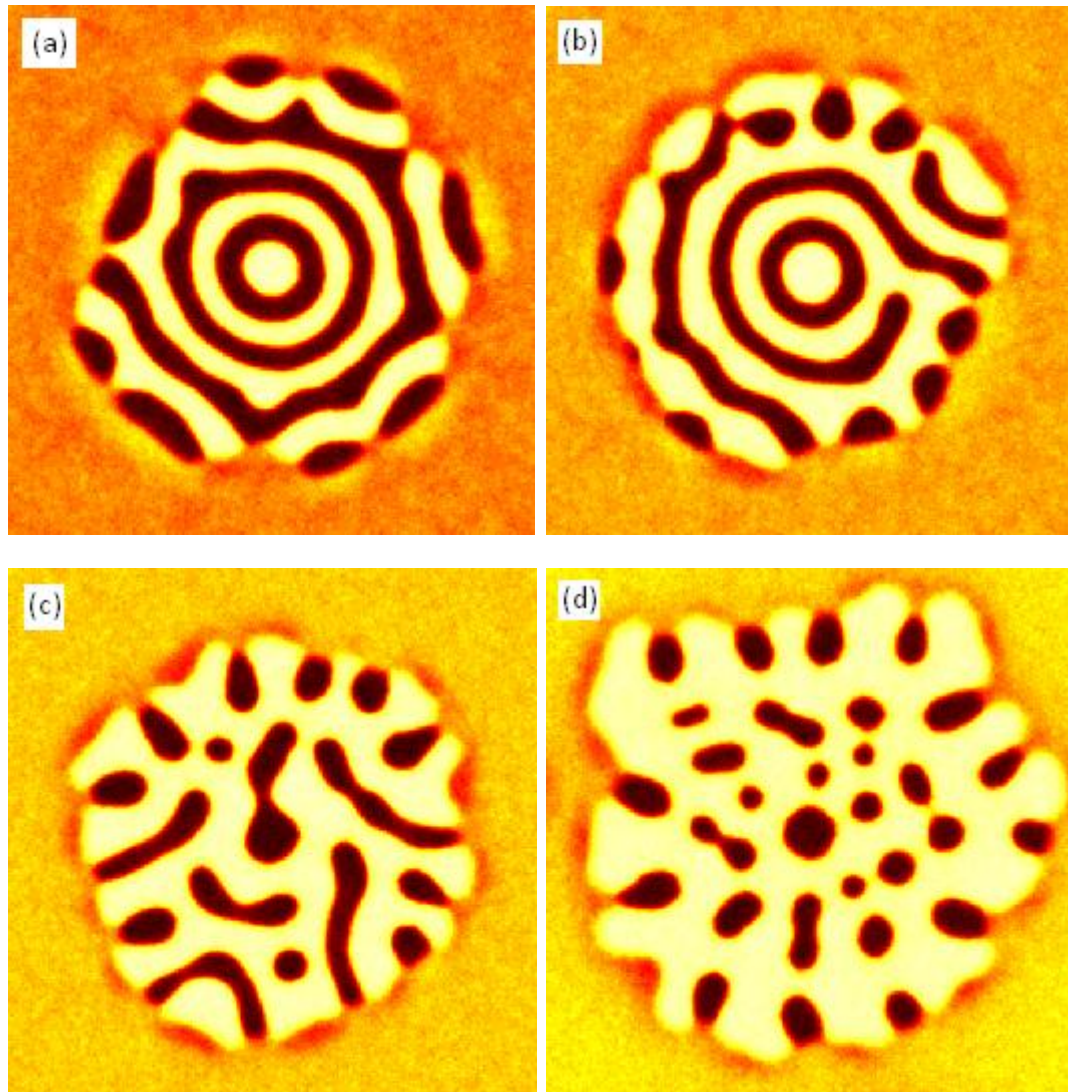


Figure 4.11: Demonstrates the eutectic transition from concentric ring-like lamellar structure to irregular dots. Simulations were conducted on a rectangular grid of size 1024×1024 . Snapshots taken at the $200,000^{\text{th}}$ time step are shown. (a) has a number density difference $(\delta N) = 10^{-6}$ and this is our reference point. (b) has a number density difference $(\delta N) = 0.02$, (c) has a number density difference $(\delta N) = 0.04$ and (d) has a number density difference $(\delta N) = 0.06$.

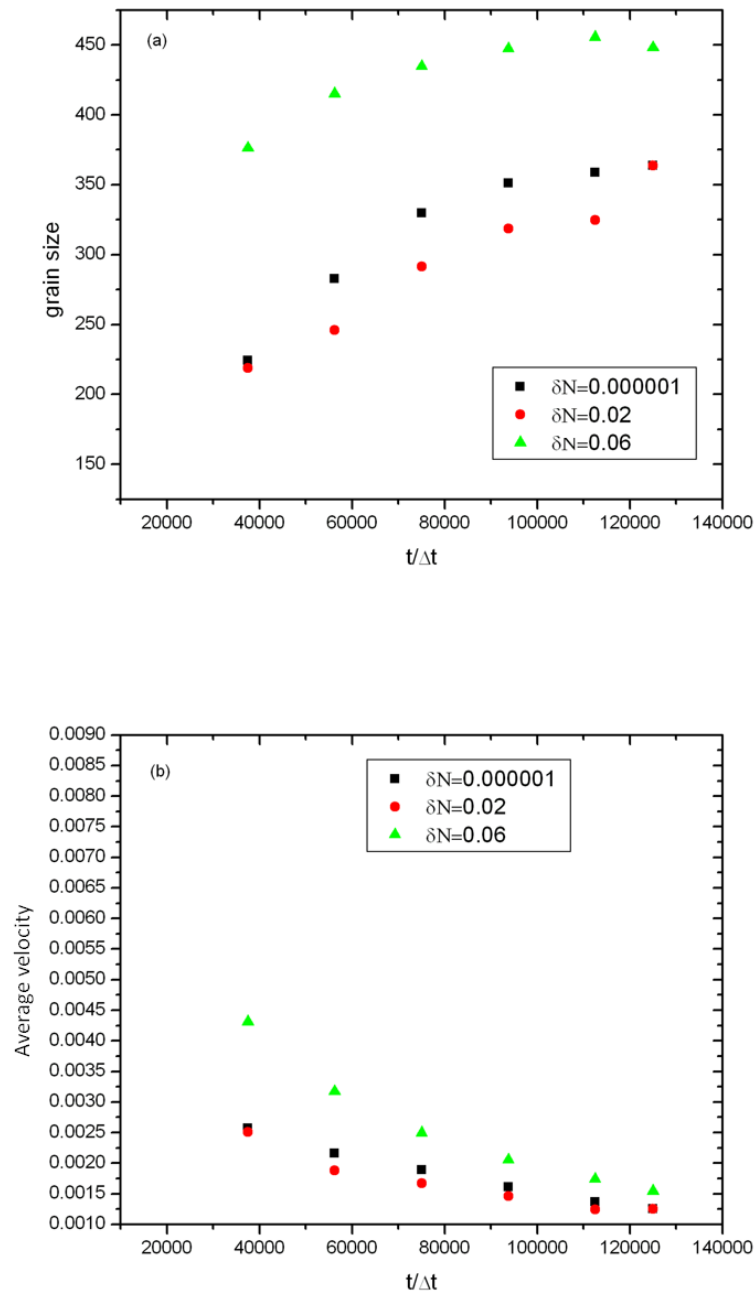


Figure 4.12: (a) Shows the grain size for $(\delta N) = 10^{-6}$, $(\delta N) = 0.02$ and $(\delta N) = 0.06$ as a function of time, (b) Shows the average velocity as a function of time with the same concentrations as in (a), both results were conducted on a simulation window of 1024×1024 .

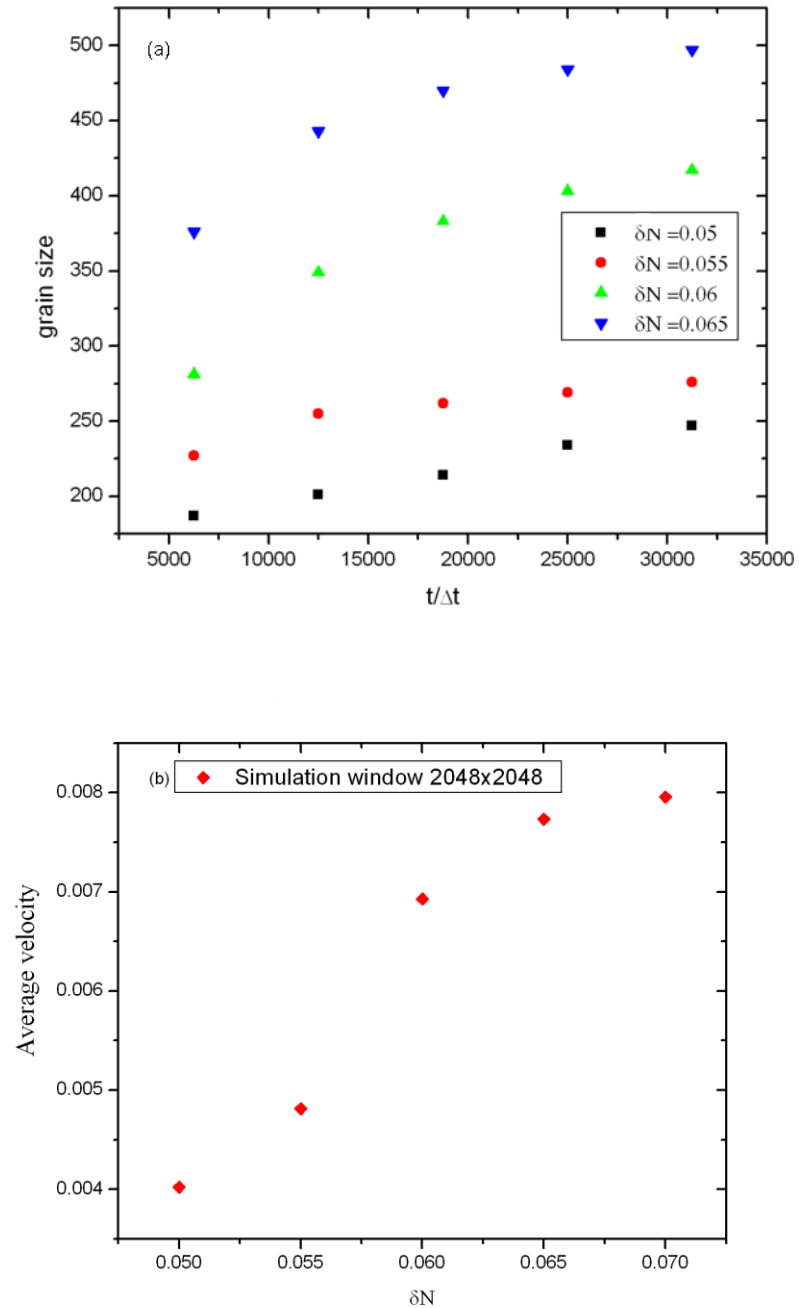


Figure 4.13: (a) Shows the average velocity for $(\delta N) = 10^{-6}$, $(\delta N) = 0.02$ and $(\delta N) = 0.06$ as a function of time, (b) shows the average velocity vs. Composition both results were conducted on a simulation window 2048 x 2048.

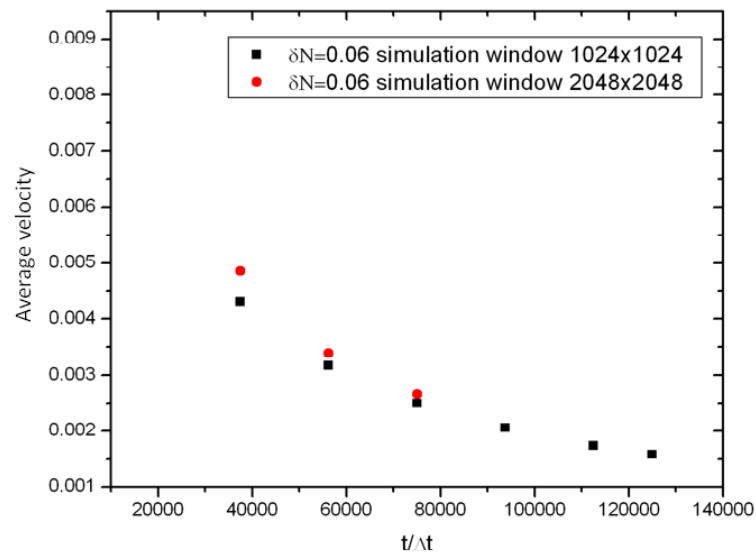


Figure 4.14: Shows the average velocity for $(\delta N) = 0.06$ obtained in the simulation windows of size 1024 x 1024 and 2048 x 2048 as a function of time.

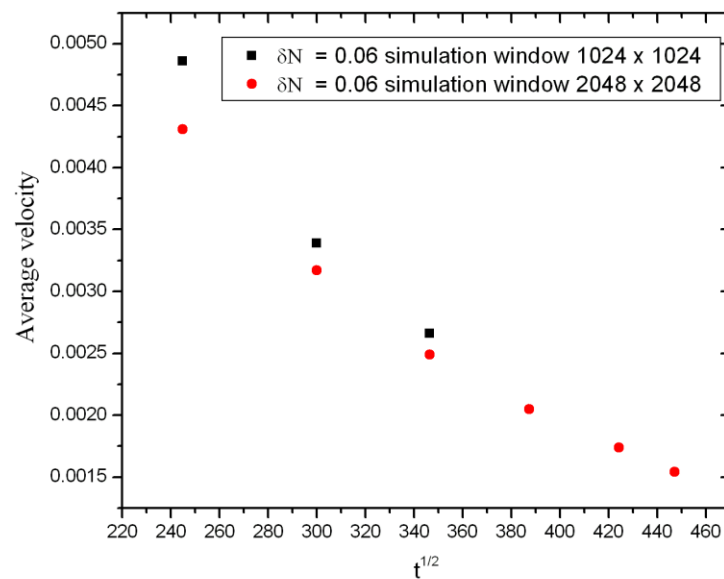


Figure 4.15 shows the average velocity for $(\delta N) = 0.06$ obtained in the simulation windows of size 1024 x 1024 and 2048 x 2048 vs. $t^{1/2}$.

This average velocity will be used to characterize the kinetics of crystallization the simulations predict.

$$\text{Average Velocity} = \text{Change in position} / \text{Elapsed time}$$

(4.4.1)

4.4.3 Results

First, I have grown a eutectic particle under the conditions specified in Table 4.4, except that the initial composition has been set as $(\delta N) = 10^{-6}$, and a simulation window of size 1024×1024 has been used. This computation has been regarded as the reference case for subsequent computations. The eutectic structure observed in the reference computation in the 200,000th time step is shown in the upper left panel of Figure 4.11. Next, I have conducted further simulations varying (δN) to clarify the effect of initial liquid composition on the eutectic morphology. In addition to the reference computation in Figure 4.11, I have provided a range of snapshots also taken at the 200,000th time step corresponding to number density differences $(\delta N) = 0.02$, $(\delta N) = 0.04$ and $(\delta N) = 0.06$. These images indicate a transition from a concentric ring-like lamellar structure (observed for near eutectic compositions) to irregular dots (appearing at off-eutectic compositions). Next I present the time dependence of the size of the eutectic crystallite and the growth velocity for these simulations in Figures 4.12, 4.13, 4.14 and 4.15, which may give information on the mechanism of crystallization.

4.5 Polycrystalline solidification of a binary alloy in two dimensions

Background

The motivation for this investigation is to explore how the above proposed semi-implicit spectral scheme produces multi-grained polycrystalline structures. With this example I am

going to demonstrate that the PFC model reproduces the kinetic of multi-grain solidification properly. The results will be analysed in terms of the Johnson-Mehl-Avrami-Kolmogorov theory. This work has been performed at the beginning of my involvement of PFC simulations, therefore, only a part of this work has been done by me, and all activities were closely supervised by G. Tegze and L. Gránásy,

4.5.1 Parameters used in the simulations

The choice of parameters that have been used in the simulations is given in Table 4.1, column (b). These values lead to dendritic solidification. First, the simulation window has been uniformly filled with the appropriate total number density $n = \bar{n}$ and number density difference values $(\delta N) = \delta \bar{N}$. Next the crystallization has been initiated by inserting 5, 50 and 500 randomly orientated and positioned crystalline clusters. Each of these clusters consisted of 13 density peaks on a hexagonal lattice (central atom + first and second neighbouring shells) with suitable atomic spacing. The computations were performed with noise representing the thermal fluctuations. These simulations were performed on a rectangular grid of size $16,384 \times 16,384$, which contained roughly 1.6 million atoms inside the simulation window.

4.5.2 Method of analysis

To evaluate the crystalline fraction first the number of atoms (density peaks) found in the crystalline regions have been determined by the ImageJ software [Abramoff *et al*, 2004]. The software will only pick atoms that belong to the solid phase by scanning the whole simulation window and identifying atoms that have a density peak larger than the average values of the bulk liquid and the bulk crystal. Next, the Johnson-Mehl-Avrami-Kolmogorov (JMAK) mean-field theory of nucleation and growth has been used to analyse the time evolution of crystallization. It describes the time evolution of crystallization in terms of a few basic assumptions.

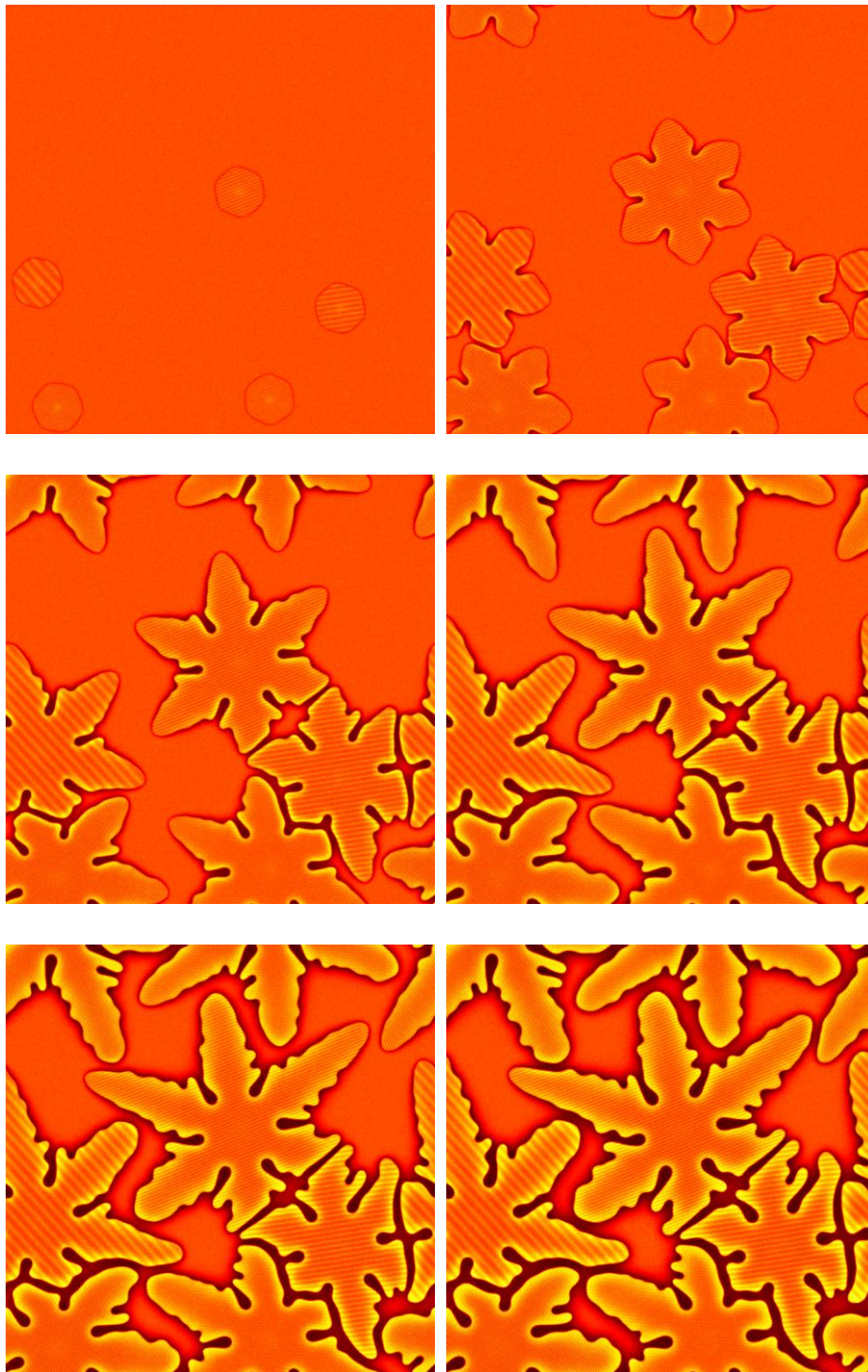


Figure 4.16: These images relate to dendritic growth of 5 crystalline particles, snapshots were taken at 1000, 5000, 7500, 10 000, 15 000 and 20 000. The simulations have been performed on a $16,384 \times 16,384$ grid, using a semi-implicit spectral method.

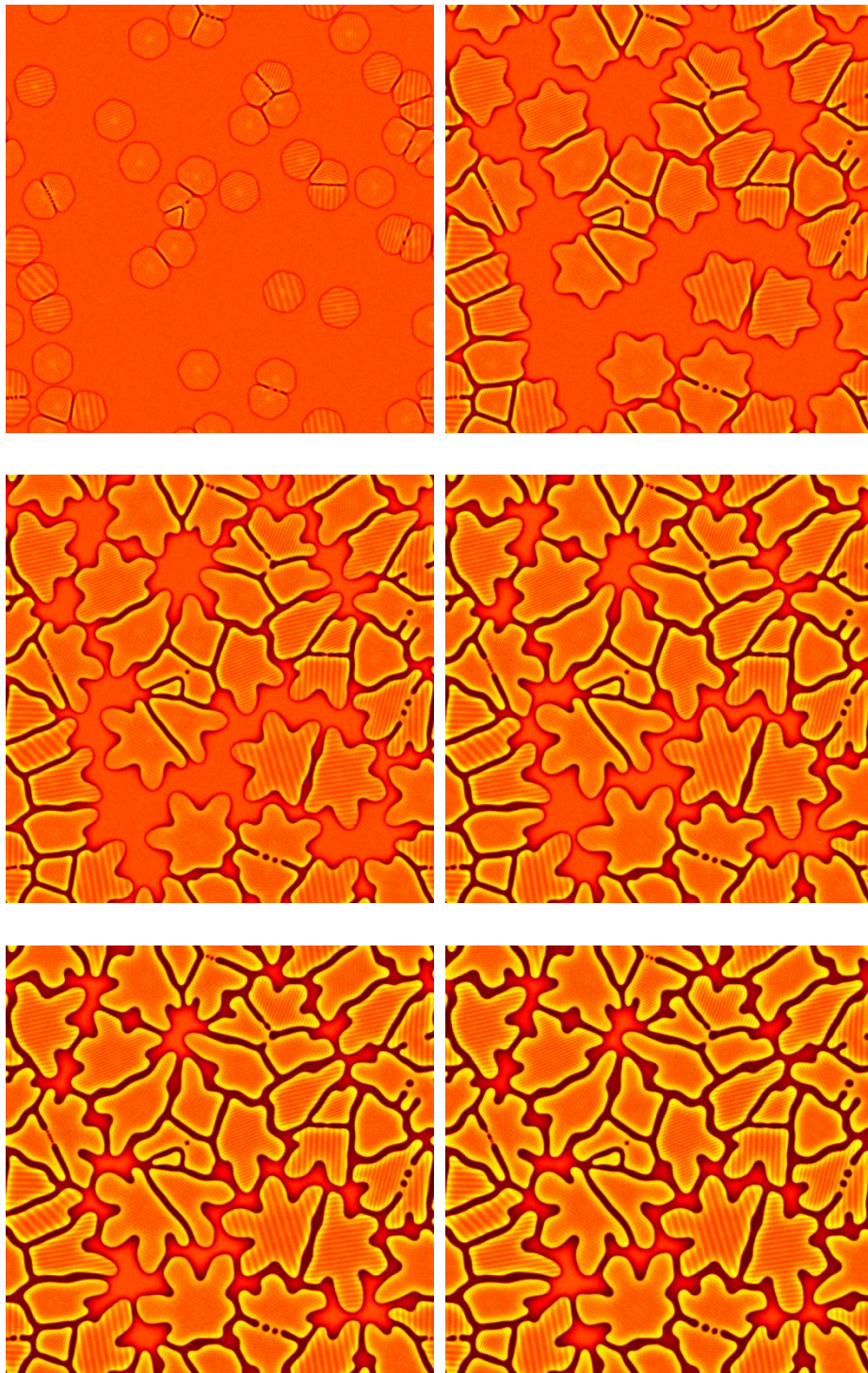


Figure 4.17: These images relate to dendritic growth of 50 crystalline particles, snapshots were taken at 1000, 3000, 4500, 5000, 7 500 and 10 000. The simulations have been performed on a $16,384 \times 16,384$ grid, using a semi-implicit spectral method.

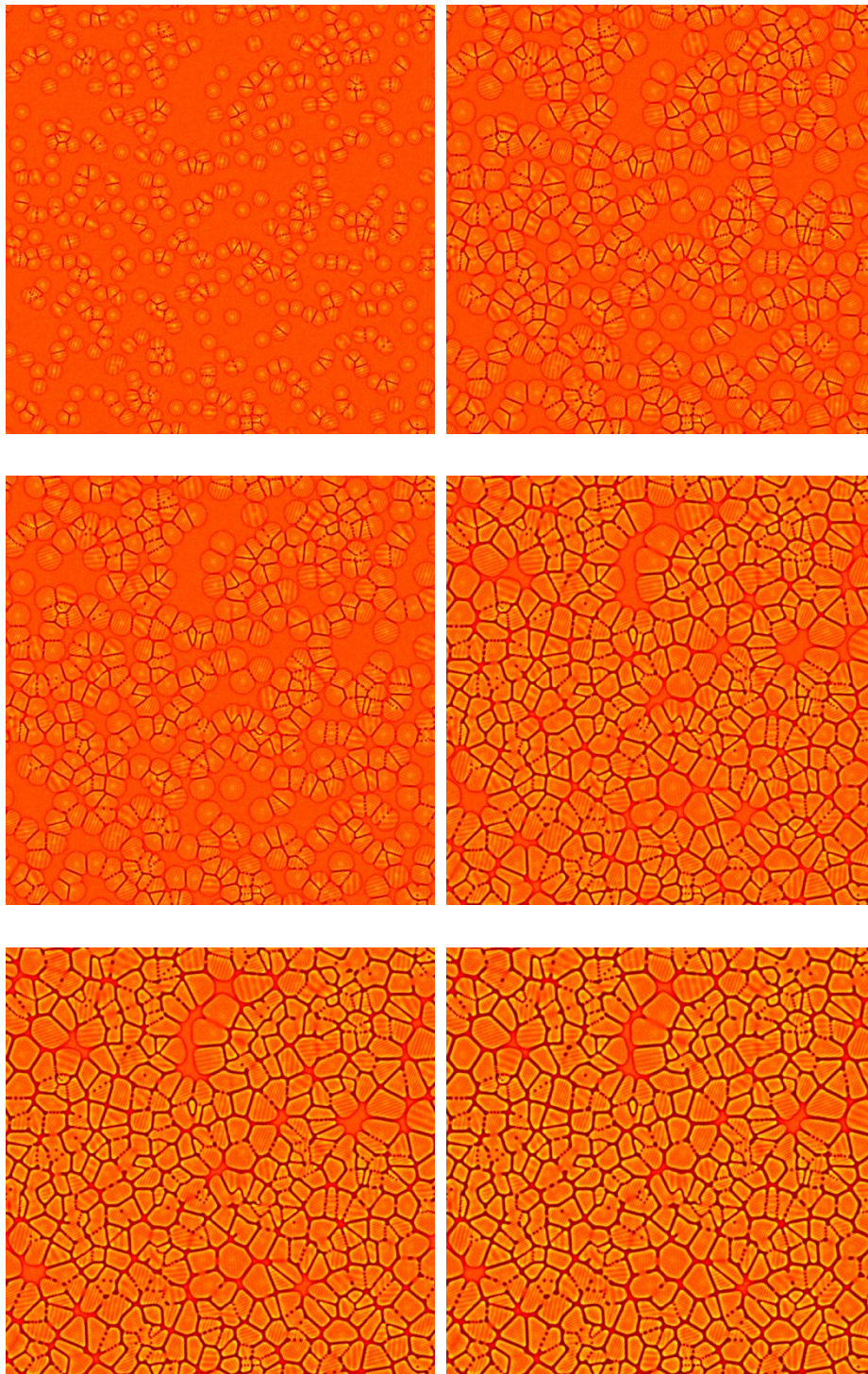


Figure 4.18: These images relate to dendritic growth of 500 crystalline particles, snapshots were taken at 250, 500, 625, 750, 1125 and 1500. The simulations have been performed on a $16,384 \times 16,384$ grid, using a semi-implicit spectral method.

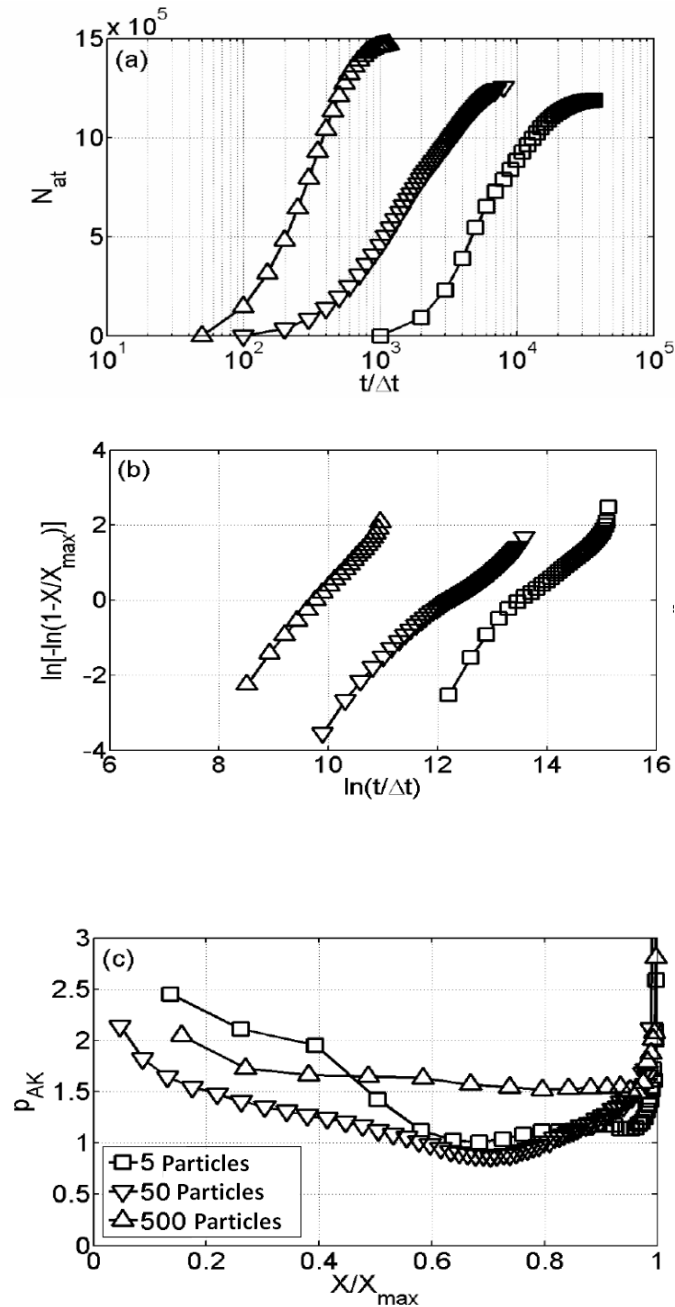


Figure 4.19: Demonstrates the crystallization kinetics for binary phase-field crystal, the top graph shows the number of atoms in the crystalline phase against time; the middle is the Avrami plots where the slope of each curve is used for the analysis of kinetics. The bottom shows Avrami-Kolmogorov exponent as a function of the reduced transformed fraction.

4.5.3 Numerical results

Firstly I would like to present the resulting multi-grain structures for the 5, 50 and 500 particle. These have been displayed in figures 4.16, 4.17 and 4.18 where I have shown snapshots of the distribution number density difference field. Next I would like to present the kinetics of crystallization as predicted by the binary PFC simulations displayed in Figure 4.19. In particular:

- (a) Shows the number of atoms in the crystalline phase as a function of the number of time steps;
- (b) Shows the Avrami plots (X and X_{max} are the transformed fraction and its maximum; while the slope of the curve determines the Avrami-Kolmogorov exponent p_{AK});
- (c) Shows the kinetic (Avrami-Kolmogorov) exponent as a function of the reduced transformed fraction.

The upward and downward pointing triangles and squares in Figure 4.19 (a), (b) and (c) correspond to 500, 50 and 5 particles, respectively.

Chapter 5

DISCUSSION

Background

This section has been broken into several sub-sections, which evaluate the results in chapter 4 and provide a deeper understanding of the PFC model used in this thesis. I would like to begin with explaining how dendrites are formed and how this is reproduced in the PFC model. Dendrites form when a non-equilibrium liquid solidifies, which can be achieved by undercooling, supersaturating the liquid or by changing its pressure. Once nucleation has happened, solidification occurs by the propagation of the interface. Since either the composition, the density or the temperature of the solid phase differs from the respective values in the undercooled liquid, the crystal growth will be governed by the respective mass, chemical or thermal diffusion. As the solid grows into a non-equilibrium liquid (undercooled or supersaturated) the Mullins-Sekerka type diffusional instability [Mullins, Sekerka, 1964] sets in and leads to fingering whose directions are determined by the anisotropies of the interfacial free energy and/or the kinetic coefficient. This then leads to the formation of the arboresque crystallization morphology known as the dendrites. In order to provide driving force for solidification in the PFC model, one has to either:

1. Lower the temperature $\Delta B = B_0^L - B_0^S$
2. Increase the number density (i.e. increase in pressure) n
3. Change the initial composition of the liquid phase δN

4. Tune the phase diagram via changing the inter-atomic distance by R_0 and R_1 , where R_1 determines the composition dependence of the inter-atomic spacing.
5. Tune the phase diagram via changing parameters L , w and u .

5.1 Preliminary-results: Application to Dendritic and Eutectic growth

The initial part of chapter 4 demonstrates how dendrites and eutectic structures are formed with the new semi-implicit PFC scheme. To begin with Figure 4.1 (a) was conducted on the RISSPO cluster which took approximately 4 days to produce on 160 CPU's equipped with InfiniBand inter-node communication. While Figure 4.1 (c) was produced using the BCAST cluster on 160 CPU's (without InfiniBand) and took approximately 10 days to produce. As both simulations were conducted on the same simulation window size and using the same SIS code, this demonstrates that the speed of data transfer between nodes is an important factor. Using these two simulations we can evaluate the sensitivity of the initial parameters, Figure 4.1 (c) is a compact dendrite which is produced by providing a higher thermodynamic driving force compared to Figure 4.1 (a). This has been introduced by increasing the initial liquid density n , and keeping all other parameters the same (see table 4.1). By changing the initial liquid density by 0.0004 there has been a dramatic difference in the structures that have been produced, which demonstrates that the solidification morphology is sensitive to the change of driving force. Furthermore in both cases (a) and (c) the dendrite arms produced almost perfect six fold symmetry, the lengths of the dendrite arms differ by approximately 0.1%. This shows that the lattice anisotropy induced by the discretization on a rectangular lattice is negligible using the semi-implicit spectral scheme. In addition Figure 4.1 (b) shows the total number density map of the small squared box on the downward pointing dendrite arm in the Figure 4.1 (a), displaying both the underlying hexagonal crystal structure and the diffuse interface between the solid and liquid phases. Lastly Figure 4.1 (d) demonstrates the eutectic structure the PFC model produces when reducing the initial number density and number density difference compared to Figure 4.1(a). The qualitative agreement of these preliminary results with those published by

Elder *et al* [Elder *et al*, 2002], implies that the present numerical implementation (SIS) successfully reproduces results obtained by a different numerical method.

5.2 Binary case

5.2.1 Convergence of the SIS scheme

With the binary PFC model stability of the time stepping is very important, as found in chapter 3. With the proper choices of the coefficients C_1 , C_2 and C_3 the stability criteria for the explicit terms have been ensured for the time and spatial steps. Full description of the stability issues and their handling are given in sub-section 3.2.2. To investigate the reliability of the proposed SIS scheme, the EFD scheme has been used as a reference. We begin the discussion by the effect of the spatial and time resolution on the SIS results summarized in Figures 4.5 to 4.8. Figure 4.5 (a) displays that the inter-atomic distance is virtually independent from spatial steps and time steps. Figure 4.5 (b) and Figure 4.6 show that the diameter of the crystallite converges at $t = 768$ as $\Delta t \rightarrow 0$. They also demonstrate that the diameter is independent of spatial steps. Figure 4.8 (a) and (b) shows the cross-section profile for the solid-liquid interface for the SIS scheme using three different mesh spacing's at $\Delta t = \Delta t_0$. Here Figure (a) depicts the total number density and Figure (b) displays the number density difference. From these figures it follows that the inter-atomic distance is virtually independent from the mesh spacing; for both the total number density and the number density difference. The points obtained with different spatial resolutions fall on top of one another with a high level of accuracy. Furthermore, from this the independence of the SIS solutions from the mesh spacing also indicates that there is convergence $\Delta x \rightarrow 0$, this can be also seen in Figure 4.5 (a). This is expected from the exponential convergence of the Fourier-spectral spatial discretization [Gottlieb, Orszag, 1977]. However one should note if $\Delta x > \Delta x_0$ there is a possibility that we may see deviation from the closely matching solutions in Figures 4.8 (a) and (b). Now we turn our attention to the diameter of the crystal, as the diameter can be considered as a measure of the average growth rate for the SIS scheme. As stated above, the particle diameter at fixed time appears to be independent of the mesh spacing within the range we have investigated $\Delta x \in [1/4, 1] \Delta x_0$. This can be seen from Figure 4.5 (b) however on closer inspection Figure 4.6 suggests that the diameter depends on the time

step. The results clearly show that there is convergence to the limiting value for $\Delta t \rightarrow 0$. In addition to this it can be seen that difference between the two smallest time steps is as small as $\sim 0.1\%$, which is indeed very small. Now comparing time steps $\Delta t = 32 \times \Delta t_0$ to the smallest time step the difference is $\sim 3.3\%$ to the limiting value. In summary the convergence tests suggests that the SIS scheme converges to the limiting solution for both $\Delta x \rightarrow 0$ and $\Delta t \rightarrow 0$. It is noted that the backward Euler time stepping is accurate to the first order, which caused the time stepping to dominate the numerical error. To improve the accuracy and efficiency of the SIS scheme time stepping methods that are accurate to higher orders are to be applied.

5.2.2 Comparison of the SIS scheme to the EFD scheme

Figure 4.9 shows the cross-sectional profiles for the solid-liquid interface for the EFD simulation performed using three different mesh spacing ($\Delta x_0/3$, $\Delta x_0/2$, Δx_0). Figure 4.9 (a) shows the number density while (b) depicts the total number difference. To be able to make the comparison to the SIS scheme data has been taken at dimensionless time $t = 768$. The results shown in Figure 4.9 were taken from the same region of the crystalline particle as in Figure 4.8. Unlike Figure 4.8 we were unable to produce simulations for mesh spacing $\Delta x_0/4$ and below due to the prohibitively large computational time. Nevertheless Figure 4.9 shows that the EFD scheme is highly dependent on the spatial resolution and convergence is seen only at smaller spatial resolutions. This convergence is also reflected in Figure 4.7, which shows snapshots of the crystals grown using the SIS and EFD taken at the same time. The time step has been varied for the EFD scheme to ensure numerical stability. A comparison of the snapshots for the SIS scheme (the right hand side) and the EFD (the left hand side) shows that in the EFD finer mesh spacing is required to obtain the same accuracy of the SIS scheme. It is noted that in the case of such high order PDEs as required for the PFC model, the EFD scheme can only be conducted on systems which have very small physical size, even more it can only be used for time scales that are very short. Figure 4.5 (a) compares the SIS and the EFD results for the inter-atomic distance. We see that the results of the EFD scheme depend on the spatial resolution. In particular, it is observed that EFD results converge to those from the SIS scheme. On closer examination the SIS scheme results

are consistently close to the limiting solution $a_0 = 7.435 \times (1.0 \pm 0.004)$ unlike the EFD which consistently underestimates the inter-atomic-distance. The mesh spacing $\Delta x = \Delta x_0$ the EFD method underestimates the inter-atomic distance by $\sim 6\%$. Even with a mesh spacing of $\Delta x = \Delta x_0/3$ the EFD scheme underestimates it by $\sim 1\%$. On the other hand when the mesh spacing is $\Delta x = \Delta x_0$ the solution from the SIS scheme is almost identical to the limiting solution. The dependence on the spatial resolution for the EFD scheme may affect the physical properties of the system such as the bulk modulus, compressibility and the free energy. It is worth noting that in the PFC model the free energy of the bulk phases depends on the accuracy of the numerical schemes that have been applied. This is not so in the conventional phase field models, where the thermodynamic properties of the bulk phases are the input, which makes these properties independent of the numerical schemes. Now we shall move to comparing the SIS scheme and the EFD in terms of the diameter of the crystalline island. From Figure 4.5 (b) one can see that the results from the SIS scheme are almost identical to the limiting solution. In contrast, the EFD scheme underestimates the diameter of the crystalline particle. At the spatial resolution $\Delta x = \Delta x_0$ the EFD scheme underestimates the diameter by $\sim 15\%$, whereas at the spatial resolution $\Delta x = \Delta x_0/3$ the result from the EFD scheme is lower by $\sim 7\%$, which is quite significant, when compared to result from the SIS scheme. Nevertheless, the EFD scheme converges towards the limiting solution. To estimate how close the EFD scheme comes to the limiting solution a linear extrapolation of the EFD data was conducted. It was shown that the EFD scheme at $\Delta x = 0$ mesh spacing underestimates the limiting solution once again however with a $\sim 4\%$ for the diameter of the crystalline particle. One should note better convergence could be seen if the simulations were conducted for smaller spatial steps and this should not be ruled out. Furthermore the cumulative rounding-off error may limit the convergence of the empirical test, which type of error is enhanced for the EFD scheme at smaller spatial steps and time test.

5.2.3 The L^2 test

The scaled L^2 difference data is provided in Table 4.3. This data quantifies the difference between the numerical solutions that were obtained by the SIS and the EFD scheme

relative to the Fourier transform of the EFD. L^2 difference takes the Euclidean distance pointwise between the solutions obtained with the semi-implicit scheme and the explicit finite difference scheme in order to calculate the standard deviation. The quantity has been normalised to see the true variation, comparisons were made for all the mesh spacing using the smallest time step SIS solution as the reference. From the data presented in Table 4.3 it appears that as the spatial step decreases so does the L^2 difference for the \hat{n} and $\widehat{\delta N}$ fields. These data show that there is convergence between the EDF and SIS solutions with decreasing spatial step.

5.2.4 Scalability of the numerical solutions obtained by the SIS and EFD schemes

Within this subsection we address the computer efficiency and scalability of both the semi-implicit spectral and explicit finite difference schemes. The results were conducted by the BCAST research team and partly by me; the role I played was calculating the results for the SIS scheme. The results for this section can be seen in Figure 4.10, Figure 4.10 (a) shows the computational cost for an individual time step on a single mesh point against the number of CPU's. Figure 4.10 (b) shows the computational time required to perform a simulation. This relationship has been determined for three different mesh spaces. We begin by examining the data in Figure 4.10 (a) computational cost for an individual time step on a single mesh point vs. the number of CPU cores. It's observed that the computation cost for the SIS scheme scales roughly linearly with the number of CPU cores except for small computations on large number of CPU cores, as one might expect. Despite the more complex algorithm, the SIS method is only slightly more costly than the simpler EFD algorithm: the computational cost of calculating a single time step at one grid point for the EFD scheme is generally smaller by a factor of ~ 2.5 . Now we compare how fast the solution can be reached by the SIS and EFD schemes for the same spatial steps. This shown in Figure 4.10 (b); here the team used 3 different spatial resolutions, which were $(\Delta x_0/4, \Delta x_0/2$ and $\Delta x_0)$. The time steps used in the case of the EFD method was the maximum stable one. Here I would like to draw the reader's attention to the fact that the results outline a linear relationship between the computation time and the number of CPU cores for both numerical methods with the exception of the

SIS results for a small number of grid points and large number of CPU cores. The latter is due to the effect of bottlenecking of information as it passes through one node to the next. From Figure 4.10 (b) it can be seen that the computational time for the SIS scheme is much smaller than the EFD scheme with regards to spatial resolution. At the spatial resolution $\Delta x_0/4$, the SIS scheme is ~ 5 orders of magnitude faster than the EFD scheme. Even at the spatial step $\Delta x_0/2$ the SIS scheme is still ~ 3 orders of magnitude faster than the EFD. However at the spatial step Δx_0 the SIS scheme is only ~ 1 order of magnitude faster than the EFD scheme, this was due to larger time steps being allowed. However, it is worth noting that to obtain the same level of accuracy as with the SIS scheme at the spatial resolution of Δx_0 the EFD scheme is required to use a finer mesh spacing of $\Delta x_0/4$ or smaller. This gives the SIS scheme a gain of ~ 6 orders of magnitude over the EFD scheme. Also remarkable is that except for small grids on a large number of CPU cores, the computation time of SIS scales with the number of the CPU cores as well as for the EFD method ($t_{comp} \propto N_{core}^{-1}$). For example, in the case of our largest computations (on a $16,384 \times 16,384$ grid), we have found this type of scaling up to our maximum number of CPU cores, 192, connected with high-speed communication. Summarizing, the SIS scheme proposed by the research team is highly stable, more accurate and faster than the EFD scheme presented by Elder [Elder *et al*, 2007].

5.3 The Single Component Case

The results for the single component case are presented in sub-section 4.2. The motivation for this investigation is to identify whether unconditional time stepping can be used to the revised semi-implicit spectral scheme for the single component case which has been shown in chapter 3. In short, the fourth order term has been treated explicitly in order to make the solution stable. To make comparison to the unconditional time stepping we have conducted conditional time stepping simulations and made comparisons between both schemes in terms of their relative errors. The results have been summarised in Figure 4.2, which shows the effect of the spatial and time resolution on the numerical results obtained with the unconditional and conditional time stepping. Here we have not investigated the behaviour of the inter-atomic distance as it is expected to be independent of the spatial resolution as observed in the binary case. Accordingly,

we have explored how the diameter of the crystalline particle (which can be considered as the average growth rate) varies with the spatial resolution. Figure 4.2 (a) compares the normalized diameter (d/d_0) against spatial resolution curves for unconditional and conditional time stepping. The diameter $d_0 = 88.45 \times (1.0 \pm 0.0009)$ from the computation with the finest spatial and time resolution has been chosen as the reference the errors displayed correspond to the smallest Δt . Figure 4.2 (a) indicates that for each individual spatial step the unconditional result was directly on top of the conditional time stepping, with virtually same relative error. This is also observed in Figure 4.3 which shows the difference between the structure for conditional and unconditional time stepping (All snapshots were taken at $t = 768$). Figure 4.3 (a) displays the conditional time stepping for $\Delta x = \Delta x_0$ with the smallest time step; whereas (b) shows the unconditional time stepping for $\Delta x = \Delta x_0$ with the smallest time step. The box to the left hand edge of the crystal in panels (a) and (b) incorporates a section of the solid-liquid interface which is shown magnified in panels (c) and (d), corresponding to conditional and unconditional time stepping, respectively. We see that the crystal structures obtained by conditional and unconditional time stepping are almost identical (Figure 4.3 (a) and (b)). Secondly we see convergence for the diameter of the crystalline particle to the limiting value for the unconditional time stepping. Also the diameter of the crystal seems to be independent of the spatial steps. This can also be seen in Figure 4.2 (c) where for each unconditional time step each normalized diameter value (d/d_0) for all three spatial steps lies on top of one another. Furthermore in Figure 4.2 (a) the relative error remains virtually the same as the spatial resolution decreases. The difference between the largest and smallest spatial step relative error varies between $\pm 0.9\%$ to ± 1.8 . Next we analyze how the diameter of the crystalline particle for conditional and unconditional time stepping varies with the time step Δt . The results are presented in Figure 4.2 (b), where we compare the calculations for the unconditional stepping obtained using the largest spatial step ($\Delta x = \Delta x_0$) with the smallest spatial step calculations ($\Delta x = \Delta x_0/2$) for conditional stepping, both at the largest time step. Remarkably, for conditional time stepping the diameter of the crystal is independent of Δt and we do see convergence to the limiting solution. For the unconditional time stepping we also see convergence to the limiting solution $\Delta t \rightarrow 0$. Furthermore, the average growth rate (the diameter of the crystal) is dependent on the time steps but the results for the two smallest time steps are virtually indistinguishable. For the conditional time stepping, from $\Delta t = 64 \times \Delta t_0$ to the

smallest time step the difference is $\sim 0.2\%$ relative to the limiting value. However beyond this point the accuracy begins to decrease. For example at $\Delta t = 128 \times \Delta t_0$ the unconditional time stepping underestimates the limiting value by $\sim 5.2\%$. This suggests that calculations with unconditional time stepping can be increased by a factor of eight compared to the largest time step calculations for the conditional time stepping with the same level of accuracy. However, beyond this point the time convergence becomes exponential; this is due to the time integration. In summary the convergence tests suggest that the unconditional time stepping scheme converges to the limiting solution for both $\Delta x \rightarrow 0$ and $\Delta t \rightarrow 0$. As well as the scheme can be used to speed up the computation significantly (by a factor of 8). Using this scheme we are able to retain the same level of accuracy as the conventional time stepping procedure.

5.4 The Johnson-Mehl-Avrami-Kolmogorov (JMAK) model

The results obtained for the kinetics of polycrystalline solidification in a binary alloy in two dimensions are presented in sub-section 4.5. They have been analysed in terms of the Johnson-Mehl-Avrami-Kolmogorov (JMAK) model, which is a formal description of crystallization that relates the crystalline fraction (X) to the nucleation and growth rates. During the phase transition X is often seen to follow a characteristic sigmoidal profile that can be broken down to three stages, which are as follows:

1. The transformation is initially very slow. This is attributed to time required for a significant number of nuclei to develop.
2. In the intermediate stage the crystallites grow freely until they start impinging one another. In this phase the transformation is rapid.
3. In the final stage the transformation becomes slower due to the impingement of the crystallites. Furthermore, the amount of untransformed material where nucleation can take place tends to zero.

In stage 1. assuming interface controlled growth (constant growth rate) the infinitesimal change of the crystalline fraction can be given as:

$$dX = I v^d dt,$$

where I is the nucleation rate, v the growth rate, d the number of dimensions, while t the time. Then the transformed fraction as a function is given by the integral:

$$X(t) = G_0 \int_0^t I(\tau) \left\{ \int_\tau^t v d\vartheta \right\}^d d\tau$$

where G_0 is a geometrical factor depending on the shape of the crystals (e.g., $G_0 = 4\pi/3$ for sphere). In the case of constant nucleation and growth rates $X = G_0 I v^d t^{1+d} = K t^n$, where n is the Avrami-Kolmogorov exponent. However, this expression is valid only for short time. Later the crystal grains grow so large that they impinge upon each other. Then, this expression overestimates the true crystalline fraction Y . A mean-field type correction can be made by taking only that part of the infinitesimal change of this overlapping crystalline fraction into account, which falls on the non-crystalline regions, i.e. by taking

$$dY = (1 - Y) dX.$$

Integrating this equation, one finds that $Y = 1 - \exp\{-X\}$. Substituting the above expression for X and rearranging the expression for Y , one obtains

$$\ln(-\ln [1 - Y(t)]) = \ln K + n \ln t \tag{5.1}$$

Plotting $(\ln(-\ln [1 - Y(t)]))$ versus $(\ln t)$, one expects a straight line whose slope is the Avrami-Kolmogorov exponent, so far as the assumptions made are valid. It is worth noting that the derivation of this expression relies on three implicit assumptions: (a)

infinite system; (b) spatially homogeneous nucleation and growth rates, (c) convex crystal shape. Violation of any of these conditions leads to deviation from the JMAK kinetics. One example that violates these conditions is diffusion controlled growth, in which case the growth rate is time dependent, and thus crystal grains of different size have different growth rates. Nevertheless, even in such case $n \approx 1 + d/2$ is expected to apply [Christian, 1981]. We note that if a constant number of nuclei are present, the Avrami-Kolmogorov exponent has the following values: $n = d$ for interface controlled growth and $n \approx d/2$ for diffusion-controlled transformation. A few specific cases:

1 = Diffusion controlled growth (conserved dynamics) of fixed number of nuclei.

2 = Interface controlled growth of the fixed number of nuclei in 2D.

3 = The nuclei is pre-formed and thus are present from the beginning and the transformation is only due to 3D growth of the nuclei.

4 = Constant nucleation rate combined with interface controlled growth in 3D.

I would like the reader to note if the distribution of nucleation is non-random the growth may severely be restricted to 1 or 2D. Therefore, site saturation may tend to have values of 1, 2 or 3 depending on whether nuclei are situated on corners, edges or surfaces. As in our simulation the liquid does not solidify fully, we have renormalized the transformed fraction by its maximum.

5.5 Polycrystalline solidification of a binary alloy in two dimensions

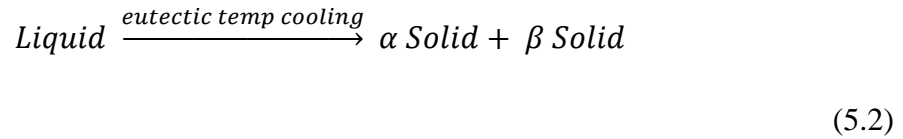
In order to evaluate the structures and find the solid fraction I have counted the number of atoms in the crystalline state by using ImageJ software [Abramoff *et al*, 2004]. The software works on the premise that it will only pick atoms that belong to the solid phase by scanning the whole simulation window and identifying atoms that have a density peak larger than a preset threshold value. The respective results are displayed in Figures 4.16,

4.17 and 4.18. In particular Figure 4.16 shows the snapshots related to dendritic growth of 5 crystalline particles taken at 1000, 5000, 7500, 10 000, 15 000 and 20 000 time steps. Figure 4.17 displays the snapshots of the growth of 50 crystalline particles, which were taken at 1000, 3000, 4500, 5000, 7500 and 10 000 time steps. Lastly Figure 4.18 presents snapshots that refer to the growth of 500 crystalline particles. The snapshots were taken at 250, 500, 625, 750, 1125 and 1500 time steps. Figure 4.19 (a) shows the number of atoms in the crystalline phase as a function of the number of time steps for crystallization started with 5, 50 and 500 nuclei. Figure 4.19 (a) indicates that in the 500 particle simulation a higher crystalline fraction has been achieved than in the simulations for 5 and 50 particles. Therein particular, for the case of 500 nuclei ~ 1.5 million atoms are solid out of the total ~ 1.6 million atoms. In comparison, at the end of the 50 particle simulation we see ~ 1.25 million solid atoms, whereas for the 5 particle simulation we see ~ 1.2 million atoms that are in the solid phase. This indicates that in the 500 particle simulation solute trapping (freezing-in of non-equilibrium composition that is closer to the composition of the liquid) is more efficient than in the 50 and 5 particle simulations. This can be explained by a faster growth rate in the initial transient phase, which can be seen by a steeper gradient in Figure 4.19 (a) for the 500 case in comparison to the 50 and 5 particle cases. Furthermore, there is supporting evidence for this interpretation in the last snapshots shown in Figures 4.16, 4.17, and Figure 4.18 the composition contrast evolving by the end of solidification is much larger in the case 5 crystal particles than in the much faster solidified 500 particle system. Next, I address the time evolution of crystallization, which will be analyzed in terms of the JMAK model. The respective results are presented in Figure 4.19 (b) and (c), which display the Avrami plots and the kinetic exponent against the reduced transformed fraction. The Avrami-Kolmogorov exponents (denoted here as P_{AK}) fall mostly between $P_{AK} = d/2 = 1$ and $P_{AK} = d = 2$. From the above definitions these values indicate a transition from interface controlled growth of the fixed number in 2D (fast initial nearly diffusionless growth due to a high level of solute trapping) and diffusion controlled growth (slow diffusion controlled growth yielding dendritic solidification observed at the later stages). However overall we can see that the plots are not linear and one can see that the respective Avrami-Kolmogorov exponents (P_{AK}) varying with the transformed fraction (or time). Another process that may potentially influence the transformation kinetics at later stages is that being concave particles the dendrites violate condition (c) required for the validity of the

JMAK model. Another effect that potentially influences crystallization kinetics, is the phenomenon termed blocking. Taking a reference point in the liquid, in the case of isotropic growth the closest crystal reaches it the first. In the case of dendrites this is not necessarily so as the growth rate strongly depends on the orientation. Accordingly, a farther crystal may grow in between the reference point and the crystal (it blocks its growth), so that it is not the closest dendrite that solidifies the reference point. It may happen though that a third dendrite blocks the blocking dendrite, before it could influence the closest crystal, so that the latter reaches the reference point first. Monte Carlo studies of such hierarchical random blocking events show that they lead to the reduction of the Avrami-Kolmogorov exponent that increases with increasing transformed fraction [Pusztai, Gránásy, 1998]. This effect is characteristic to highly anisotropic growth, which has been investigated in the following publications [Shepilov, 1990], [Shepilov, Baik, 1994], [Birnir III, Weinberg 1995], [Pusztai *et al*, 2005a] and [Pusztai *et al*, 2005b]. Lastly I would like to mention that the results for the 5 dendritic particles is in suspect as 5 particles do not provide satisfactory statistics for evaluating the kinetic exponent. One solution to this is to perform simulations on a larger scale with a greater number of fully developed dendrite than was shown in this study. However the stumbling block here is that with current hardware and numerical techniques it cannot be easily performed. However I would like to note that the final microstructure for the 500 particle simulation is commonly shown in experimental results under practical solidification conditions. This demonstrates that the PFC model effectively handles multi-grained polycrystalline structures with a high number of initial particles introduced.

5.6 Eutectic solidification

We now discuss the results for eutectic solidification displayed in the sub-section 4.4. Here it has been investigated how the composition of the initial liquid phase influences the eutectic morphology evolving during solidification. This appears to be the first study that addresses this question on microscopic grounds using the dynamical density functional theory. We begin by recalling how eutectic structures form. Eutectic reaction can be represented by the following reaction equation:



which describes the simultaneous formation of two solid phases α and β from the liquid phase below the eutectic temperature T_E . At eutectic temperature T_E the liquid and two solid phases co-exist in equilibrium. T_E is lower than the melting point of the pure components. As a result of the interplay of diffusion, capillarity, and anisotropies various eutectic structures evolve, including ordered structures (rod, lamellar, spiralling, or cellular) and disordered structures (such as fish-net, Chinese-script, etc.).

5.7 Investigation of eutectic solidification that addresses the composition dependence of eutectic pattern formation

In my studies, we have tried to model equiaxed formation of eutectic particles, however, without modelling explicitly the nucleation of the particles. Starting with two adjacent particles of different composition, we were able to grow lamellar eutectic patterns (see Figure 4.1 (d)). The eutectic particles grown so that a single seed has been inserted to the centre of the simulation window are shown as a function of composition in Figure 4.11. They have a compact shape and display a transition from concentric ring-like structure to irregular dots as a function of increasing compositional difference from the eutectic point. To characterize these morphologies the average grain diameter of the eutectic structure has been determined and plotted as a function of time. In addition we have determined and plotted the average radial growth velocity as a function of time for the number density differences 10^{-6} , 0.02 and 0.06. These simulations were conducted in a simulation window of 1024×1024 and are displayed in Figures 4.12 (a) and (b) respectively. In Figure 4.12 (b) the average radial growth velocity decreases with time for all three compositions. Figures 4.12 (a) and (b) show that the time dependence of the grain size as well as the average velocity are fairly similar for the number density differences of 10^{-6} and 0.02. This accords with the snapshots in Figure 4.11 which show that the eutectic patterns formed at these compositions are fairly similar showing a

dominantly concentric ring-like pattern. However this was not the case for the simulation performed at the number density 0.06, where it's observed (Figure 4.12 (a)) a significantly larger grain size and a higher average velocity (Figure 4.12 (b)). This implies that the thermodynamic driving force of crystallization increases with increasing (δN) for $(\delta N) > 0$. From these results it is apparent that steady state has not been achieved yet. There might be various explanations for this. One possibility is that size of the simulations is too small to establish such a steady state. In order to test this possibility, we have repeated the test simulations in a larger simulation box. Here we increased the simulation window from 1024×1024 to 2048×2048 . Figure 4.13 (a) shows the average velocity for $(\delta N) = 0.05$, $(\delta N) = 0.055$, $(\delta N) = 0.06$ and $(\delta N) = 0.065$ as a function of time. For $(\delta N) = 0.06$ a grain size of ~ 380 has been observed at the 32500^{th} time step. In comparison to the simulation conducted on the 1024×1024 simulation window at the 40000^{th} time step, the grain size is ~ 375 . Furthermore, in Figure 4.14, the time dependent average velocities obtained in simulation windows of size 1024×1024 and 2048×2048 are almost identical. A similar relationship applies for the grain size: the growth rate decreases as the eutectic structure evolves. The growth of eutectic particles and the composition dependence of the average velocity (obtained at the $200,000^{\text{th}}$ time step) are shown in Figure 4.13 (b) for larger (δN) values. The trends obtained for these cases are consistent with results obtained for smaller (δN) values. Lastly plotting the growth rate with respect to $t^{1/2}$, we obtain a linear functional relationship (Figure. 4.15). This suggests that the growth process is limited by long-range diffusion ahead of the interface. This is rather surprising. Normally, eutectic solidification is controlled by lateral diffusion at the solid-liquid interface, which establishes the characteristic wavelength of the eutectic pattern, and yields a constant growth rate. A possible explanation for this typical behaviour is that while the average composition of the crystallite is indeed close to the composition of the initial liquid, the average number densities of the crystal and the liquid are different, and this difference relaxes diffusively. This is a consequence of the diffusive equation of motion assumed in the PFC model. Such diffusive relaxation of the density differences is realistic in the case of colloidal systems. Accordingly, it is expected that the present computations are relevant only to eutectic solidification in colloidal systems. Recent experiments on charged colloids imply that eutectic solidification is indeed possible in such systems [Lorenz *et al*, 2008, 2009a, 2009b]. A recent publication by Gránásy *et al* [Gránásy *et al*,

2010] provides supporting evidence for the work I completed a year prior to the publication. In the work published it was found that after the initial period of growth the growth velocity continuously decreased and confirmed the propagation of the eutectic front was controlled by long-range diffusion. Furthermore in this work they have demonstrated a 3 dimensional eutectic structure using the PFC model.

Chapter 6

CONCLUSIONS

The results presented in this thesis address four main issues and are summarised below.

1. I have shown the efficient semi-implicit spectral scheme based on a specific operator splitting technique for solving numerically the equations of motion of the binary phase-field crystal model developed by György Tegze. I have then demonstrated the following:
 - For decreasing time and spatial steps, the solution obtained with the proposed semi-implicit scheme converges to a limiting solution.
 - In the range, where computations with the explicit finite difference scheme can be performed, results from the explicit scheme and those from the semi-implicit spectral scheme converge with decreasing time and spatial steps.
 - Significant acceleration of the computations can be expected if the proposed semi-implicit spectral scheme is used, especially if accurate solutions are needed, in which case the new method can be several orders of magnitude faster than the conventional explicit finite difference scheme.
 - Since the proposed method is implicit in the Fourier space, it can be parallelized efficiently: in the investigated size and CPU core number ranges, the computational time scales roughly with the inverse of the number of the CPU cores.

2. For the single component case I have applied the semi-implicit spectral scheme and provided numerical testing to clarify whether unconditional time stepping can be used to reduce the computational time. The following has been demonstrated:
 - The relative error for both the conditional and unconditional time stepping are virtually indistinguishable. Accordingly, unconditional time stepping can have the same accuracy as the conditional time stepping.
 - The unconditional scheme applied here can be used to speed up the computations significantly (by a factor of 8 in our case) relative to conventional conditional time stepping.

3. I have applied the SIS scheme to polycrystalline solidification within the binary PFC model. The kinetics of transformation has been analyzed in terms of the Johnson-Mehl-Avrami-Kolmogorov formalism. The following has been established:
 - The Avrami-Kolmogorov exponent P_{AK} , that characterizes the transformation kinetics, is time dependent and shows a complex behaviour. Apart from the (initial and final) transient regimes it falls into the range between the values that correspond to the purely interface controlled and purely diffusion controlled cases ($1 < P_{AK} < 2$).

4. I have investigated the morphology evolution during two-dimensional eutectic solidification within the binary PFC model as a function of the chemical composition.
 - I have observed a gradual transition from a lamellar eutectic structure to dotted patterns.
 - The average front velocity increases with δN .

Chapter 7

FURTHER WORK

We have presented in this thesis, an efficient semi-implicit spectral scheme based on a specific operator splitting technique for solving numerically the equations of motion of the binary phase-field crystal model. However we expect by applying higher order time stepping, the efficiency of the method can further be improved. Investigations are planned into this direction.

In addition to this, the single component case the model can be extended to three dimensions, as it has been done recently [Berry et al, 2008; Tegze et al, 2009]. Extension of the binary model to three dimensions would open up the way for the first atomistic simulations of three dimensional solutal dendritic structures.

The three dimensional PFC model is expected to enable us to investigate the microscopic aspects of the formation of fairly complex three dimensional polycrystalline structures, including multi-grain dendritic solidification, and the formation of polycrystalline spherulites.

We believe that these modelling tools and their descendants/combinations supported by atomistic simulations will find application in various branches of materials science and technology.

BIBLIOGRAPHY

1. [Abramoff *et al*, 2004] MD Abramoff, PJ Magalhaes, and SJ Ram, “Image processing with ImageJ”. *Biophotonics International* 11 Pg 36 – 42 (2004).
2. [Allen, Cahn, 1979] S. M. Allen and J. W. Cahn, “A microscopic theory for antiphase boundary motion and its application to antiphase domain coarsening”, *Acta Metall.* 27, Pg 1085-1095 (1979).
3. [Athreya, 2006] B. P. Athreya, “Phase-Fields and the renormalization group: A continuum approach to multiscale modelling of materials” *Phd thesis* Pg 2 (2006).
4. [Athreya *et al*, 2007] B. P. Athreya, N. Goldenfeld, J. A. Dantzig, M. Greenwood, and N. Provatas, “Adaptive mesh computation of polycrystalline pattern formation using a renormalization-group reduction of the phase-field crystal model”, *Phys. Rev. E* 76, Pg 056706 1-14(2007).
5. [Aust, Chalmers, 1952] K. Aust and B. Chalmers, “Metal Interfaces”, *American Society of Metals*, Pg 153 (1952).
6. [Beltram-Sanchez, Stefanescu, 2004] L Beltram-Sanchez and D M Stefanescu, "A Quantitative Dendrite Growth Model and Analysis of Stability Concepts", *Metall. Mater. Trans. A* 35, Pg 2471-2485 (2004).
7. [Berry *et al*, 2008] J Berry, K. R. Elder, and M Grant, “Simulation of an atomistic dynamic field theory for monatomic liquids: Freezing and glass formation”, *Phys. Rev E* 77, Pg 061506 1-7 (2008).
8. [Birnie III, Weinberg 1995] D P Birnie III and M C Weinberg, “Kinetics of transformation for anisotropic particles including shielding effects”, *J. Chem. Phys.* 103, Pg 3742–3746 (1995).
9. [Boettinger *et al*, 2002] W J Boettinger, J A Warren, C Beckermann and A Karma, "Phase-Field simulation of solidification”, *Ann. Rev. Mater. Res.* 32 Pg 163-194 (2002).
10. [Bray, 1994] A. J. Bray, "Theory of phase-ordering kinetics", *Adv. Phys.* 43, Pg 357-459 (1994).

11. [Brazowskii, 1975] S. A. Brazovskiy, "Phase transition of an isotropic system to an inhomogeneous state", *Zh. Eksp. Teor. Fiz.* 68, Pg 175 (1975).
12. [Budd *et al*, 2006] C. Budd, O. Koch, and E. Weinmuller, "Computation of self-similar solution profiles for the nonlinear Schrodinger equation", *Computing* 77, Pg 335 (2006).
13. [Cahn, Hilliard, 1958] J. W. Cahn and J. E. Hilliard, "Free energy of a nonuniform system. I. Interface free energy", *J. Chem. Phys.* 28, Pg 258 (1958).
14. [Chen, 2002] L Q Chen, "Phase-Field models for microstructure" *Ann. Rev. Mater. Res.* 32 Pg 113-140 (2002).
15. [Christian, 1981] J W Christian, "Transformations in Metals and Alloys" (Oxford: Pergamon) (1981).
16. [Christov, Marinova, 2001] C. I. Christov and R. S. Marinova, "Implicit vectorial operator splitting for incompressible Navier - Stokes equations in primitive variables", *J. Comput. Technologies* 6, Pg 92-119 (2001).
17. [Csomos *et al*, 2005] P. Csomos, I. Farago, and A. Havasi, "Weighted sequential splittings and their analysis", *Proceedings of NMCM-2002, Comput. Math. Appl.* 50, Pg. 1017–1031 (2005).
18. [Csomos, Farago, 2008] P. Csomos, and I. Farago, "Error analysis of the numerical solution of split differential equations", *Math. Comput. Model.* 48, Pg 1090-1106 (2008).
19. [Davidchack, Laird, 1998] R. L. Davidchack and B. B. Laird, "Simulation of the hard-sphere crystal-melt interface", *J. Chem. Phys.* 108, Pg 9452-9462 (1998).
20. [Diepers *et al*, 2002] H J Diepers, D Ma and I Steinbach, "History effects during the selection of primary dendrite spacing. Comparison of phase-field simulations with experimental observations", *J. Cryst. Growth* 237-239 Pg 149-153 (2002).
21. [Elder *et al*, 2002] K. R. Elder, M. Katakowski, M. Haataja, and M. Grant, "Modelling Elasticity in Crystal Growth", *Phys. Rev. Lett.* 88, Pg 245701.1-.4 (2002).
22. [Elder *et al*, 2004] K. R. Elder and M. Grant, "Modelling elastic and plastic deformations in nonequilibrium processing using phase field crystals", *Phys. Rev. E* 70, Pg 051605 1- 18 (2004).
23. [Elder *et al*, 2006] K. R. Elder , N Provatas, J Berry, P Stefanovic and M Grant, "Density Functional Theory of Freezing and Phase Field Crystal Modelling", *Phys. Rev. B*, 75, pre-press, (2006).

24. [Elder *et al*, 2007] K. R. Elder , N Provatas, J Berry, P Stefanovic and M Grant, "Phase-field crystal modelling and classical density functional theory of freezing", *Phys. Rev. B*, 75, Pg 064107 1-14 (2007).
25. [Evans, 1979] R. Evans, "The nature of the liquid-vapour interface and other topics in the statistical mechanics of non-uniform, classical fluids" *Adv. Phys.* 28, Pg 143 (1979) .
26. [Fan *et al*, 2006] M Fan, M Greenwood and N Provatas, "Phase-field simulations of velocity selection in rapidly solidified binary alloys" *Phys. Rev, E* 74, Pg 031602 1-7 (2006).
27. [Fan, Chen, 1996] D Fan and L Q Chen, "Computer simulation of grain growth using a continuum field model" *Acta Mater.* 45, Pg 611(1996).
28. [Farago, 2007] I.Farago, "New Operator Splitting Methods and Their Analysis", *Numerical Methods and Applications*, 4310, Pg 443-450 (2007).
29. [Farago, Geiser, 2006] I. Farago, J. Geiser, "Iterative Operator-Splitting methods for Linear Problems". Preprint No. 1043 of the Weierstrass Institute for Applied Analysis and Stochastics, Berlin, Germany, June 2005, *International Journal of Computational Science and Engineering*, in press, (2006).
30. [Farago, Havasi, 2005a] I. Farago and A. Havasi, "On the convergence and local splitting error of different splitting schemes". *Prog. Comput. Fluid Dynamics* 5, Pg 495 (2005).
31. [Farago, Havasi, 2005b] I. Farago, "Splitting methods and their application to the abstract Cauchy problems", in *Lecture Notes in Comput. Science*, 3401, Pg 35 (2005).
32. [Ferziger, Peric, 2002] J Ferziger, M Peric, "computational methods for fluid dynamics", *Joel H.Ferziger / Milovan Peric 3rd edition* Pg 40 (2002).
33. [Frigo, Johnson, 2005] M. Frigo and S. G. Johnson, "The design and implementation of FFTW3", *Proc. of the IEEE* 93, Pg 216 (2005).
34. [Garcia-Ojalvo *et al*, 1992] J Garcia-Ojalvo, J Sancho, and L Ramirez-Piscina, "Generation of spatiotemporal colored noise", *Phys. Rev. A* 46, Pg 4670 (1992).
35. [Gjostein, Rhines, 1959] N. Gjostein and F. Rhines, "Absolute interfacial energies of [001] tilt and twist grain boundaries in copper" *Acta Metall.* 7, Pg 319 (1959).
36. [Goldenfel *et al*, 2005] N Goldenfeld, B Athreya, and J Dantzig, "Renormalization group approach to multiscale simulation of polycrystalline materials using the phase field crystal model", *Phys. Rev. E* 72, Pg 020601 1-4 (2005).

37. [Goldenfeld *et al*, 2006] *N Goldenfeld, B Athreya, and J Dantzig*, "Renormalization Group Approach to Multiscale Modelling in Materials Science" *J. Stat. Phys.* 125, Pg 1015 1-14 (2006).
38. [Gottlieb, Orszag, 1977] *D. Gottlieb and S. A. Orszag*, "Numerical Analysis of Spectral Methods: Theory and Application (1977).
39. [Gránásy *et al*, 2002] *L Gránásy, T Börzsönyi and T Pusztai*, "Nucleation and bulk crystallization in binary phase field theory" *Phys. Rev. Lett.* 88 art no 206105 (2002).
40. [Gránásy *et al*, 2003] *L Gránásy, T Pusztai, J A Warren, T Börzsönyi, J F Douglas and V Ferreiro* "Growth of 'dizzy dendrites' in a random field of foreign particles" *Nature Mater.* 2 Pg 92 - 96 (2003).
41. [Gránásy *et al*, 2004a] *L Gránásy, T Pusztai and J A Warren* "Modelling polycrystalline solidification using phase field theory" *Phys.: Condens. Matter* 16 R1205 (2004).
42. [Gránásy *et al*, 2004b] *L Gránásy, T Pusztai, T Börzsönyi, J A Warren and J F Douglas* "A general mechanism of polycrystalline growth" *Nature Mater.* 3 Pg 645–650 (2004).
43. [Gránásy *et al*, 2010] *I Toth, G Tegze, T Pusztai, G Toth and L Gránásy*, "Polymorphism, crystal nucleation and growth in the phase-field crystal model in 2D and 3D", *J. Phys. Condens. Matter* 22 36410, (2010) .
44. [Gunton *et al*, 1983] *J. D. Gunton, M. San Miguel, and P. S. Sahni*, "Phase Transitions and Critical Phenomena", *Academic Press, New York*, Vol. 8, Pg 267. (1983).
45. [Hoyt *et al*, 2003] *J J Hoyt, M Asta and A Karma*, "Atomistic and continuum modeling of dendritic solidification" *Mater. Sci. Eng. Rep.* R 41 Pg 121–163 (2003).
46. [Hundsdoerfer, Verwer, 2003] *W. Hundsdoerfer, J. G. Verwer*, "Numerical Solution of Time-Dependent Advection-Diffusion-Reaction Equations" *Springer-Verlag, Berlin*, (2003).
47. [inf.bauwesen] <http://www.inf.bauwesen.tu-muenchen.de/~kollmannsberger/SoftLab2008ElyptMeshGen/examples.htm>
(Downloaded Feb 2011)
48. [Jacot, Rappaz, 2002] *A Jacot and M Rappaz*, "A pseudo-front tracking technique for the modelling of solidification microstructures in multi-component alloys" *Acta Mater.* 50 Pg 1909–1926 (2002).

49. [Jakobsen *et al*, 2001] *E. R. Jakobsen, K. H. Karlsen, and N. H. Risebro*, "On the convergence rate of operator splitting for Hamilton - Jacobi equations with source terms". *SIAM J. Numer. Anal.* 39, Pg 499 (2001).
50. [Karlsen *et al*, 2001] *K. H. Karlsen, K.-A. Lie, J. R. Natvig, H. F. Nordhaug, and H. K. Dahle*, "Operator splitting methods for systems of convection- diffusion equations: nonlinear error mechanisms and correction strategies". *J. Comput. Phys.* 173, Pg 636 (2001).
51. [Karlsen, Risebro, 2002] *K. H. Karlsen, and N. H. Risebro*, "Unconditionally stable methods for Hamilton - Jacobi equations". *J. Comput. Phys.* 180, Pg 710 (2002).
52. [Kobayashi *et al*, 1998] *R Kobayashi, J A Warren and W C Carter*, "Vector-valued phase field model for crystallization and grain boundary formation" *Physica D* 119 Pg 415 (1998).
53. [Kobayashi *et al*, 2000] *R Kobayashi, J A Warren and W C Carter*, "A continuum model of grain boundaries" *Physica D* 140 Pg 141-150 (2000).
54. [Krill, Chen, 2002] *C E Krill and L Q Chen*, "Computer simulation of 3-D grain growth using a phase-field model" *Acta. Mater.* 50 Pg 305 (2002).
55. [Langer, 1992] *J. S. Langer*, "Solids far from Equilibrium", edited by C. Godreche *Cambridge University Press*, Pg 297 (1992).
56. [Levin *et al*, 1997] *J. G. Levin, M. Iskandarani, and D. B. Haidvogel*, "A spectral filtering procedure for eddy-resolving simulations with a spectral element ocean model", *J. Comput.Phys.* 137, Pg 130 (1997).
57. [Lorenz *et al*, 2008] *N Lorenz, J Liu and T Palberg* "Phase behaviour of binary mixtures of colloidal charged spheres" *Colloids and Surfaces* 319, Pg 109 (2008).
58. [Lorenz *et al*, 2009a] *N Lorenz, H J Schope and T Palberg*, "Phase behavior of a deionized binary mixture of charged spheres in the presence of gravity" *J. Chem. Phys.* 131 134501 (2009).
59. [Lorenz *et al*, 2009b] *N Lorenz, H J Schope, H Reiber, T Palberg, P Wette, I Klassen, D Holland-Moritz, D M Herlach and T Okubo*, "Phase behaviour of deionized binary mixtures of charged colloidal spheres", *J. Phys. Condens. Matter* 21 464116 (2009).
60. [Marchuk, 1988] *G. I. Marchuk*, "Methods of Splitting" (*Nauka, Moscow*, 1988).
61. [Marinova *et al*, 2003] *R. S. Marinova, C. I. Christov, and T. T. Marinov*, "A fully coupled solver for incompressible Navier - Stokes equations using operator splitting". *Int. J. Comput. Fluid Dynamics* 17, Pg 371 (2003).
62. [mathworks] <http://www.mathworks.com/matlabcentral/fileexchange/16215->

[triangular-mesh-refinement](#) (Downloaded Feb 2011)

63. [Matthews, Blakesless 1975] *J. W. Matthews and A. E. Blakeslee*, "Defects associated with the accommodation of misfit between crystals" *J. Cryst. Growth* 27, Pg 118 (1974).
64. [Mendelev *et al*, 2003] *M. I. Mendelev, S. Han, D. J. Srolovitz, G. J. Ackland, D. Y. Sun, and M. Asta*, "Development of new interatomic potentials appropriate for crystalline and liquid iron" *Philos. Mag.* 83, Pg 3977–3994 (2003).
65. [Mimura *et al*, 1984] *M. Mimura, T. Nakaki, and K. Tomoeda*, "A numerical approach to interface curves for some nonlinear diffusion equations". *Jpn. J. Appl. Math.* 1, Pg 93 (1984).
66. [Morin *et al*, 1995] *Morin B, Elder K R, Sutton M and Grant M*, "Model of the Kinetics of Polymorphous Crystallization" *Phys. Rev. Lett.* 75 Pg 2156-2159 (1995).
67. [Morris, 2002] *J. R. Morris*, "Complete mapping of the anisotropy of the crystal-melt interface in Al", *Phys. Rev. B* 66, Pg 144104 1-7 (2002).
68. [Mullins, Sekerka, 1964] *W. W. Mullins and R. F. Sekerka*, "Stability of a planar interface during solidification of a dilute binary alloy" *J. Appl. Phys.*, 35, Pg 444–451 (1964).
69. [Musicki, 1978] *D. Musicki*, "On canonical formalism in field theory with derivatives of higher order-canonical transformations" *Physica A* 11, Pg 39-53 (1978).
70. [Oono, Puri, 1998] *Y. Oono and S. Puri*, "Study of phase-separation dynamics by use of cell dynamical systems. I. Modeling", *Phys. Rev. A* 38, Pg 434 (1998).
71. [Oxtoby, 1991] *D. W. Oxtoby*, "Crystallization of liquids: a density functional approach, in *Liquids, Freezing, and Glass Transition*", edited by J. P. Hansen, D. Levesque and J. Zinn-Justin, Vol. I, Pg 145 (1991).
72. [Provatas *et al*, 2005] *N. Provatas, M. Greenwood, B. Athreya, and N. Goldenfeld*, "Multiscale Modeling of Solidification: Phase-Field Methods to Adaptive Mesh Refinement", *Int. J. Mod. Phys. B* 59, Pg 4525-4565 (2005).
73. [Provatas *et al*, 2007] *N. Provatas, J. A. Dantzig, B. Athreya, P. Chan, P. Stefanovic, N. Goldenfeld and K. R. Elder*, "Using the Phase-Field Crystal Method in the Multi-Scale Modeling of Microstructure Evolution", *Journal of Metals* 59 Pg 83-90 (2007).
74. [psc.edu] http://www.psc.edu/science/2002/cizmas/images/the_computational_grid-01-full.jpeg (Downloaded Feb 2011).

75. [Pusztai *et al*, 2005a] T Pusztai, G Bortel and L Gránásy, "Phase field theory of polycrystalline solidification in three dimensions" *Europhys. Lett.* 71 Pg 131 (2005).
76. [Pusztai *et al*, 2005b] T Pusztai, G Bortel and L Gránásy, "Phase field modeling of polycrystalline freezing" *Mater. Sci. Eng. A* 413-414 Pg 412–417 (2005).
77. [Pusztai, Gránásy, 1998] T. Pusztai, L. Gránásy "Monte Carlo simulations of first-order phase transformations with mutual blocking of anisotropically growing particles up to all relevant orders", *Phys. Rev. B* 57, 14 110-14 Pg 118 (1998).
78. [Ramakrishnan, Yussouff, 1979] T. V. Ramakrishnan and M. Yussouff, "First-principles order-parameter theory of freezing" *Phys. Rev. B* 19, Pg 2775 (1979).
79. [Ramalingam *et al*, 2002] H. Ramalingam, M. Asta, A. van de Walle, and J. J. Hoyt, "Atomic-scale study of equilibrium solute adsorption at alloy solid-liquid interfaces", *Interface Sci.* 10, Pg 149 (2002).
80. [Read, Shockley 1950] J W. T. Read and W. Shockley, "Dislocation Models of Crystal Grain Boundaries" *Phys. Rev.* 78, Pg 275 (1950).
81. [Rogers *et al*, 1988] T. M. Rogers, K. R. Elder, and R. C. Desai, "Numerical study of the late stages of spinodal decomposition", *Phys. Rev. B* 37, Pg 9638 (1988).
82. [rspa] <http://rspa.royalsocietypublishing.org/content/early/2010/09/06/rspa.2010.0307/F1.large.jpg> (Downloaded Feb 2011)
83. [Sancho *et al*, 1998] J. M. Sancho, J. Garcia-Ojalvo, and H. Guo, "Non-equilibrium Ginzburg-Landau model driven by colored noise", *Physica D* 113, Pg 331 (1998).
84. [Schiotz *et al* 1998] J. Schiotz, F.D. DiTotta, and K.W. Jacobson, "Softening of nanocrystalline metals at very small grain sizes" *Nature* 391, Pg 561 (1998).
85. [Schiotz *et al* 1999] J. Schiotz, T. Vegge, F. Di Tolla, and K. Jacobsen, "Atomic-scale simulations of the mechanical deformation of nanocrystalline metals" *Phys. Rev. B* 60, Pg 971-983 (1999).
86. [Schmidt, 1996,] A Schmidt, "Computation of Three Dimensional Dendrites with Finite Elements" *J. Comp. Phys.* 125 Pg 293 (1996).
87. [Shepilov, 1990] M P Shepilov, *Sov. Phys. Crystallogr.* 35 Pg 164 (1990).
88. [Shepilov, Baik, 1994] M P Shepilov and D S Baik, "Computer simulation of crystallization kinetics for the model with simultaneous nucleation of randomly-oriented ellipsoidal crystals" *J. Non-Cryst. Solids* 171 Pg141 (1994).
89. [Shih *et al*, 1987] W. H. Shih, Z. Q. Wang, X. C. Zeng, and D. Stroud, "Ginzburg-Landau theory for the solid-liquid interface of bcc elements", *Phys. Rev. A* 35, Pg 2611 (1987).

90. [Singh, 1991] *Y. Singh*, "Density-functional theory of freezing and properties of the ordered phase" *Phys. Rep.* 207, Pg 351 (1991) .
91. [Stefanovic *et al*, 2006] *Stefanovic, M. Haataja, and N. Provatas*, "Phase-field Crystals with Elastic Interactions" *Phys. Rev. Lett.* 96, Pg 225504 1-4 (2006).
92. [Steinbach *et al*, 1996] *I Steinbach, F Pezzola, B Nestler, M Seesselberg, M Prieler, G J Schmitz and J L L Rezende*, "A phase field concept for multiphase systems" *Physica D* 94 Pg 135 (1996).
93. [Steinbach *et al*, 1999] *I Steinbac, C Beckermann, B Kauerauf, Q Li and J Guo*, "Three-dimensional modeling of equiaxed dendritic growth on a mesoscopic scale" *Acta Mater.* 47 Pg 971 (1999).
94. [Strang, 1968] *G. Strang*, "On the construction and comparison of different splitting schemes". *SIAM J. Numer. Anal.* 5, Pg 506 (1968).
95. [Sun *et al*, 2004] *D. Y. Sun, M. Asta, and J. J. Hoyt*, "Crystal-melt free energies and mobilitites in fcc and bcc Fe", *Phys. Rev. B* 69, Pg 174103 (2004).
96. [Swift, Hohenberg, 1977] *J. Swift and P. C. Hohenberg*, "Hydrodynamic fluctuations at the convective instability", *Phys. Rev. A* 15, Pg 319 (1977).
97. [Tan, Zabaras, 2006] *J Tan and N Zabaras*, "A level set simulation of dendritic solidification with combined features of front-tracking and fixed-domain methods" *J. Comp. Phys.* 211 Pg 36 (2006).
98. [Tan, Zabaras, 2007] *J Tan and N Zabaras*, "Modeling the growth and interaction of multiple dendrites in solidification using a level set method" *J. Comp. Phys.* 226 Pg 131 (2007).
99. [Tegze *et al*, 2009] *G. Tegze, L. Gránásy, G. I. Toth, F. Podmaniczky, A. Jaatinen, T. Ala-Nissila and T. Pusztai*, "Diffusion-Controlled Anisotropic Growth of Stable and Metastable Crystal Polymorphs in the Phase-Field Crystal Model" *Phys. Rev. Lett* 103, Pg 035702 1-4 (2009).
100. [Tieten *et al*, 1998] *J Tieten, B Nestler, H J Diepers and I Steinbach*, "The multiphase-field model with an integrated concept for modelling solute diffusion" *Physica D* 115, Pg 73 (1998).
101. [Tryggvason *et al*, 2002] *G Tryggvason, B Brunner, A Esmaeeli, D Juric, N Al-Rawahi, W Tauber, J Han, S Nas and Y-J Jan*, "A Front-Tracking Method for the Computations of Multiphase Flow" *J. Comput. Phys.* 169 Pg 708 (2002).
102. [vidi.cs] <http://vidi.cs.ucdavis.edu/research/unstructuredgrid> (Downloaded Feb 2010).

- 103. [Warren et al, 2003]** *J A Warren, R Kobayashi, A E Lobkovsky and W C Carter*, "Extending phase field models of solidification to polycrystalline materials" *Acta Mater.* 51 Pg 6035-6058 (2003).
- 104. [Woodhead-Galloway, Gaskell, 1968]** *J. Woodhead-Galloway and T. Gaskell*, "Structure of mixtures of simple fluids", *J. Phys. C* 1, Pg 1472 (1968).
- 105. [Wu et al, 2006]** *K.-A. Wu, A. Karma, J. J. Hoyt, and M. Asta*, "Ginzburg-Landau theory of crystalline anisotropy for bcc-liquid interfaces", *Phys. Rev. B* 73, Pg 094101 1-7 (2006).
- 106. [Wu, Karma, 2007]** *K Wu and A Karma*, "Phase-field crystal modeling of equilibrium bcc-liquid interfaces" *Phys. Rev. B* 76, Pg 184107 1-10 (2007).
- 107. [Zhu et al, 2008]** *M-F Zhu, T Dai, S-Y Lee and C-P Hong*, "Modeling of solutal dendritic growth with melt convection" *Comp. Math. Appl.* 55 Pg 1620 (2008).
- 108. [Zhu, Hong, 2002]** *M-F Zhu and C-P Hong*, "Modeling of microstructure evolution in regular eutectic growth" *Phys. Rev. B* 66 art no 155428 (2002).

Appendix A

Single component (pure material) PFC

The following subsection shows the derivation of the free energy functional for the single component case as given in [Elder et al, 2006]; the starting point is the grand potential function for N particles at temperature T being defined to be:

$$\Xi = Tr\left\{e^{\frac{(H_N - \mu N)}{K_B T}}\right\} \quad (\text{A.1})$$

Where

$$Tr \equiv \frac{1}{h^{3N} N!} \sum_{N=0}^{\infty} \int d\vec{r}_1 d\vec{r}_2 \dots d\vec{r}^N \int d\vec{p}_1 d\vec{p}_2 \dots d\vec{p}^N \quad (\text{A.2})$$

is the classical operator, with \vec{r}_i and \vec{p}_i being the position and momentum of the i^{th} atom, while μ the chemical potential and h denotes the Planck's constant. The N -body Hamiltonian can be written as $H_N = K + U + V$ where:

$$\begin{aligned}
K &= \sum_{i=1}^N \frac{p_i^2}{m_i} \\
U &\equiv U(\vec{r}_1, \dots, \vec{r}_N) \\
V &= \sum_{i=1}^N V_{ext}(\vec{r}_i)
\end{aligned}
\tag{A.3}$$

U denotes the interaction potential between particles in the system (including many body interactions), K is the total kinetic energy, with m_i the mass of the particles i^{th} and V_{ext} that represents the interaction of atom i^{th} with the external field. The probability density of a particular phase space configuration is given by:

$$f_{eq} = \Xi^{-1} e^{\frac{(H_N - \mu N)}{K_B T}}
\tag{A.4}$$

The number density operator, an N-body system is defined by:

$$\hat{\rho}(\vec{r}) = \sum_{i=1}^N \delta(\vec{r} - \vec{r}_i)
\tag{A.5}$$

The equilibrium number density is obtained by averaging the density operator with the equilibrium probability density:

$$\rho(\vec{r}) = \langle \hat{\rho} \rangle = Tr\{\hat{\rho} f_{eq}\}
\tag{A.6}$$

The PFC will ultimately yield governing equations for the time evolution of the number density (defined by equation A.6) on the diffusive time scale. We note that the equilibrium probability density f_{eq} is the functional of $\rho(\vec{r})$ [Evans, 1979]. For a given U , the Helmholtz free energy can be defined as:

$$\mathcal{F}[\rho] = Tr\{f_{eq}(K + U + K_B T \ln f_{eq})\} \quad (\text{A.7})$$

While the grand potential functional is defined by:

$$\Omega[\rho] = \int d\vec{r} \rho(\vec{r}) V_{ext}(\vec{r}) + \mathcal{F}[\rho] - \mu \int d\vec{r} \rho(\vec{r}) \quad (\text{A.8})$$

The grand potential can be put in a more familiar form by substituting equation A.6 into [Evans, 1979] and exchanging the order of integration over $\Omega[\rho]$ and Tr operation. Specifically using the result:

$$\int d\vec{r} \rho(\vec{r}) V_{ext}(\vec{r}) = -Tr\{f_{eq}V\}$$

And

$$-\mu \int d\vec{r} \rho(\vec{r}) V_{ext}(\vec{r}) = -Tr\{f_{eq}\mu N\},$$

This then leads to the known statistical mechanics result:

$$\Omega[\rho] \equiv -K_B T \ln \Xi \quad (\text{A.9})$$

The grand potential can be used to relate the chemical potential to the equilibrium density $\rho(\vec{r})$ according to $\delta\Omega[\rho]/\delta\rho(r) = 0$ which gives:

$$\mu = V_{ext}(\vec{r}) + \frac{\delta\mathcal{F}[\rho]}{\delta\rho(\vec{r})} \quad (\text{A.10})$$

Equation A.10 is fundamental to the theory of non-uniform fluids and can in principle be used to calculate the equilibrium density as shown in [Singh, 1991], [Evans, 1979]. The properties of the free energy functional $\mathcal{F}[\rho]$ can be elucidated by writing it as the sum of two terms:

$$\mathcal{F}[\rho] = \mathcal{F}_0 - \Phi[\rho] \quad (\text{A.11})$$

Where \mathcal{F}_0 represents the ideal case of non-interacting particles, while $\Phi[\rho]$ represents the total potential energy of the interaction between the particles. Note that for a given U , Φ is once again a functional of $\rho(\vec{r})$. Moreover for $U = 0$ in equation A.7 $\mathcal{F}_0[\rho]$ becomes:

$$\mathcal{F}_0[\rho] = K_B T \int d\vec{r} \rho(\vec{r}) (\ln(\lambda \rho(\vec{r})) - 1) \quad (\text{A.12})$$

Where $\lambda = \sqrt{\frac{h^2}{2m\pi K_B T}}$ [Evans, 1979]. It will be useful to expand the free energy $\mathcal{F}[\rho]$ for periodic phases in equation A.11 about the density, $\rho = \rho_l$ which corresponds to the liquid side of the solid-liquid co-existence phase diagram (at a given temperature). The change in the free energy $\mathcal{F}_c \equiv \mathcal{F}[\rho] - \mathcal{F}[\rho_l]$ then becomes:

$$\mathcal{F}_c = (\mathcal{F}_0[\rho] - \mathcal{F}_0[\rho_l]) - (\Omega[\rho] - \Omega[\rho_l]) \quad (\text{A.13})$$

The first term on the right hand side of equation A.13 can be simplified by substituting $\rho = \rho_l + \delta\rho$ in the non-logarithmic expressions of $\mathcal{F}_0[\rho]$ giving:

$$(\mathcal{F}_0[\rho] - \mathcal{F}_0[\rho_l]) = K_B T \int d\vec{r} (\rho \ln(\rho/\rho_l) - \delta\rho) \quad (\text{A.14})$$

The interaction term, $(\Phi[\rho] - \Phi[\rho_l])$ can be expanded functionally in $\delta\rho(\vec{r})$ about ρ_l , while defining the one-particle, two-particle, etc. direct correlation functions as:

$$\begin{aligned}
C_1(\vec{r}) &\equiv \frac{\delta\Phi[\rho(\vec{r})]}{\delta\rho(\vec{r})} \\
C_2(\vec{r}_1, \vec{r}_2) &\equiv \frac{\delta^2\Phi}{\delta\rho(\vec{r}_1)\delta\rho(\vec{r}_2)} \\
C_3(\vec{r}_1, \vec{r}_2, \vec{r}_3) &\equiv \frac{\delta^3\Phi}{\delta\rho(\vec{r}_1)\delta\rho(\vec{r}_2)\delta\rho(\vec{r}_3)}
\end{aligned}
\tag{A.15}$$

Using equation A.14 and A.15 in equation A.13 you finally get:

$$\begin{aligned}
\frac{\mathcal{F}_c}{K_B T} &= \int d\vec{x} \left[\rho(\vec{r}) \ln\left(\frac{\rho(\vec{r})}{\rho_l}\right) - \delta\rho(\vec{r}) \right] \\
&\quad - \frac{1}{2} \int d\vec{r}_1 d\vec{r}_2 \delta\rho(\vec{r}_1) C_2(\vec{r}_1, \vec{r}_2) \delta\rho(\vec{r}_2) + \\
&\quad - \frac{1}{6} \int d\vec{r}_1 d\vec{r}_2 d\vec{r}_3 \delta\rho(\vec{r}_1) C_3(\vec{r}_1, \vec{r}_2, \vec{r}_3) \delta\rho(\vec{r}_2) \delta\rho(\vec{r}_3) \\
&\quad + \dots
\end{aligned}
\tag{A.16}$$

The function C_2 is the two point direct correlation function of an isotropic fluid and it is usually denoted $C_{ij} \equiv C_2(r_{12})$, where $r_{12} \equiv |\vec{r}_1 - \vec{r}_2|$. The function C_3 is the three point correlation, etc.

Appendix B

Raw Data for the Binary Simulations

Atomic distances for 13 density peaks

Mesh Spacing	time steps for the SIS scheme											The EFD scheme
	0.0125	0.025	0.05	0.1	0.2	0.4	0.8	1.6	3.2	6.4	12.8	smallest available time step
0.275	7.436613	7.438907	7.443384	7.435874	7.436019	7.435835	7.440144	7.4338	7.432975	7.438841	7.439548	NA
0.366666667	7.440609	7.439094	7.436779	7.439824	7.436073	7.442259	7.440257	7.432202	7.4382	7.437946	7.439747	7.393442221
0.55	7.443645	7.44799	7.457725	7.442232	7.441709	7.430373	7.44172	7.44062	7.433635	7.44403	7.43815	7.315515625
0.733333333	7.433866	7.436147	7.453233	7.46526	7.460999	7.460765	7.484107	7.451888	7.45074	7.442967	7.486431	7.235164442
0.825	7.430363	7.428218	7.438802	7.42269	7.424753	7.421923	7.42401	7.423185	7.432838	7.417781	7.425103	7.169148525
1.1	NA	NA	7.42742	7.438563	7.46064	7.46526	7.4459	7.4789	7.422434	7.48066	7.56085	6.930814

Grain size for 13 density peaks

Mesh Spacing	time steps for the SIS scheme											The EFD scheme
	0.0125	0.025	0.05	0.1	0.2	0.4	0.8	1.6	3.2	6.4	12.8	smallest available time step
0.275	NA	NA	191.5805	191.3799	190.9809	190.1887	188.6138	185.4132	178.267	167.7646	149.2132	
0.366666667	NA	NA	186.5013	186.2877	185.8577	184.9868	183.1944	179.3333	173.4271	161.8819	143.9324	177.669988
0.55	NA	NA	190.8673	190.6812	190.3104	189.5725	188.1015	185.0909	178.3092	167.0577	149.2295	175.084642
0.733333333	NA	NA	185.6958	185.456	184.9744	184.0029	182.0083	177.7449	172.2131	161.0075	143.9219	173.407374
0.825	NA	NA	189.3308	189.1488	188.7846	188.0563	186.582	182.4793	175.9072	164.7709	146.7383	170.668044
1.1	NA	NA	191.7904	191.5895	191.1897	190.3977	188.8247	185.6348	178.5489	167.2675	146.7857	164.48435

**Grain size for 19
density peaks**

Mesh Spacing	time steps for the SIS scheme											The EFD scheme
	0.0125	0.025	0.05	0.1	0.2	0.4	0.8	1.6	3.2	6.4	12.8	smallest available time step
0.275	NA	NA	NA	NA	NA	NA	NA	NA	NA	NA	NA	NA
0.366666667	184.2231	184.1709	184.0685	183.8611	183.4437	182.597	180.8463	177.4453	172.4027	161.9178	145.3338	177.669988
0.55	172.6035	172.5611	172.4777	172.3091	171.9719	171.2931	169.9115	167.0209	161.6466	152.8301	138.1168	175.084642
0.733333333	156.3511	156.3153	156.2452	156.1045	155.8217	155.2539	154.1042	151.7274	147.0497	140.0399	127.4127	173.407374
0.825	148.0012	147.9696	147.9052	147.7775	147.5228	147.0182	146.0241	144.0718	140.1482	132.4205	120.3054	170.668044
1.1	NA	NA	116.4739	116.3762	116.1807	115.7909	115.0241	113.5181	113.1322	104.5442	97.42578	164.48435

L² Test

Mesh Spacing	stddev pfc	stddev chem
0.366666667	0.02396937	0.028140669
0.55	0.055147402	0.061442385
0.733333333	0.07646277	0.078096489
0.825	0.092025034	0.098817966
1.1	0.098451443	0.109165965